SATELLITES, STREAMS, AND SURVEYS, OH MY!

A Dissertation

by

PETER STANTON FERGUSON

Submitted to the Graduate and Professional School of
Texas A&M University
in partial fulfillment of the requirements for the degree of

DOCTOR OF PHILOSOPHY

Chair of Committee,	Jennifer Marshall
Co-Chair of Committee,	Louis Strigari
Committee Members,	Casey Papovich
	Jianhua Huang
Head of Department,	Grigory Rogachev

August 2021

Major Subject: Astronomy

ABSTRACT

In the past few decades we have entered a new age of astronomy where large scale astronomical surveys have enabled us to advance and revolutionize our understanding of the Milky Way and its neighborhood. The outskirts of our Galaxy has been found to be teeming with substructure ranging from intact objects such as the classical satellites to the much smaller ultra-faint dwarf galaxies, to disrupted objects like stellar streams. In this thesis I discuss two science projects that I have led characterizing substructure of the Milky Way. The first project studies the core of the Sagittarius dwarf spheroidal galaxy, where we use RR-lyrae type stars as three-dimensional tracers in order to characterize the shape of this core. Second, I discuss my project with the DECam Local Volume Exploration (DELVE) survey. This survey uses archival DECam data and 126 nights of dedicated observations to create a deep wide-field photometric catalog of the high-Galactic latitude southern sky. In this analysis, I fully characterize the Jet stellar stream for the first time using DELVE and *Gaia* data. Additionally, I will cover my instrumentation work on TCal which will help to enable and enhance the science return for the next generation of large scale precision photometric surveys.

DEDICATION

To my parents Carol and Stuart who have done so much to support and encourage me in my scientific journey.

Love and appreciate you both so much.

ACKNOWLEDGMENTS

First of all, I would like to express my gratitude to the graduate student community in the Texas A&M astronomy group. These people helped me to mentally survive and thrive throughout graduate school and I appreciate that. In particular, I would like to thank Sarah Cantu and Jonathan Cohn for their support and help in becoming a better astronomer and member of my communities (as well as all the silliness and music).

I would like to thank my co-advisors Jennifer Marshall and Louis Strigari for their support through this process. Specifically, for how they enabled me to chase the projects I was excited in no matter who they were with and for introducing me to the Dark Energy Survey (DES) collaboration.

One of my greatest joys in grad school has been to learn how much I enjoy working in collaborations. So, I also want to make sure to thank all of the DES Milky Way working group and the DECam Local Volume Exploration (DELVE) survey communities. These groups have continued to inject excitement and passion into my life making it a pleasure to work on science. I would especially like to mention Alex Drlica-Wagner who more than anyone else has acted as a role model for the scientist I would like to be. This is especially true in the ways in which he interacts with the collaborations I am apart of and the students (including me) who he mentors.

I would also like to acknowledge that Texas A&M University where I have completed this dissertation, sits on unceded native land. I would like to recognize the aboriginal and indigenous peoples' land which we occupy. This includes the aboriginal homeland of the Tonkawa people. The Texas state government forcibly removed the Tonkawa in 1855, ultimately relocating them to their current reservation in northern Oklahoma. The Brazos County region was also the traditional land of the Atakapa-Ishak people, particularly the Bidai.

Last but not least I would like to thank all of the work done by others to enable me to

focus on science. This includes all of the staff in the Mitchell institute and Department of Physics and Astronomy. I would like to particularly highlight Leona and Monique Glover at the Munnerlyn Laboratory who both ensured I was happy and had a great place to work.

CONTRIBUTORS AND FUNDING SOURCES

Contributors

This work was supported by a thesis committee consisting of my co-advisors, Professors Jennifer Marshall and Louis Strigari, and Professor Casey Papovich of the Department of Physics and Astronomy and Professor Jianhua Huang of the Department of Statistics.

The analysis done in Chapter II was led by the author (Peter Ferguson), with help from Professor Louis Strigari. We are grateful to Jennifer Marshall and Andrew Pace for discussions that improved this analysis. The author acknowledges the Texas A&M University Brazos HPC cluster that contributed to the research reported here.

The analysis done in Chapter III was led by the author (Peter Ferguson) and includes contributions from N. Shipp, A. Drlica-Wagner, T. S. Li, W. Cerny, K. Tavangar, A. B. Pace, J. L. Marshall, A. H. Riley and other members of the DELVE-WIDE working group and DELVE collaboration.

The analysis done in Chapter IV was led by the author (Peter Ferguson) and includes contributions from L. Barba, D. L. DePoy, L. M. Schmidt, J. L. Marshall, T. Prochaska, L. Bush, D. Freeman, L. Gardner; I. Gutierrez; D. Kim; Z. Kunnummal, J. Mason, M. Sauseda, H. Sharp and M. Torregosa.

Additionally, the analyses presented in chapters II and III have made use of data from the European Space Agency (ESA) mission *Gaia* (`https://www.cosmos.esa.int/gaia`), processed by the *Gaia* Data Processing and Analysis Consortium (DPAC, `https://www.cosmos.esa.int/web/gaia/dpac/consortium`). Funding for the DPAC has been provided by national institutions, in particular the institutions participating in the *Gaia* Multilateral Agreement. All other work conducted for the thesis (or) dissertation was completed by the student independently.

In chapter III the DELVE project is partially supported by Fermilab LDRD project

L2019-011 and the NASA Fermi Guest Investigator Program Cycle 9 No. 91201.

This project (DELVE) used data obtained with the Dark Energy Camera (DECam), which was constructed by the Dark Energy Survey (DES) collaboration. Funding for the DES Projects has been provided by the DOE and NSF (USA), MISE (Spain), STFC (UK), HEFCE (UK), NCSA (UIUC), KICP (U. Chicago), CCAPP (Ohio State), MIFPA (Texas A&M University), CNPQ, FAPERJ, FINEP (Brazil), MINECO (Spain), DFG (Germany), and the collaborating institutions in the Dark Energy Survey, which are Argonne Lab, UC Santa Cruz, University of Cambridge, CIEMAT-Madrid, University of Chicago, University College London, DES-Brazil Consortium, University of Edinburgh, ETH Zürich, Fermilab, University of Illinois, ICE (IEEC-CSIC), IFAE Barcelona, Lawrence Berkeley Lab, LMU München, and the associated Excellence Cluster Universe, University of Michigan, NSF's National Optical-Infrared Astronomy Research Laboratory, University of Nottingham, Ohio State University, OzDES Membership Consortium University of Pennsylvania, University of Portsmouth, SLAC National Lab, Stanford University, University of Sussex, and Texas A&M University.

This work is based on observations at Cerro Tololo Inter-American Observatory, NSF's National Optical-Infrared Astronomy Research Laboratory (2019A-0305; PI: Drlica-Wagner), which is operated by the Association of Universities for Research in Astronomy (AURA) under a cooperative agreement with the National Science Foundation.

Funding Sources

The analysis done in Chapter II was partially supported by the College of Science at TAMU through a Strategic Transformative Research Program (STRP) Seed Grant.

The analysis done in Chapter III was partially supported by the Visiting Scholars Award Program of the Universities Research Association.

The analysis done in Chapter IV was supported by Charles R. and Judith G. Munnerlyn, George P. and Cynthia W. Mitchell, and their families through their generous support of astronomical instrumentation activities in the Department of Physics and Astronomy at Texas

A&M University. Additionally, This material is based upon work supported by the National Science Foundation under Grants 1715865, and AST-1560223, "REU Site: Astronomical Research and Instrumentation at Texas A&M University."

NOMENCLATURE

2MASS	Two Micron All-sky Survey
CCD	Charge Coupled Device
CTIO	Cerro Tololo Inter-American Observatories
dec	Declination
DECal	Dark Energy Camera calibration system
DECam	Dark Energy Camera
DELVE	DECam Local Volume Exploration survey
DES	Dark Energy Survey
DESDM	DES Data Management
FWHM	Full Width at Half Maximum
MSTO	Main Sequence Turn-Of
NIST	National Institute of Standards and Technology
RA	Right Ascension
S/N	Signal-to-Noise Ratio
SBIG	Santa Barbara Instrument Group
SED	Spectral Energy Distribution
SDSS	Sloan Digitized Sky Survey
ΛCDM	Lambda Cold Dark Matter

TABLE OF CONTENTS

Page

ABSTRACT ii

DEDICATION iii

ACKNOWLEDGMENTS iv

CONTRIBUTORS AND FUNDING SOURCES vi

NOMENCLATURE ix

TABLE OF CONTENTS x

LIST OF FIGURES xiii

LIST OF TABLES xvii

1. INTRODUCTION 1

    1.1 Outline of Dissertation 4

2. THREE-DIMENSIONAL STRUCTURE OF THE SAGITTARIUS DWARF SPHEROIDAL CORE FROM RR LYRAE* 7

    2.1 Introduction 7
    2.2 Data 10
        2.2.1 Selection of data from *Gaia* DR2 variable catalog 10
        2.2.2 Selection of data from OGLE-IV RRab catalog 13
            2.2.2.1 Distance derivations for OGLE RR Lyrae 14
            2.2.2.2 Physically motivated cuts 15
    2.3 Methods 16
        2.3.1 Modeling the 3D properties of Sagittarius 16
            2.3.1.1 2D projection of a 3d ellipsoid 19
            2.3.1.2 Inclination of an ellipsoid 22
        2.3.2 Likelihood analysis 22
    2.4 Results 25
    2.5 Discussion and Conclusion 33

3. DELVE-ING INTO THE JET: A THIN STREAM ON A RETROGRADE ORBIT AT 30 KPC 35

3.1 Introduction 35
3.2 DELVE DR1 Data 39
3.2.1 *Gaia* cross-match with DELVE DR1 42
3.3 Methods and Analysis 42
3.3.1 Initial matched-filter Search 43
3.3.2 Distance Gradient 46
3.3.3 Creation of optimized matched-filter map 48
3.3.4 Fitting Stream Morphology 49
3.3.5 Proper Motion of the Jet Stream 51
3.3.5.1 Data Preparation 54
3.3.5.2 Mixture Model 55
3.4 Dynamical Modeling 59
3.5 Discussion 62
3.5.1 Properties of the Jet stream 62
3.5.2 Small-Scale Features 64
3.5.3 Stream Mass and Progenitor Properties 65
3.6 Conclusions 67

4. THE DEVELOPMENT AND TESTING OF TCal: A MOBILE SPECTROPHOTOMETRIC CALIBRATION UNIT FOR ASTRONOMICAL IMAGING SYSTEMS* 70

4.1 INTRODUCTION 70
4.2 EXPERIMENTAL SETUP 73
4.2.1 Light source 74
4.2.2 Coupling Optics 75
4.2.3 Filter Wheel 75
4.2.4 Monochromator 76
4.2.5 Fiber Bundle 77
4.2.6 Monitoring Spectrometer 77
4.2.7 Projection System 77
4.2.8 Flat Field Screen 77
4.2.9 Monitor CCD 78
4.2.10 Instrument Enclosure/Stand 79
4.3 SOFTWARE 79
4.3.1 Scan Software 80
4.3.1.1 Scan Initialization 80
4.3.2 Scan Procedure 81
4.3.3 Data Reduction Pipeline 82
4.4 TESTING OF PROTOTYPE 83
4.4.1 Stray Light At Blue Wavelengths 84
4.5 CONCLUSION 85

5. SUMMARY AND CONCLUSIONS 87

REFERENCES 89

APPENDIX A. 131
A.1 *Gaia* Queries 131
APPENDIX B. 132
B.1 Membership Probability 132

LIST OF FIGURES

FIGURE Page

2.1 *Left:* Density of all 8.5×10^6 Gaia sources in proper motion space. The solid red ellipse denotes a $1\,\sigma$ contour for the Sagittarius Gaussian component, and the solid blue line is the same for a Milky Way component. *Middle:* The green points show all sources from the *Gaia* DR2 variability catalog with a *best_classification* of RRab in the on sky region of Sagittarius. *Right:* The green points are the same as the left plot, but only the sources that pass our proper motion and magnitude cuts are plotted. The red ellipse shows the projected half light radius of Sagittarius found from RR Lyrae stars. 11

2.2 Shown is a kernel density estimate of *Gaia* RR Lyrae (points in right plot of Figure 2.1) as a function of angular position in the sky where yellow indicates a more dense region, and blue is less dense. $\Delta\theta_1$ and $\Delta\theta_2$ show the angular distance from the center of Sagittarius. The red ellipse indicates the projected half-light radius as Figure 2.1, and the black circle marks the center of the galaxy. 11

2.3 *Left:* The blue points show the on-sky spatial distribution of the 670 OGLE RR Lyrae used in our analysis. The red ellipse shows the same projected half-light radius as Figure 2.1, and the black outline shows the region where OGLE data was taken. *Right:* A histogram of heliocentric distance for all stars in left-hand plot. The median distance of Sagittarius RR Lyrae is marked with a dashed line. 13

2.4 Posterior probability densities resulting from the likelihood analysis. The top row shows the results for the principal axes (a, b, c) of the core of Sagittarius, and the bottom row shows the posteriors for the inclination with respect to earth ($i_{\rm earth}$) and with respect to the Galactic center ($i_{\rm Gal}$ as well as the Triaxiality (T) of the system. To illustrate how each of the datasets effects our results posteriors are shown for the individual fits of the *Gaia* (*blue*) and OGLE data (*red*), a fit of only the 2D information from the OGLE data (*grey*), and the joint fit of the two datasets (*green*). 27

2.5 Three dimensional plot showing the results of our analysis. The red points show the two dimensional location of *Gaia* RR Lyrae, and the blue ellipse indicates the half light radius derived from them. The black points show OGLE RR Lyrae where the grey lines indicate the uncertainty on the position of each star. The green ellipsoid shows the three dimensional half light radius of Sagittarius derived from the results of our analysis. The $\hat{z'}$ axis points towards the observer. The black arrow points towards the Galactic center..... 29

2.6 Posterior probability densities from a joint fit to the *Gaia* and OGLE data for the six baseline parameters of our model; a is the major axis scale length in *kpc*, p is the ratio of the intermediate to the major axis, and q is the ratio of the minor to the major axis. The angles are the Euler rotation angles as defined in Section 2.3 in units of degrees. 30

2.7 Histograms showing the distribution of OGLE RR Lyrae in different dimensions. For each panel the red (green) line shows the observed distribution of OGLE (*Gaia*) stars, the black line is the median of 1000 mock realizations drawn from the posteriors of our model, and the blue contours show 50% and 95% confidence intervals for the mock realizations. *Top row:* the panels show comparisons in x', y', z', and the radial distribution between the observed 3D positions of OGLE RR Lyrae and the model.*Bottom row:* the panels compare the observed on sky (α, δ) positions of *Gaia* RR Lyrae and the model..... 32

3.1 The DELVE DR1 region where our search was performed is shown in light blue. The additional region (the Jet Bridge) that was searched is shown as a light orange patch. The solid black line indicates the plane of the Milky Way ($b = 0$ °) and the two dashed lines indicate $b = \pm 10°$. 40

3.2 A stellar density map from the DELVE photometry showing the Jet stream at a distance modulus of $m - M = 17.28$ ($D_\odot = 28.6\,\mathrm{kpc}$). The orange points show the extent of the stream identified by Jethwa et al. (2018), and the blue points denote the new extent of the stream as detected in MSTO and BHB stars as determined in this study. The solid black line in the bottom right indicates the plane of the Milky Way ($b = 0°$), and the dashed line shows $b = 10°$. 44

3.3 *Top:* Jet stream density after applying the same matched-filter as Figure 3.2. Additionally, deviations from great circle path $\phi_2 = 0°$ are clearly seen. The orange points show the extent of the stream identified by Jethwa et al. (2018), and the blue points denote the new extent of the stream as detected in MSTO and BHB stars. For the range $\phi_1 < -12.7°$ or $> 10°$ the stream is only detected using BHB stars. *Bottom:* SFD dust map of the same region. The red dashed line shows the track of Jet. 45

3.4 *Left:* proper motions of candidate BHB stars along the Jet stream. The green box shows our proper motion selection for likely members. The Milky Way foreground is seen at $(\mu^{\star}_{\phi_1}, \mu_{\phi_2}) \sim (0, 2)$ mas/yr *Right:* on-sky distribution (top) and distances modulus (bottom) of candidate BHB stars that are likely associated with the Jet stream. The matched-filter stream track (Equation 3.2 is shown as green dashed line on the top plot, and the linear fit on distance modulus, $(m - M)$, of the candidate BHB stars (Equation 3.3) is shown as a green dashed line on the bottom plot. 47

3.5 Hess difference diagram created by subtracting a background region from the on-stream region. The main sequence of the Jet stream is clearly seen. The Dotter et al. (2008) isochrone we use for our analysis with a metallicity of [Fe/H]$=-1.57$ and age of $\tau = 12.1$ Gyr is shown as a solid black line. The red line shows the matched-filter used to create the optimized map shown in the top row of Figure 3.6. The left y-axis shows the absolute magnitude of sources and the right y-axis shows the corresponding apparent magnitude at $\phi_1 = 0^{\circ}$. 50

3.6 Modeling the track, width, and intensity of the Jet stream from DELVE DR1 photometric data. *Top:* The density of stars that pass the optimized matched-filter selection that takes into account the observed distance gradient in the region of the Jet stream. *Middle:* The maximum *a posteriori* (MAP) model of the data shown in the top panel containing both stream and background components. *Bottom:* The residual density map showing the observed density minus the model. 52

3.7 Measurement of Jet stream parameters as a function of position along the stream (ϕ_1) as derived from modeling the DELVE DR1 stellar density maps. From top to bottom are stream surface brightness, stream track, stream width, and linear density. The shaded area shows the 68% containment peak interval, and the black line shows the best-fit estimate of each parameter. 53

3.8 Selection of stars used to measure the proper motion of the Jet stream. *Left:* A color–magnitude diagram demonstrating the selection applied to the data. The orange lines show the empirical M92 horizontal branch and Dotter isochrone ([Fe/H] $=-1.57$) used to select data. The blue dashed lines show our selection range in distance, and the red dashed lines our selection range in color. *Center:* A color-color plot showing our selection range in blue around an empirical stellar locus of dereddened DES photometry in orange. *Right:* Proper motion in stream coordinates of the sample of stars passing all selection cuts. The signal from the Jet stream is easily seen at $(\mu^{\star}_{\phi_1}, \mu_{\phi_2}) \sim (-1, 0)$ mas/yr (circled in red). 55

3.9 Proper motion of high probability member RGB (red) and BHB (blue) stars ($p_{mem} > 0.8$). Additionally the line of best-fit proper motion is shown as a black dashed line. All the BHB stars used to measure the distance gradient are also high probability members. 58

3.10 Best-fit stream model to the Jet stream. In each row the dark blue points show the best-fit stream model and the red points show the observations to which the model was fit. *First row:* the on-sky distribution of the stream. *Second row:* the distance modulus of the stream. *Third and Fourth rows:* The reflex-corrected proper motions of the stream in ϕ_1 and ϕ_2 respectively. *Fifth row:* predicted heliocentric velocities of the stream. 63

4.1 Scan of optical filters used in the Carnegie Supernova Project (Marshall, 2016). This is similar to the expected data product of TCal. 72

4.2 Schematic of the TCal system. The large arrows on the right hand side show the direction that light travels through these components of the system. 74

4.3 Spectral Radiance of EQ-99x as measured in the lab by Energetiq 75

4.4 *Left:* A model of the light source, coupling optics, filter wheel and monochromator. *Right:* Image of the TCal system in the lab, including the enclosure and dedicated table. 76

4.5 *Left*: Reflectance measurements for the mixed nylon-spandex material from Schmidt *et al. in prep*,Schmidt (2018) note that it reflects well into the UV unlike other screen materials tested. Right: Image of 1.2 m screen. 78

4.6 Graphical Control for TCal scan written in LabView. 81

4.7 The results of our scan of ETSI mounted on the 0.9 m telescope at McDonald Observatory. The blue line shows our measurement the relative transmission as a function of wavelength for ETSI. The dashed line is a prediction of the bandpass solely taking into account the theoretical transmission functions of the Alluxa Quad filter and 435 nm long pass (LP) filter and our lab measured transmission function of the STF-8300M CCD. 84

LIST OF TABLES

TABLE Page

2.1 Assumed priors for our set of baseline model parameters. Parameters are defined in Section 2.3. 25

2.2 Results of our fits for the joint case as well as the *Gaia* only, OGLE only 2d (α, δ) and OGLE only 3d (α, δ, $D_\odot$) cases. The values are the median for each parameter, and the errors show the 68% confidence interval. Histograms showing the posteriors for a selection of these parameters is shown in Figure 2.4. For the joint fit the $r_{1/2,\,\mathrm{proj}} = 2.04\,\mathrm{kpc}$ corresponds to an on sky major axis of $269 \pm 21'$. 26

3.1 Results of the proper motion fit in reflex corrected proper motion coordinates . 59

3.2 Priors on the dynamical model 62

B.1 this table includes all stars with $p_i > 0.1$ for our analysis of the proper motion of the Jet stream. (This table is available in its entirety in machine-readable form.) (a) DELVE ID's are from the `QUICK_OBJECT_ID` column in DELVE-DR1, and Gaia IDs are from `SOURCE_ID` column in *Gaia* EDR3. (b) R.A. and Dec. are from Gaia EDR3 catalog (J2015.5 Epoch). (c) g, r band magnitudes are reddening corrected PSF photometry (`MAG_PSF_DERED`) from DELVE DR1 catalog. (d) The D_{ϕ_1} column gives the distance in kpc derived from equation 3.3, except for candidate bhb stars whose distances are estimated from their predicted absolute magnitude M_g as discussed in section 3.3.2 (e) The probability that a star is a member of the Jet stream. 133

B.1 this table includes all stars with $p_i > 0.1$ for our analysis of the proper motion of the Jet stream. (This table is available in its entirety in machine-readable form.) (a) DELVE ID's are from the `QUICK_OBJECT_ID` column in DELVE-DR1, and Gaia IDs are from `SOURCE_ID` column in *Gaia* EDR3. (b) R.A. and Dec. are from Gaia EDR3 catalog (J2015.5 Epoch). (c) g, r band magnitudes are reddening corrected PSF photometry (`MAG_PSF_DERED`) from DELVE DR1 catalog. (d) The D_{ϕ_1} column gives the distance in kpc derived from equation 3.3, except for candidate bhb stars whose distances are estimated from their predicted absolute magnitude M_g as discussed in section 3.3.2 (e) The probability that a star is a member of the Jet stream. 134

B.1 this table includes all stars with $p_i > 0.1$ for our analysis of the proper motion of the Jet stream. (This table is available in its entirety in machine-readable form.) (a) DELVE ID's are from the `QUICK_OBJECT_ID` column in DELVE-DR1, and Gaia IDs are from `SOURCE_ID` column in *Gaia* EDR3. (b) R.A. and Dec. are from Gaia EDR3 catalog (J2015.5 Epoch). (c) g, r band magnitudes are reddening corrected PSF photometry (`MAG_PSF_DERED`) from DELVE DR1 catalog. (d) The D_{ϕ_1} column gives the distance in kpc derived from equation 3.3, except for candidate bhb stars whose distances are estimated from their predicted absolute magnitude M_g as discussed in section 3.3.2 (e) The probability that a star is a member of the Jet stream. 135

B.1 this table includes all stars with $p_i > 0.1$ for our analysis of the proper motion of the Jet stream. (This table is available in its entirety in machine-readable form.) (a) DELVE ID's are from the `QUICK_OBJECT_ID` column in DELVE-DR1, and Gaia IDs are from `SOURCE_ID` column in *Gaia* EDR3. (b) R.A. and Dec. are from Gaia EDR3 catalog (J2015.5 Epoch). (c) g, r band magnitudes are reddening corrected PSF photometry (`MAG_PSF_DERED`) from DELVE DR1 catalog. (d) The D_{ϕ_1} column gives the distance in kpc derived from equation 3.3, except for candidate bhb stars whose distances are estimated from their predicted absolute magnitude M_g as discussed in section 3.3.2 (e) The probability that a star is a member of the Jet stream. 136

B.1 this table includes all stars with $p_i > 0.1$ for our analysis of the proper motion of the Jet stream. (This table is available in its entirety in machine-readable form.) (a) DELVE ID's are from the `QUICK_OBJECT_ID` column in DELVE-DR1, and Gaia IDs are from `SOURCE_ID` column in *Gaia* EDR3. (b) R.A. and Dec. are from Gaia EDR3 catalog (J2015.5 Epoch). (c) g, r band magnitudes are reddening corrected PSF photometry (`MAG_PSF_DERED`) from DELVE DR1 catalog. (d) The D_{ϕ_1} column gives the distance in kpc derived from equation 3.3, except for candidate bhb stars whose distances are estimated from their predicted absolute magnitude M_g as discussed in section 3.3.2 (e) The probability that a star is a member of the Jet stream. 137

B.1 this table includes all stars with $p_i > 0.1$ for our analysis of the proper motion of the Jet stream. (This table is available in its entirety in machine-readable form.) (a) DELVE ID's are from the `QUICK_OBJECT_ID` column in DELVE-DR1, and Gaia IDs are from `SOURCE_ID` column in *Gaia* EDR3. (b) R.A. and Dec. are from Gaia EDR3 catalog (J2015.5 Epoch). (c) g, r band magnitudes are reddening corrected PSF photometry (`MAG_PSF_DERED`) from DELVE DR1 catalog. (d) The D_{ϕ_1} column gives the distance in kpc derived from equation 3.3, except for candidate bhb stars whose distances are estimated from their predicted absolute magnitude M_g as discussed in section 3.3.2 (e) The probability that a star is a member of the Jet stream. 138

B.1 this table includes all stars with $p_i > 0.1$ for our analysis of the proper motion of the Jet stream. (This table is available in its entirety in machine-readable form.) (a) DELVE ID's are from the `QUICK_OBJECT_ID` column in DELVE-DR1, and Gaia IDs are from `SOURCE_ID` column in *Gaia* EDR3. (b) R.A. and Dec. are from Gaia EDR3 catalog (J2015.5 Epoch). (c) g, r band magnitudes are reddening corrected PSF photometry (`MAG_PSF_DERED`) from DELVE DR1 catalog. (d) The D_{ϕ_1} column gives the distance in kpc derived from equation 3.3, except for candidate bhb stars whose distances are estimated from their predicted absolute magnitude M_g as discussed in section 3.3.2 (e) The probability that a star is a member of the Jet stream. 139

B.1 this table includes all stars with $p_i > 0.1$ for our analysis of the proper motion of the Jet stream. (This table is available in its entirety in machine-readable form.) (a) DELVE ID's are from the `QUICK_OBJECT_ID` column in DELVE-DR1, and Gaia IDs are from `SOURCE_ID` column in *Gaia* EDR3. (b) R.A. and Dec. are from Gaia EDR3 catalog (J2015.5 Epoch). (c) g, r band magnitudes are reddening corrected PSF photometry (`MAG_PSF_DERED`) from DELVE DR1 catalog. (d) The D_{ϕ_1} column gives the distance in kpc derived from equation 3.3, except for candidate bhb stars whose distances are estimated from their predicted absolute magnitude M_g as discussed in section 3.3.2 (e) The probability that a star is a member of the Jet stream. 140

B.1 this table includes all stars with $p_i > 0.1$ for our analysis of the proper motion of the Jet stream. (This table is available in its entirety in machine-readable form.) (a) DELVE ID's are from the `QUICK_OBJECT_ID` column in DELVE-DR1, and Gaia IDs are from `SOURCE_ID` column in *Gaia* EDR3. (b) R.A. and Dec. are from Gaia EDR3 catalog (J2015.5 Epoch). (c) g, r band magnitudes are reddening corrected PSF photometry (`MAG_PSF_DERED`) from DELVE DR1 catalog. (d) The D_{ϕ_1} column gives the distance in kpc derived from equation 3.3, except for candidate bhb stars whose distances are estimated from their predicted absolute magnitude M_g as discussed in section 3.3.2 (e) The probability that a star is a member of the Jet stream. 141

B.1 this table includes all stars with $p_i > 0.1$ for our analysis of the proper motion of the Jet stream. (This table is available in its entirety in machine-readable form.) (a) DELVE ID's are from the `QUICK_OBJECT_ID` column in DELVE-DR1, and Gaia IDs are from `SOURCE_ID` column in *Gaia* EDR3. (b) R.A. and Dec. are from Gaia EDR3 catalog (J2015.5 Epoch). (c) g, r band magnitudes are reddening corrected PSF photometry (`MAG_PSF_DERED`) from DELVE DR1 catalog. (d) The D_{ϕ_1} column gives the distance in kpc derived from equation 3.3, except for candidate bhb stars whose distances are estimated from their predicted absolute magnitude M_g as discussed in section 3.3.2 (e) The probability that a star is a member of the Jet stream. 142

B.1 this table includes all stars with $p_i > 0.1$ for our analysis of the proper motion of the Jet stream. (This table is available in its entirety in machine-readable form.) (a) DELVE ID's are from the `QUICK_OBJECT_ID` column in DELVE-DR1, and Gaia IDs are from `SOURCE_ID` column in *Gaia* EDR3. (b) R.A. and Dec. are from Gaia EDR3 catalog (J2015.5 Epoch). (c) g, r band magnitudes are reddening corrected PSF photometry (`MAG_PSF_DERED`) from DELVE DR1 catalog. (d) The D_{ϕ_1} column gives the distance in kpc derived from equation 3.3, except for candidate bhb stars whose distances are estimated from their predicted absolute magnitude M_g as discussed in section 3.3.2 (e) The probability that a star is a member of the Jet stream. 143

1. INTRODUCTION

One of the great open questions in astronomy is how exactly did galaxies form and evolve to their present day state? Many of the broad strokes have been filled out, through a myriad of studies including observations of the cosmic microwave background, millions of galaxies, supernovae and comparisons to cosmological simulations. These analyses and many others have tested the ΛCDM (Dark Energy plus Cold dark Matter) paradigm and found its predictions to agree with observations at a stunningly high level (e.g. Planck Collaboration et al., 2020; Abbott et al., 2018; Riess et al., 2016). Even so there are still regions of parameter space where we can continue to test the predictions of ΛCDM, and alternative theories such as warm dark matter (Dodelson and Widrow, 1994), fuzzy dark matter (Hu et al., 2000), self interacting dark matter (Kaplinghat et al., 2016), or others are not fully ruled out. For many of these regions, the studies of resolved stars in the Milky Way provide unique information and constraints that are not available through studies of extragalactic objects (Ivezić et al., 2012).

The general model of Milky Way formation was first suggested by Eggen et al. (1962), based on the kinematics of 122 nearby metal poor stars, they presented the Milky Way as the result of gas falling towards the galactic center, collapsing into a rotating disk, and forming the major smooth components that we see today. This simple and smooth model of galaxy formation was then challenged by Searle and Zinn (1978) who used observations of globular clusters to suggest a much more stochastic and clumpy build up of the Milky Way. As theory developed, studies using simulations in ΛCDM also predicted an abundance of substructure accreting onto the Milky Way (e.g. Press and Schechter, 1974). This hierarchical formalism of ΛCDM, first stated by White and Rees (1978), predicts the accretion of dark matter subhalos onto the larger dark matter halo of the Milky Way. Since then, observations and simulations have continued to add to our dynamic and complex understanding of the Milky Way (e.g. Bovy et al., 2012b; Bullock and Boylan-Kolchin, 2017).

Of particular interest to the analyses contained in this dissertation, is the evolution in our understanding of the stellar halo of our Galaxy. The stellar halo is estimated to contain only $\sim 1\%$ of the stellar mass of the Milky Way ($M_{\star,halo} \sim 10^9 M_\odot$; Freeman and Bland-Hawthorn, 2002). But, the halo also appears to contain the most information about the detailed accretion history of the Milky Way (Helmi, 2020), and can provide constraints on ΛCDM (Bullock and Boylan-Kolchin, 2017). Prior to the discovery of a plethora of substructure, the halo was modeled as an old, metal poor, and smooth distribution of stars. Then, large scale surveys began to change how we view the stellar halo of the Milky Way.

These studies, for the first time, allowed us to identify halo stars in large enough numbers to begin to unravel the complexity of this Milky Way component. Since only 1 in 1000 stars belong to the halo in the solar neighborhood (Helmi, 2020), it was not until the advent of photometric surveys taking observations of millions of objects such as Two Micron All Sky Survey (2MASS; Skrutskie, 2006) or Sloan Digital Sky Survey (SDSS; York, 2000) that this component could be explored in depth. This explosion in knowledge can be illustrated in the cumulative number of known Milky Way satellites and stellar streams (tidally disrupting satellites and stellar clusters). Prior to SDSS ($\sim$ 2005) we knew of around 10 Milky Way satellites and 1 stellar stream. As of the writing of this dissertation, there are $\sim$ 60 candidate satellites and $\sim$ 70 candidate stellar streams (Private communications with A. Drlica Wagner and T.S. Li). Clearly, discoveries over the last 20 years have shown us just how inhomogeneous and clumpy the stellar halo is.

One of the ways that we have enabled these large scale surveys to discover this halo substructure is through precise calibrations to remove systemic photometric errors. With the DELVE survey I have worked on understanding and correcting for systematics in the survey data using comparisons to deeper more homogeneous datasets, zeropoint calibrations to reference catalogs, and the creation of maps of survey properties (Drlica-Wagner et al., 2021). These maps allow us to account and correct for inhomogeneous depth, conditions, and coverage improving the sensitivity of substructure searches using this survey data. In

addition to calibrations at the catalog level, DELVE has benefited from dedicated calibration observations done for the Dark Energy Survey (DES; DES Collaboration et al., 2016). DES has been especially sensitive to substructure (e.g. Bechtol et al., 2015; Shipp et al., 2018; Drlica-Wagner et al., 2020) in a large part because of the measurement and synoptic monitoring of the telescope + instrumental transmission function (DECal; Marshall, 2016), and real time monitoring of the atmospheric transmission function (aTmcam; Li et al., 2016). In the future, the Traveling Calibration instrument (TCal; Ferguson and DePoy, 2018), that I led the development for, will measure this instrumental transmission function at many telescopes, and putting them on a common photometric baseline. These measurements, will reduce systematic photometric errors introduced when combining data taken with multiple instruments and improve the sensitivity of future searches.

To fully exploit the information in the stellar halo it is important not only to identify substructure, but also to characterize this substructure. The astrometric survey *Gaia* has cataloged the proper motions of billions of stars (Gaia Collaboration et al., 2021), and combined with radial velocity surveys (e.g. Majewski et al., 2017; Conroy et al., 2019), or dedicated follow-up (e.g. Li et al., 2019) has given us 7D (3 positions + 3 velocities + chemical abundances) information for many halo stars and substructures. Using this 7D information, we can now put together a cohesive picture of the halo build up, and the accretion history of the Milky Way. Satellite galaxies are accreted, then tidally disrupted forming stellar streams and clouds. Subsequently, after a few dynamical timescales (few Gyr) these substructures become phase-mixed, no longer spatially coherent but identifiable based on stellar orbits and chemical signatures (e.g. Naidu et al., 2020; Bonaca et al., 2020).

Additionally, characterizing this substructure can be used to constrain the nature of our universe. The subject of near-field cosmology uses these substructures to place limits on the nature of dark matter, stellar formation, reionization, the sites of nucleosynthesis, and the environment in the early universe (Weisz and Boylan-Kolchin, 2019). One example among many are the limits place on the dark matter subhalo mass function, both through the

abundances of faint satellites (e.g. Nadler et al., 2021), and the complex morphologies of stellar streams (e.g. Banik et al., 2021). Because we can resolve structure at much smaller scales in our Galaxy than anywhere else this field promises to place some of the most stringent constraints on dark matter, galaxy formation and the evolution of the universe.

As discussed in the following subsection, the work in this dissertation mainly concerns itself with this characterization of substructure in order to better understand the nature of the Milky Way halo and calibrations of instruments involved in large scale surveys.

1.1 Outline of Dissertation

Here we outline the structure of the following dissertation. The general push of this work has been to use large scale surveys to characterize and better understand substructure of the Milky Way, such as dwarf galaxies and stellar streams. Additionally, we discuss the infrastructure and instrumentation work completed to enable precision science with large scale surveys.

In Chapter 2, we study the three dimensional geometry of the core of the Sagittarius dwarf spheroidal (dSph) using RR Lyrae (RRL) type variable stars as spatial tracers. RRL stars are old, metal poor and occur in abundance in Sagittarius. Additionally, with a well measured light curve (luminosity vs time) we can estimate the distance to an individual star very precisely. These two features taken together, the large number of RRL in Sagittarius and the small distance uncertainties for many of these RRL, allow us to constrain the three dimensional shape of the dSph. To do this we use data from two surveys that catalog RRL stars, OGLE and *Gaia* DR2. These two catalogs contain complimentary information on the nature of the Sagittarius core. The OGLE data only contains objects in the very center of the dSph, but has an extremely high detection efficiency (assumed to be $\sim 100\%$) over this area, and the light curves are well sampled allowing for photometric estimates of the metallicity of these stars which greatly increases the precision of distance estimates to these objects. On the other hand the *Gaia* catalog, which covers the entire spatial extent of Sagittarius, is less complete ($\sim$15%), and does not have well sampled light curves (meaning large uncertainties

on the distance to an individual star). Therefore, we can use the information in both datasets to fully constrain the shape of the core of Sagittarius. The OGLE data resolves the width along the line of sight, and the *Gaia* data constrains the projection of Sagittarius onto the plane of the sky. We develop a modeling framework to fit a three dimensional ellipsoid to the data finding a best finding a best-fit stellar distribution that is triaxial, with axis ratios of $1 : 0.76 : 0.43$. The measurements of this shape, along with kinematic (velocity) information can be used in future studies to distinguish between different dark matter distributions in the core of Sagittarius.

In Chapter 3, we study the Jet stream. This stellar stream is the remnant of a globular cluster that has been tidally disrupted by the Milky Way gravitational potential. Using the DECam Local Volume Exploration (DELVE) survey, a large photometric survey, and proper motions from *Gaia* EDR3 we characterize the nature of this stellar stream. A matched filter search using DELVE data plus candidate blue horizontal branch stars identified using DELVE photometry and *Gaia* proper motions reveal that the stellar stream extends at least 29 deg across the sky. Previously, only 11 deg of this stream was known. Then, we use the Blue Horizontal Branch (BHB) stars to measure a distance gradient along the stream of 0.2 kpc/deg with heliocentric distances ranging from $D_\odot = 27 - 34$ kpc. Next, the matched filter map created from DELVE photometry is used to simultaneously fit the stream track, width, and intensity of the stream to quantitatively characterize density variations in the Jet stream, including a large gap, and identify substructure off the main track of the stream. Furthermore, we report the first measurement of the proper motion of the Jet stream and find that it is well-aligned with the stream track suggesting the stream has likely not been significantly perturbed perpendicular to the line of sight. Finally, we fit the stream with a dynamical model and find that the stream is on a retrograde orbit, and is well fit by a gravitational potential including the Milky Way and Large Magellanic Cloud. These results indicate the Jet stream is an excellent candidate for future studies with deeper photometry, astrometry, and spectroscopy to study the potential of the Milky Way and probe perturbations from

baryonic and dark matter substructure.

Next, in Chapter 4 we discuss work on the Traveling CALibration unit (TCal). A mobile spectrophotometric calibration system to characterize the throughput as a function of wavelength of imaging systems. These measurements will enhance the science return from follow-up observations of imaging surveys such as the Dark Energy Survey (DES), the Rubin Observatory Legacy Survey of Space and Time (LSST), and the Zwicky Transient Factory (ZTF) by placing all calibrated systems on a common photometric baselines. This calibration is completed using a monochromator based tunable light source to project narrow-band light ($\sim$ 1 mm) on a screen that is measured both by the system to be calibrated and a previously calibrated monitor CCD. Then the ratio of these two measurements gives a relative measure of throughput as a function of wavelength including contributions from the telescope, optics, filters, windows, and detector. In this chapter we focus the hardware and software development of this system. This calibration will be performed on numerous 1-8m telescopes that expect devote time towards survey follow-up. This set of calibrations will reduce the systematic errors due to small differences in bandpass that are introduced when combining data products from multiple observatories making follow-up efforts more precise and accurate.

Finally, in Chapter 5 we summarize the work presented in this dissertation and conclude with a few possible next steps.

2. THREE-DIMENSIONAL STRUCTURE OF THE SAGITTARIUS DWARF SPHEROIDAL CORE FROM RR LYRAE*

2.1 Introduction

Precise measurements of distances to member stars have provided important information on the three-dimensional structure of the Sagittarius dwarf galaxy and its associated stellar stream. The stream has now been mapped out over the full sky by determining the distances to M-giants (Majewski et al., 2003a), main-sequence, horizontal branch, red giants (Niederste-Ostholt et al., 2010; Koposov et al., 2012; Slater et al., 2013; Belokurov et al., 2014), and RR Lyrae (Sesar et al., 2017; Hernitschek et al., 2017). These measurements now show that the leading and the trailing arms of the stream extend $\sim 20 - 120$ kpc from the main body. The three-dimensional structure of the stream is a necessary input to simulations which attempt to understand its origin (Law and Majewski, 2010a; Peñarrubia et al., 2011; Dierickx and Loeb, 2017). The phase-space structure of the stream may also provide new probes of exotic physics in the dark matter sector (Kesden and Kamionkowski, 2006; Xu and Randall, 2019).

In addition to the stream, the structure of the core provides important information on the nature and evolution of Sagittarius. The first in-depth photometric and kinematic study by Ibata et al. (1997) found a half-light radius for the core of ~ 1 kpc, and an average line-of-sight velocity dispersion of ~ 11 km/s. Distance estimates to red clump stars indicate that the ratios of the major, intermediate, and minor axes are 1:0.33:0.33. The line-of-sight velocity dispersion is now measured out to several half-light radii, and is $\sim 10 - 15$ km/s, with a cold spot in the central region (Frinchaboy et al., 2012; Majewski et al., 2013).

*This chapter is a pre-copyedited, author-produced version of an article accepted for publication in the Monthly Noticies of the Royal Astronomical Society following peer review. The version of record is located in MNRAS, Volume 495, Issue 4, July 2020, Pages 4124–4134, and is available online at: https://doi.org/10.1093/mnras/staa1404. This use follows their self archiving policy.

Understanding the dynamical structure of both the core and the stream has important implications for constraining the progenitor of Sagittarius and its dark matter properties. It has long been known that the observed geometry of the leading and trailing arms of the streams imply that the progenitor resides in a more massive and extended dark matter halo (Johnston et al., 1995; Ibata and Lewis, 1998). Matching the recent kinematic data in the streams implies that the progenitor mass is $\gtrsim 6 \times 10^{10}$ $M_\odot$ (Gibbons et al., 2017). Similarly, in order to match the kinematics in the core, simulations suggest that the total stellar plus dark matter mass of the progenitor was $\gtrsim 10^{10}$ $M_\odot$ (Łokas et al., 2010). The nature of the progenitor may also be constrained from the lack of rotation signal in the central core (Peñarrubia et al., 2011).

Measuring the shape and the orientation of dwarf satellite galaxies like Sagittarius is important from the perspective of the ΛCDM theory of structure formation. Dark matter only simulations of tidally-disrupting satellites find that heavily-stripped subhalos tend to be rounder than those that are less tidally disturbed (Kuhlen et al., 2007; Barber et al., 2015). These simulations also find that the major axes of the subhalos tend to align towards the center of the host dark matter halo. This effect is most pronounced in the outer regions of the subhalo; it is not yet clear how baryons alter both the shapes and the orientations of the subhalos.

The kinematics of the Sagittarius core may be used to determine the dark matter mass distribution in this region. Assuming that the system is in dynamical equilibrium, the mass distribution may be extracted using methods that are typically used on dwarf spheroidal galaxies (Battaglia et al., 2013). However, all of these methods are limited because the inputs to them are derived from projected quantities such as the surface density or velocity dispersion. Since it is the three-dimensional stellar density profile that must be used in the dynamical models, an incorrect input for it may bias the reconstructed luminous and dark mass distributions. For example, in the simplest case of spherically-symmetric stellar distributions, there is a non-unique mapping from projected two-dimensional stellar distri-

bution onto a three-dimensional stellar density distribution. In particular, an observed flat two-dimensional stellar profile may project onto either a central core or a central cusp in three dimensions, and this has important implications for extracting the dark matter distribution (Strigari et al., 2010). Distance information on individual stars would provide an important new input to constrain dynamical models (Richardson et al., 2014).

For axisymmetric models, the extraction of the three-dimensional stellar profile from the two-dimensional data is even more difficult. This is because of the projection issue that plagues spherical models, and even more importantly because there is an inclination angle of the major (or minor) axis with respect to the sky plane that must be determined. Only with a measurement of this inclination is it possible to obtain the three-dimensional velocity dispersion from the measured two-dimensional dispersions, and estimate the dark matter distribution (e.g. Hayashi and Chiba (2015))

Obtaining an empirical three-dimensional stellar distribution requires a precise measurement of the distance to individual member stars. However because of the relatively large distances to a typical dwarf spheroidal galaxy, and the fact that the distances to the majority of their member stars cannot be precisely measured, obtaining a three-dimensional profile is difficult. Previously, Sagittarius has had its line-of-sight width measured using the same OGLE-IV dataset as our analysis (Hamanowicz et al., 2016), but only the Magellanic Clouds have had their complete three-dimensional structure directly measured from samples of RR Lyrae stars (Deb, 2017; Deb et al., 2018).

In this paper, we make the first measurement of the complete three-dimensional structure of the core of Sagittarius. We use two samples of RR Lyrae: one from the OGLE-IV bulge survey and one from *Gaia* DR2. The OGLE data have precise three-dimensional positions, and so contain information on the three-dimensional stellar distribution in the core. The *Gaia* sample of RR Lyrae do not have precise distances, but they form the most homogenous and spatially complete sample of RR Lyrae in Sagittarius. Therefore they contain information on the projection of Sagittarius onto the two-dimensional sky plane.

To fit the data we model the core as a full triaxial ellipsoid. We constrain the scale lengths of the spheroid and the inclination using the three-dimensional information from the OGLE data. We project the spheroid onto the two-dimensional sky plane, and use the *Gaia* data to obtain independent constraints on the scale lengths. We will show that the strongest constraints on the scale lengths and the inclination of the core are obtained with a joint analysis of the OGLE and *Gaia* data.

This paper is organized as follows. In section 2.2 we describe in detail the *Gaia* DR2 and OGLE-IV data, and discuss the cuts that we implement to obtain our final RR Lyrae sample. In section 2.3 we outline our formalism for measuring the shape of the stellar distribution, and describe the statistical methodology used to compare different models. In section 2.4 we present the results of our analysis, and in section 2.5 we end with conclusions and discussion.

2.2 Data

In this section we describe the selection of our data samples from the *Gaia* and the OGLE catalogs, and our determination of the distances to the stars and their associated errors.

2.2.1 Selection of data from *Gaia* DR2 variable catalog

We use data from the second data release (Gaia Collaboration et al., 2018a) from the *Gaia* mission (Gaia Collaboration et al., 2016b) to identify the 2D positions of a sample of RRab stars that are consistent with being members of Sagittarius. The *Gaia* parallaxes are not measured well enough to obtain the distance precision required to constrain the 3D structure of Sagittarius. However, this dataset is much more spatially extended than the OGLE dataset. As we show below the larger spatial extent of these data allow us to obtain constraints on the three-dimensional properties that are complementary to the OGLE data.

To obtain a clean sample of *Gaia* candidate RR Lyrae we start by using the full DR2 catalog to determine the appropriate proper motion cut to apply. We select all stars in *Gaia* DR2 with a measured parallax ($\bar{\omega}$) of $< 1\,\mathrm{mas}$ that are within the core region of Sagittarius, defined by a right ascension (α) and declination (δ) of $279^\circ < \alpha < 291^\circ$ and

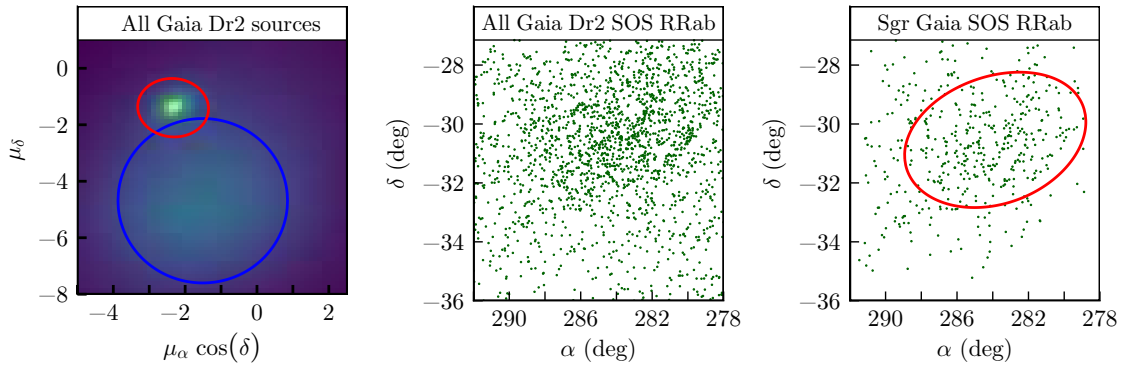

Figure 2.1 *Left:* Density of all 8.5×10^6 Gaia sources in proper motion space. The solid red ellipse denotes a $1\,\sigma$ contour for the Sagittarius Gaussian component, and the solid blue line is the same for a Milky Way component. *Middle:* The green points show all sources from the *Gaia* DR2 variability catalog with a *best_classification* of RRab in the on sky region of Sagittarius. *Right:* The green points are the same as the left plot, but only the sources that pass our proper motion and magnitude cuts are plotted. The red ellipse shows the projected half light radius of Sagittarius found from RR Lyrae stars.

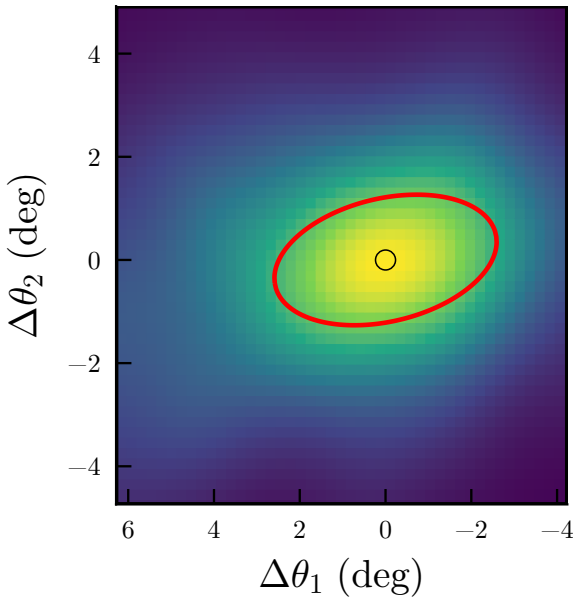

Figure 2.2 Shown is a kernel density estimate of *Gaia* RR Lyrae (points in right plot of Figure 2.1) as a function of angular position in the sky where yellow indicates a more dense region, and blue is less dense. $\Delta\theta_1$ and $\Delta\theta_2$ show the angular distance from the center of Sagittarius. The red ellipse indicates the projected half-light radius as Figure 2.1, and the black circle marks the center of the galaxy.

$-40^\circ < \delta < -20^\circ$, respectively (See Appendix A.1 for the query that we use). This selection criteria produce a sample of 8.5×10^6 sources which we use to determine the proper motion of Sagittarius. The left panel of Figure 2.1 shows a 2D density histogram of the proper motions of these sources. A bimodal distribution can clearly be seen with a broad component due to the Milky Way and a much narrower one due to Sagittarius.

In order to determine the proper motion cut necessary to separate stars that are associated with Sagittarius from those that are likely associated with the Milky Way we fit a simple two Gaussian mixture model to the data. We define $\boldsymbol{\mu}$ as the centroid of the Sagittarius component, the components dispersion as $\boldsymbol{\sigma} = (\sigma_{\rm major}, \sigma_{\rm minor})$, and a rotation by θ, the angle between the $\mu_\alpha \cos(\delta)$ axis and the $\sigma_{\rm major}$ axis. The left panel of Figure 2.1 also shows the two-dimensional Gaussian model fit to the proper motion of these sources. The blue ellipse shows the 1σ best-fit component for the Milky Way population, and the red ellipse marks the 1σ best fit parameters for the Sagittarius component. For the Sagittarius component we find best-fit values of $\boldsymbol{\mu} = (-2.34, -1.40)\,[\mathrm{mas/yr}]$, $\sigma_{major} = 0.52\,[\mathrm{mas/yr}]$, $\sigma_{minor} = 0.49\,[\mathrm{mas/yr}]$, and $\theta = 17.7\,[\mathrm{deg}]$. The mean proper motion of the Sagittarius component is consistent with the results of Gaia Collaboration et al. (2018b) and Fritz et al. (2018). We use these proper motion fit parameters below to identify RRab stars from the *Gaia* sample that are members of Sagittarius.

Next we query the *Gaia* Specific Objects Study (SOS) catalog (Clementini et al., 2019) to obtain the sample of stars classified as RRab stars in the region of Sagittarius. Quality cuts are applied on the RRL catalog following Iorio and Belokurov (2018). This sample is shown in the middle panel of Figure 2.1. To select candidate RR Lyrae that are consistent with being Sagittarius members we apply a proper motion cut based on the fit to all sources in the area. Only stars with proper motions within 2σ of the Saggitarius mean proper motion are kept. We further remove all stars within the tidal radius of M54 as identified in Hamanowicz et al. (2016) ($\alpha = 283.76^\circ,\ \delta = -30.48^\circ,\ r_{\rm tidal} = 7'.5$). Additionally, we apply a raw magnitude cut of $M_G > 16.8$ to remove any Milky Way foreground. This cleaned

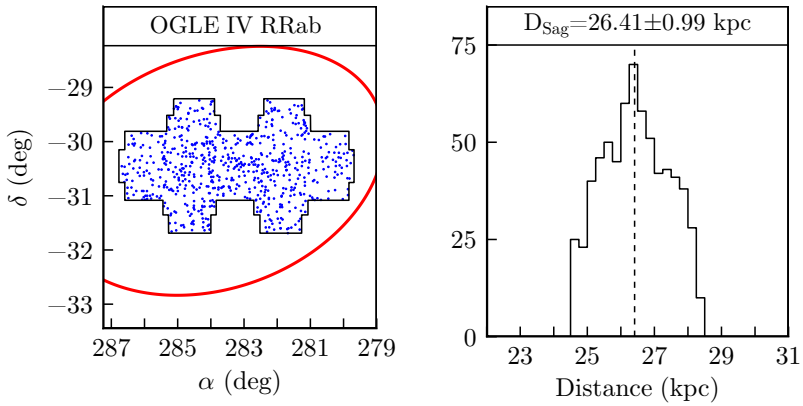

Figure 2.3 *Left:* The blue points show the on-sky spatial distribution of the 670 OGLE RR Lyrae used in our analysis. The red ellipse shows the same projected half-light radius as Figure 2.1, and the black outline shows the region where OGLE data was taken. *Right:* A histogram of heliocentric distance for all stars in left-hand plot. The median distance of Sagittarius RR Lyrae is marked with a dashed line.

sample is shown in the right panel of Figure 2.1.

Finally, the positions of these stars are converted from (α, δ) to Sagittarius-centered coordinates (ρ, ϕ), where ρ is the angular separation between a star at (α, δ), the centroid of Sagittarius (α_0, δ_0), and ϕ is the position angle of a star with respect to the centroid. The points are then projected onto an angular plane similar to equations 1-4 in van der Marel and Cioni (2001). Next, we perform a Gaussian kernel density estimate (KDE) with a 1 deg^2 window as a rough check on the distribution of these stars. This KDE in Figure 2.2 shows a density spike at the location of Sagittarius that drops off in a manner consistent with being Gaussian. We apply a rectangular cut of $-4.2 < \Delta\theta_1[\mathrm{deg}] < 6.2$ and $-4.7 < \Delta\theta_2[\mathrm{deg}] < 4.9$ where only the 482 stars within this area are used in our analysis.

2.2.2 Selection of data from OGLE-IV RRab catalog

We use the OGLE-IV Bulge (Udalski et al., 2015) catalog of fundamental mode RR Lyrae variable stars (RRab, Soszyński et al. 2014; Hamanowicz et al. 2016) for the 3D portion of our analysis. We clean the sample and derive distances to the RR Lyrae in the same manner as Jacyszyn-Dobrzeniecka et al. (2017) and Skowron et al. (2016) which we describe below.

2.2.2.1 Distance derivations for OGLE RR Lyrae

The distances to our RR Lyrae are derived using the same methodology as Jacyszyn-Dobrzeniecka et al. (2017). The process is briefly summarized and a few important equations are included in this section.

Starting from the OGLE-IV bulge catalog all objects with no measurements of the V-band magnitude or the Fourier coefficient combination ϕ_{31}^{I} are removed. Next, stars with atypically small peak-to peak I-band amplitudes are excluded (where $A_I < 5 \times Log(P) - 1$).

For the remaining stars we estimate the metallicity ([Fe/H]) of each star photometrically using the period (P) and (ϕ_{31}^{I}). Following Skowron et al. (2016) the ϕ_{31}^{I} catalog values plus the appropriate π offset are converted to ϕ_{31}^{V} (Equation 2.1), which are then converted to ϕ_{31}^{Kep} (Jeon et al. (2014), Equation 2.2). Then, the empirical relation from Nemec et al. (2013) (Equation 2.3) is used to get ([Fe/H]) on the Jurcsik (1995) scale. This metallicity is then converted to the Carretta et al. (2009) scale (Kapakos et al. (2011) Equation 2.4). Subsequently, the Braga et al. (2015) Period-Luminosity-Metallicity (PLZ) relation for $W_{I,V-I,abs}$ is applied to derive the absolute Wesenheit magnitude (Equation 2.5). The observed Wesenheit magnitude (Madore, 1976) is given by Equation 2.6. Finally, we use Equation 2.7 to estimate a distance in pc to each RR Lyrae.

$$\phi_{31}^{V} = 0.122(\phi_{31}^{I})^2 - 0.75(\phi_{31}^{I}) + 5.331 \tag{2.1}$$

$$\phi_{31}^{Kep} = \phi_{31}^{V} + 0.174 \tag{2.2}$$

$$[\mathrm{Fe/H}]_{\mathrm{J}} = -8.65 - 40.12\,P + 5.96\,\phi_{31}^{Kep} + 6.27\,\phi_{31}^{Kep}\,P - 0.72(\phi_{31}^{Kep})^2 \tag{2.3}$$

$$[\mathrm{Fe/H}]_{\mathrm{C}} = 1.001\,[\mathrm{Fe/H}]_{\mathrm{J}} - 0.112 \tag{2.4}$$

$$W_{I,V-I,abs} = -1.039 + -2.524\,Log(P) + 0.147([\mathrm{Fe/H}]_{\mathrm{C}} + 0.04) \tag{2.5}$$

$$W_{I,V-I} = I - 1.55\,(V - I) \tag{2.6}$$

$$D_{\odot} = 10^{(W_{I,V-I} - W_{I,V-I,abs})/5+1} \tag{2.7}$$

We estimate the uncertainty on these distance measurements as follows. The statistical component is due to the accuracy of mean brightness in the I-band and V-band. From Udalski et al. (2015) the mean accuracy of these measurements is $\sigma_{I,V} = 0.02$ mag, and the systematic uncertainty is introduced from the calculation of [Fe/H] and the Braga et al. (2015) Period Luminosity Metallicity (PLZ) relation. Similar to Jacyszyn-Dobrzeniecka et al. (2017) we take total uncertainty to be 3% of the distance to a star.

2.2.2.2 Physically motivated cuts

After cleaning the catalog and deriving distances we make cuts to remove Milky Way foreground/background stars. First, the same proper motion cut discussed in the previous section is applied. Next, we select all RRab stars with $279.6^{\circ} < \alpha < 286.7^{\circ}$ and $-31.7^{\circ} < \delta < -29.23^{\circ}$ near the core of Sagittarius. Then, a cut is applied to remove stars with large radial distances from the core ($r > 2$ kpc). This cut is implemented by defining D_{min} (D_{max}) which corresponds to the minimum (maximum) heliocentric distance of a star with $r < 2$ kpc and removing all stars with distances outside of $D_{\mathrm{min}} < D < D_{\mathrm{max}}$.

We define the center of Sagittarius to be $\alpha_0 = 283.83°$, $\delta_0 = -30.55°$ (Hamanowicz et al., 2016; McConnachie, 2012) and the distance to be the median distance of our sample $D_0 = 26.41$ kpc. This distance differs from Hamanowicz et al. (2016) who found $D_0 = 26.98$ kpc due to the slightly different method of distance estimation to the RR Lyrae (we are using Wesenheit magnitudes instead of I-band magnitudes). Finally, member stars of the globular cluster M54 are removed in the same manner detailed above. The positions and distances of the 721 RR Lyrae stars that compose our clean sample are shown in Figure 2.3.

Additionally, prior to our analysis we compare the *Gaia* sample to the OGLE sample to check the *Gaia* sample for completeness and contamination. From Clementini et al. (2019) the *Gaia* SOS catalog is 15% complete with 9% contamination in the OGLE bulge fields for RRab, RRc, and RRd stars. To get a sense of the completeness and contamination in our sub-sample, which is much fainter on average ($\langle M_G \rangle = 18.14$) than the full OGLE bulge catalog, we cross-match the cleaned *Gaia* SOS catalog with the less extended, but more complete and pure OGLE Sgr sample. There are 123 stars in common between the two datasets. We find that for this much smaller sample the *Gaia* catalog is 15% complete with 2% contamination and importantly has no obvious spatial structure in the completeness or the contamination. Due to the low contamination rate and absence of artificial structure in the data, we assume the distribution is unbiased, and can be used to infer projected properties of the Sagittarius dwarf galaxy.

2.3 Methods

In this section we present a model for the 3D properties of the RRab distribution in the Sagittarius core. We then move on to define the likelihood functions that we use for inference with both the 2D *Gaia* DR2 data and 3D OGLE data.

2.3.1 Modeling the 3D properties of Sagittarius

We define an inertial coordinate system centered on Sagittarius such that $\hat{x}$ is aligned along the major axis, $\hat{y}$ along the intermediate axis, and $\hat{z}$ along the minor axis. In this

coordinate system, we model the 3D stellar distribution of RR Lyrae as a Gaussian,

$$\rho_{RRL} = \rho_0 \exp\left(-\frac{1}{2}\left[\frac{x^2}{a^2} + \frac{y^2}{b^2} + \frac{z^2}{c^2}\right]\right), \tag{2.8}$$

where a, b, c are the scale lengths of the density distribution in the respective coordinate directions, and ρ_0 is a scale density. The radius along the major axis for any location is then given by $r = \sqrt{x^2/a^2 + y^2/b^2 + z^2/c^2}$. For this three-dimensional Gaussian density distribution, the half-light radius along the major axis is given by $1.56 \times a$. We choose the Gaussian form in Equation 2.8 because its physical interpretation is straightforward, and also because its analytic properties can be readily determined in convolutions that we perform below.

From the scale lengths (a, b, c), we can define the triaxility, T, in terms of the axis ratios $p = b/a$ and $q = c/a$

$$T = \frac{1 - p^2}{1 - q^2}. \tag{2.9}$$

For $T = 0$, the shape of the system is an oblate spheroid ($a = b > c$), while for $T = 1$ the system is a prolate spheroid ($a > b = c$).

In order to connect to an observer-based coordinate system, we define a separate right-handed "primed" coordinate system centered on Sagittarius. We convert the observed positions of the RR Lyrae to cylindrical coordinates in the plane of the sky, (ρ, ϕ), as described in van der Marel and Cioni (2001). We similarly define our coordinate system such that the $\hat{x}'$ axis points anti-parallel to the right ascension axis, the $\hat{y}'$ points parallel to the declination axis and the $\hat{z}'$ axis to points towards the observer on Earth. These transformations from

(ρ, ϕ, D) to (x', y', z') are given by

$$\begin{aligned} x' =& D \ \sin \ \rho \cos\phi \\ y' =& D \ \sin \ \rho \sin\phi \\ z' =& D_0 - D \ \cos \ \rho \end{aligned}$$

with D defined as the distance to a star and D_0 as the distance to the galaxy.

To then transform from the inertial Sagittarius coordinate system to this observed frame we follow a similar formalism to Sanders and Evans (2017). The transformation matrix between the coordinates is defined as the Euler rotation $\boldsymbol{R}(\alpha, \beta, \kappa) = \boldsymbol{R}_z(\alpha)\boldsymbol{R}_x(\beta)\boldsymbol{R}_z(\kappa)$, with the rotation matrices defined as

$$\boldsymbol{R}_z(\omega) = \begin{bmatrix} \cos(\omega) & -\sin(\omega) & 0 \\ \sin(\omega) & \cos(\omega) & 0 \\ 0 & 0 & 1 \end{bmatrix}, \tag{2.10}$$

$$\boldsymbol{R}_x(\omega) = \begin{bmatrix} 1 & 0 & 0 \\ 0 & \cos(\omega) & \sin(\omega) \\ 0 & \sin(\omega) & \cos(\omega) \end{bmatrix} \tag{2.11}$$

For the inertial $(\boldsymbol{x})$ to observed $(\boldsymbol{x'})$ transformation similar to Xu and Randall (2019) we define the observer to be located in the direction

$$\hat{z}' \equiv \sin\theta\cos\phi\,\hat{x} + \sin\theta\sin\phi\,\hat{y} + \cos\theta\,\hat{z}$$

Then if (x', y', z') is the right handed coordinate system defined above the total transformation is $\boldsymbol{R}_{\text{int,obs}} = \boldsymbol{R}(\gamma, \pi/2 - \phi, \theta)$ where γ is a rotational degree of freedom in the plane of

the sky. Written out the transformation is

$$\begin{bmatrix} x' \\ y' \\ z' \end{bmatrix} = \begin{bmatrix} \cos\gamma & -\sin\gamma & 0 \\ \sin\gamma & \cos\gamma & 0 \\ 0 & 0 & 1 \end{bmatrix} \times \begin{bmatrix} \sin\phi & -\cos\phi & 0 \\ \cos\theta\cos\phi & \cos\theta\sin\phi & -\sin\theta \\ \sin\theta\cos\phi & \sin\theta\sin\phi & \cos\theta \end{bmatrix} \begin{bmatrix} x \\ y \\ z \end{bmatrix}. \tag{2.12}$$

From the above definitions we must compute the projected properties of the galaxy in order to compare with the *Gaia* sample. The formalism to obtain the projected positions is similar to Sanders and Evans (2017); for our analysis we are particularly interested in expressing the result in terms of the projected major axis $a_{\rm proj}$, the minor axis $b_{\rm proj}$, the observed ellipticity $\epsilon = 1 - b_{\rm proj}/a_{\rm proj}$, and the position angle between observed North and the projected major axis *P.A.*. In Section 2.3.1.1 we derive the relation between a 3D ellipsoid and these 2D parameters.

2.3.1.1 2D projection of a 3d ellipsoid

Initially our ellipsoid can be described in its inertial frame by the following equation $\frac{x^2}{a^2} + \frac{y^2}{b^2} + \frac{z^2}{c^2} = 1$. In matrix form:

$$E = \begin{bmatrix} a^{-2} & 0 & 0 \\ 0 & b^{-2} & 0 \\ 0 & 0 & c^{-2} \end{bmatrix}$$

and

$$\begin{bmatrix} x & y & z \end{bmatrix} E \begin{bmatrix} x \\ y \\ z \end{bmatrix} = 1.$$

we then rotate this ellipse into the observed frame see Equation 2.12.

$$T(\gamma, \pi/2 - \phi, \theta)^{\mathrm{T}} \begin{bmatrix} a^{-2} & 0 & 0 \\ 0 & b^{-2} & 0 \\ 0 & 0 & c^{-2} \end{bmatrix} T(\gamma, \pi/2 - \phi, \theta) = \begin{bmatrix} A_{11} & A_{12} & A_{13} \\ A_{21} & A_{22} & A_{23} \\ A_{31} & A_{32} & A_{33} \end{bmatrix} = 1 \tag{2.13}$$

The conic section equation is given by:

$$\begin{aligned} f(x', y', z') =& A_{11}x'^2 + A_{22}y'^2 + A_{33}z'^2 \\ &+ 2A_{12}x'y' + 2A_{13}x'z' + 2A_{23}y'z' \\ =& 1 \end{aligned} \tag{2.14}$$

The ellipse formed by the *shadow* of this ellipsoid on the observed $x'y'$ plane is defined as the set of points where the z' component of $\nabla f(x', y', z') = 0$.

$$\begin{aligned} \frac{\mathrm{df}}{\mathrm{dz}} &= 2A_{33}z' + 2A_{13}x' + 2A_{23}y' = 0 \\ z' &= \frac{-A_{13}x' - A_{23}y'}{A_{33}} \end{aligned}$$

plugging this into equation 2.14 gives the conic section equation

$$\begin{aligned} 1 = A_{11}x'^2 + A_{22}y'^2 + A_{33}\left(\frac{-A_{13}x' - A_{23}y'}{A_{33}}\right)^2 + 2A_{12}x'y' \\ + 2A_{13}\frac{-A_{13}x' - A_{23}y'}{A_{33}}x' + 2A_{23}\frac{-A_{13}x' - A_{23}y'}{A_{33}}y' \end{aligned}$$

Grouping like terms gives

$$0 = -1 + \left(A_{11} - \frac{A_{13}^2}{A_{33}}\right)x'^2 + \left(2A_{12} - 2\frac{A_{13}A_{23}}{A_{33}}\right)x'y' + \left(A_{22} - \frac{A_{23}^2}{A_{33}}\right)y'^2$$

This is the canonical conic section equation with D & E equal to 0.

$$Ax'^2 + Bx'y' + Cy'^2 + Dx + Ey + F = 0$$

We then define a normalization factor (K) and the linear eccentricity or the distance of the focus from the center of the ellipse (s).

$$K = 64\,F\,(4\,A\,C - B^2)/(4\,A\,C - B^2)^2 \tag{2.15}$$

$$s = \frac{1}{4}\sqrt{|\,K\,|\,\sqrt{B^2 + (A-C)^2}} \tag{2.16}$$

From here we can write relations for the semi-major ($a_{\rm proj}$) and semi-minor ($b_{\rm proj}$) axes.

$$a_{\rm proj} = \frac{1}{8}\sqrt{2|K|\sqrt{B^2 + (A-C)^2 - 2q(A+C)}} \tag{2.17}$$

$$b_{\rm proj} = \sqrt{a_{\rm proj}^2 - s^2} \tag{2.18}$$

and the projected position angle ($P.A.$) is given by

$$P.A. = \frac{3\pi}{2} - \frac{1}{2}\text{atan2}\left(\frac{b}{a-c}\right) \tag{2.19}$$

2.3.1.2 *Inclination of an ellipsoid*

Finally, we are interested in the inclination of Sagittarius with respect to both an Earth-based observer and one at the Galactic Center. To measure this we define the inclination angle (i) to be the dot product of the unit vector pointing along the major axis ($\hat{\mathbf{a}}$) and the vector that points from Sgr to the observer ($\hat{\mathbf{u}}$). Then the inclination is defined by $cos(i + \pi/2) = \hat{\mathbf{a}} \cdot \hat{\mathbf{u}}$ where $i = 0$ indicates the major axis of Sgr is in the plane of the sky with respect to an observer. For an Earth-based observer in the ($\prime$) frame $\hat{\mathbf{u}}_{earth} = [0, 0, 1]$ and we take the distance between the sun and the Galactic Center to be 8.17 *kpc* (Gravity Collaboration et al., 2019) giving a $\hat{\mathbf{u}}_{GC} = [-0.11, 0, 0.99]$.

2.3.2 Likelihood analysis

With the model for Sagittarius outlined above, we now move on to discussing our likelihood analysis. Our likelihood analysis will involve a separate analysis of the 2D *Gaia* and the 3D OGLE data, as well as a joint analysis of these data sets.

We define the 2D and 3D data vectors as $\mathcal{D}_{2D}$ and $\mathcal{D}_{3D}$, respectively. We use these data sets to constrain our model parameters, which we take as the 3D parameters, $\mathbf{\Theta}_{3D} = [a, p, q, \gamma, \phi, \theta]$, defined as above. We choose to use the 3D parameters as our base set of model parameters in order to analyze the 2D and 3D data in a consistent manner. The probability for the model parameters given the $\mathcal{D}_{3D}$ data is $P(\mathbf{\Theta}_{3D} \,|\, \mathcal{D}_{3D})$, and similarly the probability for the model parameters given the $\mathcal{D}_{2D}$ data is $P(\mathbf{\Theta}_{3D} \,|\, \mathcal{D}_{2D})$.

Starting with the 2D case we need to derive an expression for $P(\mathbf{\Theta}_{3D} \,|\, \mathcal{D}_{2D})$. In this case the data vector $\mathcal{D}_{2D}$ is given in the primed coordinates defined in the frame of the observer. We start by writing the observed Cartesian position of a star when projected into the $z' = 0$ plane as $\boldsymbol{x}'^T = [x', y', 0]$. Then given the Gaussian model for the core of Sagittarius the probability of a single star being observed at location $\boldsymbol{x}'$ is

$$P(\boldsymbol{x}' \,|\, \mathbf{\Theta}_{3D}) = \mathcal{N}(\boldsymbol{x}' \,|\, \langle \boldsymbol{x}' \rangle_{\rm Sgr}, \boldsymbol{C}_{\rm proj}). \tag{2.20}$$

where $\mathcal{N}$ is defined as a multivariate normal distribution. In the above equation $\langle \boldsymbol{x}' \rangle_{\rm Sgr}$ is taken to be the center of Sagittarius as defined in Section 2.2.2 which is $(0, 0, 0)$ in the prime ($\prime$) frame. Then $\boldsymbol{C}_{\rm proj}$ is the covariance matrix

$$\boldsymbol{C}_{\rm proj} = \boldsymbol{R}_z^T(P.A.) \begin{bmatrix} a^2_{\rm proj} & 0 & 0 \\ 0 & b^2_{\rm proj} & 0 \\ 0 & 0 & 0 \end{bmatrix} \boldsymbol{R}_z(P.A.). \tag{2.21}$$

The covariance matrix is a function of the position angle ($P.A.$) and the projected major axes ($a^2_{\rm proj}, b^2_{\rm proj}$). These projected quantities can be derived from our model parameters as discussed in the previous section via the equations in Section 2.3.1.1.

In order to account for incomplete sampling of the stars in Sagittarius, we must develop a selection function to incorporate into the likelihood analysis. We define a simple selection function $\mathcal{S}_{2D}(x', y') = \int \mathcal{S}_{3D}(\boldsymbol{x}')\,{\rm dz}$ that is equal to 1 inside the region within figure 2.2, and 0 elsewhere. With this selection function, the probability of any set of $\boldsymbol{\Theta}_{3D}$ is then:

$$P(\boldsymbol{\Theta}_{3D}|\mathcal{D}_{2D}) = \frac{\prod_n^N \mathcal{S}_{2D}(\boldsymbol{x'})\ P(\boldsymbol{x'}_n \,|\, \boldsymbol{\Theta}_{3D})[\boldsymbol{\Theta}_{3D}]}{\int\int \mathcal{S}_{2D}(\boldsymbol{x'}) P(\boldsymbol{x'} \,|\, \boldsymbol{\Theta}_{3D})\,{\rm dx'dy'}}. \tag{2.22}$$

where N is the number of stars in the *Gaia* sample and n labels an individual star. With the likelihood defined above, we are able to conduct parameter inference on the 3D model parameters using the methods described below.

Our 3D analysis that uses the OGLE data follows a similar formalism as in the 2D case. We define the true position of a single star as $\tilde{\boldsymbol{x}}'$, and the observed position as $\boldsymbol{x}'$. We assume that the true position of a star given its observed position follows the distribution,

$$P(\boldsymbol{x}' \,|\, \tilde{\boldsymbol{x}}') = \mathcal{N}(\boldsymbol{x}' \,|\, \tilde{\boldsymbol{x}}', \boldsymbol{C}_{\boldsymbol{x}}). \tag{2.23}$$

Here $\boldsymbol{C}_{\boldsymbol{x}}$ is empirically determined by Monte Carlo resampling the distance of an individual star and recomputing its Cartesian position 5000 times, using the assumed errors on the

heliocentric distance of 3% (see Section 2.2) and taking into account the correlations between coordinates.

The population as a whole we model as a multivariate Gaussian with mean given by the centroid of the galaxy ($\langle \boldsymbol{x'} \rangle_{\rm Sgr}$), a dispersion defined by the three principal axes, and an axis of symmetry parameters p and q. The covariance matrix in the inertial frame is then:

$$\boldsymbol{C}_{\rm Sgr} = \begin{bmatrix} a^2 & 0 & 0 \\ 0 & b^2 & 0 \\ 0 & 0 & c^2 \end{bmatrix} = \begin{bmatrix} a^2 & 0 & 0 \\ 0 & (p \times a)^2 & 0 \\ 0 & 0 & (q \times a)^2 \end{bmatrix}. \tag{2.24}$$

Therefore, the probability of a star existing at true location $\tilde{\boldsymbol{x}}'$ is given by:

$$P(\tilde{\boldsymbol{x}}' \,|\, \boldsymbol{\Theta}_{3D}) = \mathcal{N}(\tilde{\boldsymbol{x}}' \mid \langle \boldsymbol{x'} \rangle_{\rm Sgr}, \mathbf{R}^{-1} \boldsymbol{C}_{\rm Sgr} \mathbf{R}). \tag{2.25}$$

Since both the observed (Equation 2.23) and true (Equation 2.25) components are Gaussian we can analytically marginalize the true positions of the stars out. Then the probability of observing a star at position $\boldsymbol{x}$ conditional on our model parameters is

$$\begin{aligned} P(\boldsymbol{x}' \,|\, \boldsymbol{\Theta}_{3D}) =& P(\boldsymbol{x}' \,|\, \tilde{\boldsymbol{x}}')\, P(\tilde{\boldsymbol{x}}' \,|\, \boldsymbol{\Theta}_{3D}) \\ =& \mathcal{N}(\boldsymbol{x}' \mid \langle \boldsymbol{x'} \rangle_{\rm Sgr}, \boldsymbol{C}_{\boldsymbol{x}'_j} + \mathbf{R}^{-1} \boldsymbol{C}_{\rm Sgr} \mathbf{R}). \end{aligned} \tag{2.26}$$

Similar to the 2D case, we then define a selection function as $\mathcal{S}_{3D}(\boldsymbol{x})$. In the 3D case, the selection function is 1 inside the area within the black outline shown in Figure 3 and within a 2 kpc distance from the center of Sagittarius. The full likelihood with the observed selection function is then

$$P(\boldsymbol{\Theta}_{3D} | \mathcal{D}_{3D}) = \frac{\prod_n^N \mathcal{S}_{3D}(\boldsymbol{x}') P(\{\boldsymbol{x}'\}_N \,|\, \boldsymbol{\Theta}_{3D})[\boldsymbol{\Theta}_{3D}]}{\int\int\int \mathcal{S}_{3D}(\boldsymbol{x}') P(\boldsymbol{x}' \,|\, \boldsymbol{\Theta}_{3D}) \mathrm{dx'dy'dz'}}. \tag{2.27}$$

The discussion above is in the context of a separate analysis for both the 2D and the 3D

Parameter	Prior
a(Major axis)	$U(0.1, 10)$ kpc
p (b/a)	$U(0.1, 1)$
q (c/a)	$U(0.1, 1 \times p)$
γ	$U(-90, 90)$ deg
ϕ	$U(-90, 90)$ deg
θ	$U(-90, 90)$ deg

Table 2.1 Assumed priors for our set of baseline model parameters. Parameters are defined in Section 2.3.

likelihoods. We will also consider a joint analysis, in which we fit to the combined 2D and 3D data sets. Assuming that the data sets are independent, which is a reasonable assumption for the *Gaia* and OGLE data, the joint probability for the model parameters given the data is

$$P(\Theta_{3D} \,|\, \mathcal{D}_{2D}, \mathcal{D}_{3D}) = P(\Theta_{3D} \,|\, \mathcal{D}_{2D}) P(\Theta_{3D} \,|\, \mathcal{D}_{3D}). \tag{2.28}$$

For both the separate and the joint likelihood analyses, we determine posterior probabilities for the parameters $\mathbf{\Theta}_{3D}$. To determine these posteriors, we use the nested sampler `PyMultinest` (Buchner et al., 2014; Feroz and Hobson, 2008; Feroz et al., 2009) with 500 live points to generate samples of the posterior. For each parameter the prior used in the fit is listed in table 2.1. Note that for p and q, the lower bound on the prior is 0.1.

2.4 Results

Figure 2.4 shows the posterior probability densities for the principal axes (a, b, c), inclination ($i_{\rm earth}$), Galactic inclination ($i_{\rm Gal}$) and triaxiality (T). The main result from a joint fit to the *Gaia* and OGLE data is shown as a green histogram, and a corner plot of this fit with the six model parameters is shown in Figure 2.6. The median of the cumulative distributions and the 68% containment intervals for each of the parameters are shown in Table 2.2. We generally find that the scale parameters a, p, q are well determined in the joint analysis, with the minor-to-major axis ratio q being the best determined parameter, which is measured

Model Parameters	joint fit	*Gaia* only fit	OGLE only 2d fit	OGLE only 3d fit
a [kpc]	$1.76^{+0.15}_{-0.12}$	$2.01^{+0.33}_{-0.19}$	$1.71^{+1.37}_{-0.37}$	$1.36^{+0.99}_{-0.16}$
p	$0.74^{+0.13}_{-0.1}$	$0.46^{+0.08}_{-0.06}$	$0.74^{+0.23}_{-0.27}$	$0.88^{+0.14}_{-0.36}$
q	$0.43^{+0.05}_{-0.06}$	$0.31^{+0.1}_{-0.14}$	$0.42^{+0.24}_{-0.23}$	$0.64^{+0.2}_{-0.25}$
γ [deg]	$-11.51^{+3.87}_{-3.54}$	$-9.35^{+52.43}_{-40.39}$	$-1.67^{+57.2}_{-54.27}$	$0.35^{+31.49}_{-35.18}$
ϕ [deg]	$-21.24^{+7.83}_{-4.76}$	$2.67^{+64.16}_{-67.75}$	$3.00^{+56.66}_{-58.24}$	$10.67^{+40.45}_{-47.74}$
θ [deg]	$3.15^{+21.51}_{-17.32}$	$-4.62^{+63.82}_{-50.69}$	$-5.28^{+69.18}_{-62.63}$	$114.50^{+37.44}_{-61.38}$
Derived Parameters				
$a_{\rm proj}$ [kpc]	$1.73^{+0.14}_{-0.11}$	$1.88^{+0.16}_{-0.14}$	$1.53^{+0.87}_{-0.25}$	$1.31^{+0.88}_{-0.14}$
$b_{\rm proj}$ [kpc]	$0.86^{+0.03}_{-0.03}$	$0.86^{+0.03}_{-0.03}$	$1.15^{+0.22}_{-0.29}$	$1.07^{+0.16}_{-0.25}$
P.A. [deg]	$102.19^{+2.44}_{-2.46}$	$101.90^{+2.14}_{-2.1}$	$98.49^{+63.95}_{-76.19}$	$109.91^{+58.2}_{-91.92}$
T	$0.56^{+0.18}_{-0.26}$	$0.87^{+0.08}_{-0.1}$	$0.61^{+0.31}_{-0.49}$	$0.47^{+0.48}_{-0.57}$
$r_{1/2}$ [kpc]	$2.74^{+0.23}_{-0.18}$	$3.14^{+0.51}_{-0.3}$	$2.67^{+2.14}_{-0.58}$	$2.12^{+1.55}_{-0.26}$
$r_{1/2,\,\rm proj}$ [kpc]	$2.04^{+0.16}_{-0.13}$	$2.22^{+0.18}_{-0.16}$	$1.80^{+1.03}_{-0.29}$	$1.55^{+1.04}_{-0.16}$

Table 2.2 Results of our fits for the joint case as well as the *Gaia* only, OGLE only 2d (α, δ) and OGLE only 3d (α, δ, $D_\odot$) cases. The values are the median for each parameter, and the errors show the 68% confidence interval. Histograms showing the posteriors for a selection of these parameters is shown in Figure 2.4. For the joint fit the $r_{1/2,\,\rm proj} = 2.04\,$kpc corresponds to an on sky major axis of $269 \pm 21'$.

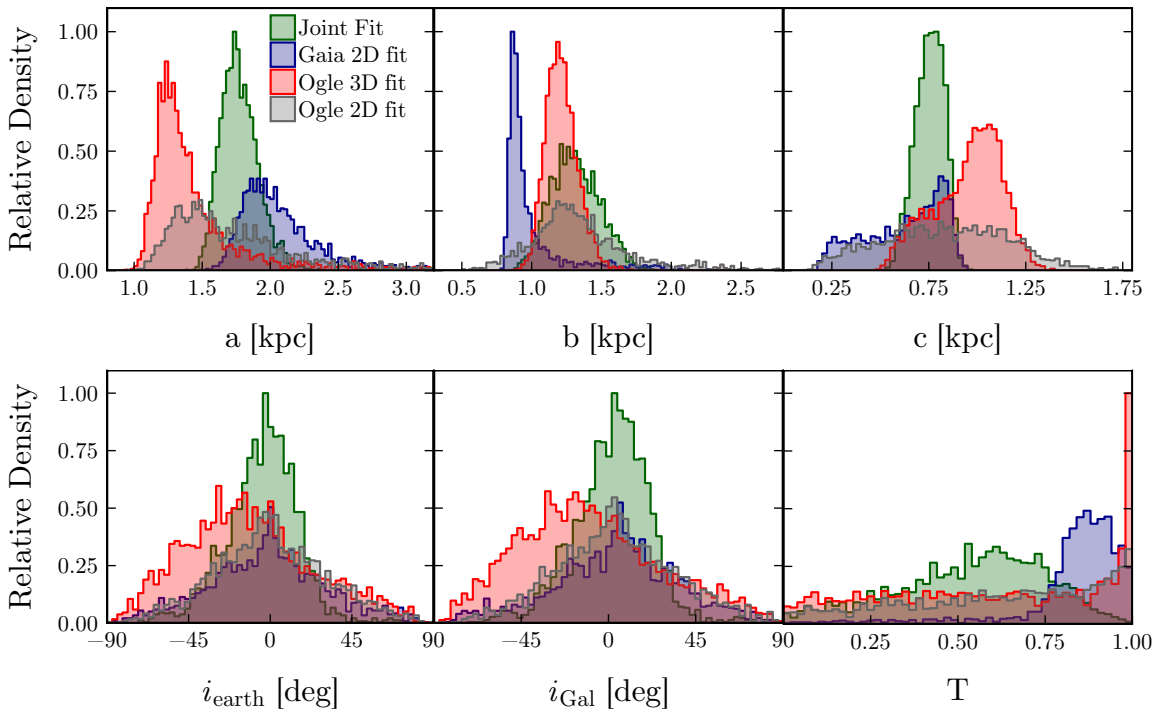

Figure 2.4 Posterior probability densities resulting from the likelihood analysis. The top row shows the results for the principal axes (a, b, c) of the core of Sagittarius, and the bottom row shows the posteriors for the inclination with respect to earth ($i_{\rm earth}$) and with respect to the Galactic center ($i_{\rm Gal}$ as well as the Triaxiality (T) of the system. To illustrate how each of the datasets effects our results posteriors are shown for the individual fits of the *Gaia* (*blue*) and OGLE data (*red*), a fit of only the 2D information from the OGLE data (*grey*), and the joint fit of the two datasets (*green*).

to $\lesssim 20\%$. The corresponding angles are generally less well constrained, in particular the rotation angle θ is not well determined by our analysis.

To get a sense of which data set is providing more statistical constraining power, Table 2.2 shows results from the individual fits to each of the *Gaia* data, the full 3D OGLE data, and only the 2D OGLE data. The medians of the scale lengths from the individual fits are found to differ; in particular the *Gaia* data favors a major axis radius ~ 2.01 kpc, while the 3D OGLE data favors a lower value, ~ 1.36 kpc. However the results are consistent when considering the 68% containment intervals. Figure 2.4 shows a comparison of the full posterior distributions of the major axis scale length as determined for both the joint and separate analyses. From this figure we see that the major axis scale length determined from the *Gaia* data is more aligned with the results from the joint fit. This is because the *Gaia* data is more extended, and thereby providing more constraining power than the OGLE data on the scale length.

In Table 2.2 we also show measurements of parameters derived from our baseline set of parameters. The 3D half-light radii along the major axis is $r_{1/2} = 1.17^{+0.07}_{-0.06}$ kpc, and the 2D half-light radii along the major axis is $r_{1/2,proj} = 1.14^{+0.07}_{-0.06}$ kpc. Note that our fits are different than the half-light radius obtained from the red giant fits with 2MASS data (Majewski et al., 2003b). The projected major axis of our fit is found to have a half light radius of $269 \pm 21'$ compared to their value of $342 \pm 12'$, and the projected ellipticity from our fit is $\epsilon = 0.49 \pm 0.04$, which can be compared to their result of $\epsilon = 0.62 \pm 0.02$. We do find consistent results for the position angle (*P.A.*).

From the parameters p and q, we derive the posterior probability distribution of T. We find $T = 0.56^{+0.18}_{-0.26}$, where again the uncertainties are 68% containment confidence intervals. Interestingly, a prolate spheroid corresponding to $T = 1$ is ruled out by the model, while an oblate spheroid is strongly disfavored at the $\sim 95\%$ confidence level.

From the posterior probabilities we also deduce both the inclination of the major axis with respect to the plane of the sky, and the projection of the major axis on the direction

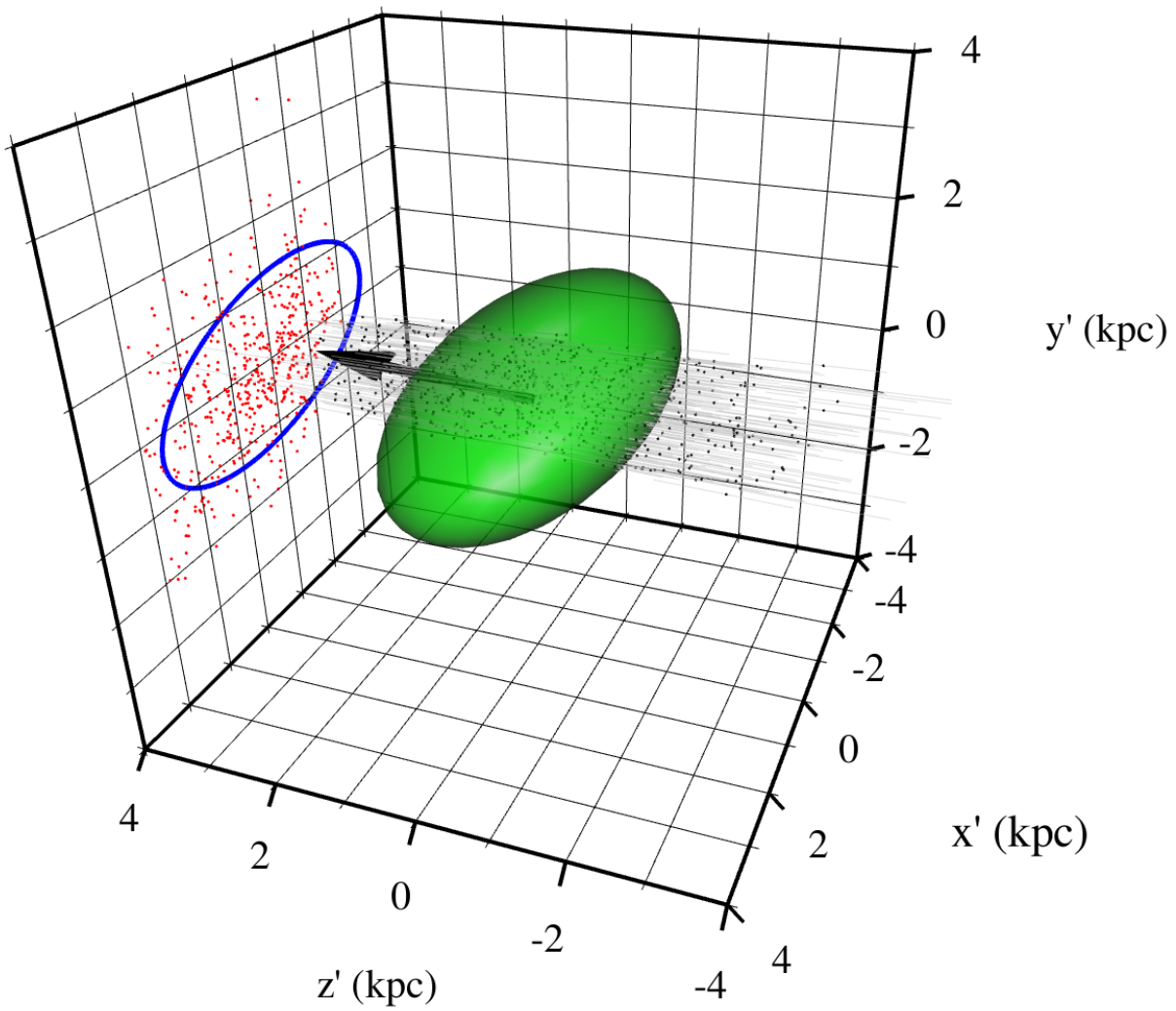

Figure 2.5 Three dimensional plot showing the results of our analysis. The red points show the two dimensional location of *Gaia* RR Lyrae, and the blue ellipse indicates the half light radius derived from them. The black points show OGLE RR Lyrae where the grey lines indicate the uncertainty on the position of each star. The green ellipsoid shows the three dimensional half light radius of Sagittarius derived from the results of our analysis. The $\hat{z}'$ axis points towards the observer. The black arrow points towards the Galactic center.

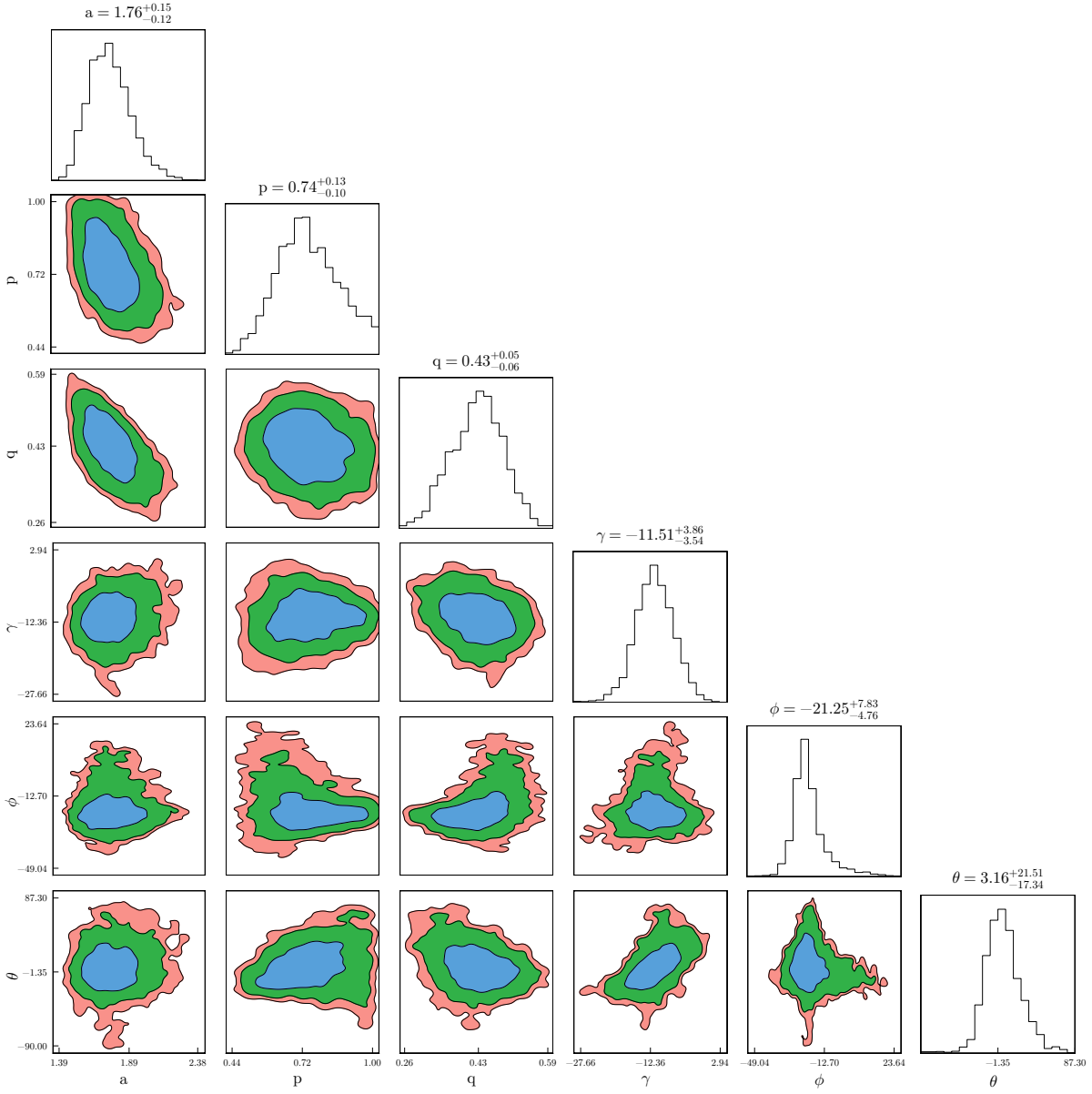

Figure 2.6 Posterior probability densities from a joint fit to the *Gaia* and OGLE data for the six baseline parameters of our model; a is the major axis scale length in kpc, p is the ratio of the intermediate to the major axis, and q is the ratio of the minor to the major axis. The angles are the Euler rotation angles as defined in Section 2.3 in units of degrees.

towards the Galactic center. The inclination relative to the observer is $i_{earth} = -4.9^{+17.5}_{-18.8}$ deg, and the inclination relative to the Galactic center is $i_{Gal} = 1.6^{+17.5}_{-18.9}$ deg. Note again that an inclination of zero implies that the major axis is fully within the plane of the sky relative to the observer. These two values of the inclination are very similar due to the location of Sagittarius relative to the Galactic center. We note that the major axis is not aligned with the direction of the Galactic center, which may have important implications when comparing to general theoretical predictions for dwarf galaxies, which we discuss in more detail below.

Figure 2.5 shows a three-dimensional view of the system. The red points are *Gaia* RR Lyrae projected onto to the z=0 plane, and the blue ellipse is the projected half light ellipse. The black points show the 3D distribution of OGLE RR Lyrae in Sagittarius-centered Cartesian coordinates ($\boldsymbol{x}'$), and the grey lines show the uncertainty on position for each OGLE star. The green ellipsoid marks the three dimensional half light radius as inferred by our analysis; its orientation and triaxiality can be seen. As a reminder the $\hat{z'}$ axis points towards the observer.

As a consistency check we take our posterior distribution of parameters Θ_{3D} and generate mock observed RR Lyrae distributions. This is done by sampling Θ_{3D} values randomly from the equal weighted posteriors (histograms in figure 2.6), generating data following our model distribution, and applying the observational selection function. These mock catalogs should have similar spatial distributions as our observed data. The results of repeating this process for 1000 mock data sets are shown in Figure 2.7, where in the top row the red line shows the observed distribution of OGLE RR Lyrae in Cartesian coordinates as well as the radial distribution of these stars stars. In the bottom row the green line shows the observed distribution of *Gaia* RR Lyrae in both right ascension (α) and declination (δ). For all of these plots the black line marks the median distribution of our mock catalogs over the same coordinates, and the blue shading indicates 50% and 95% confidence intervals for these mock catalogs. We find that there is generally good agreement between the observed distribution and the expected distribution based on the results of our analysis.

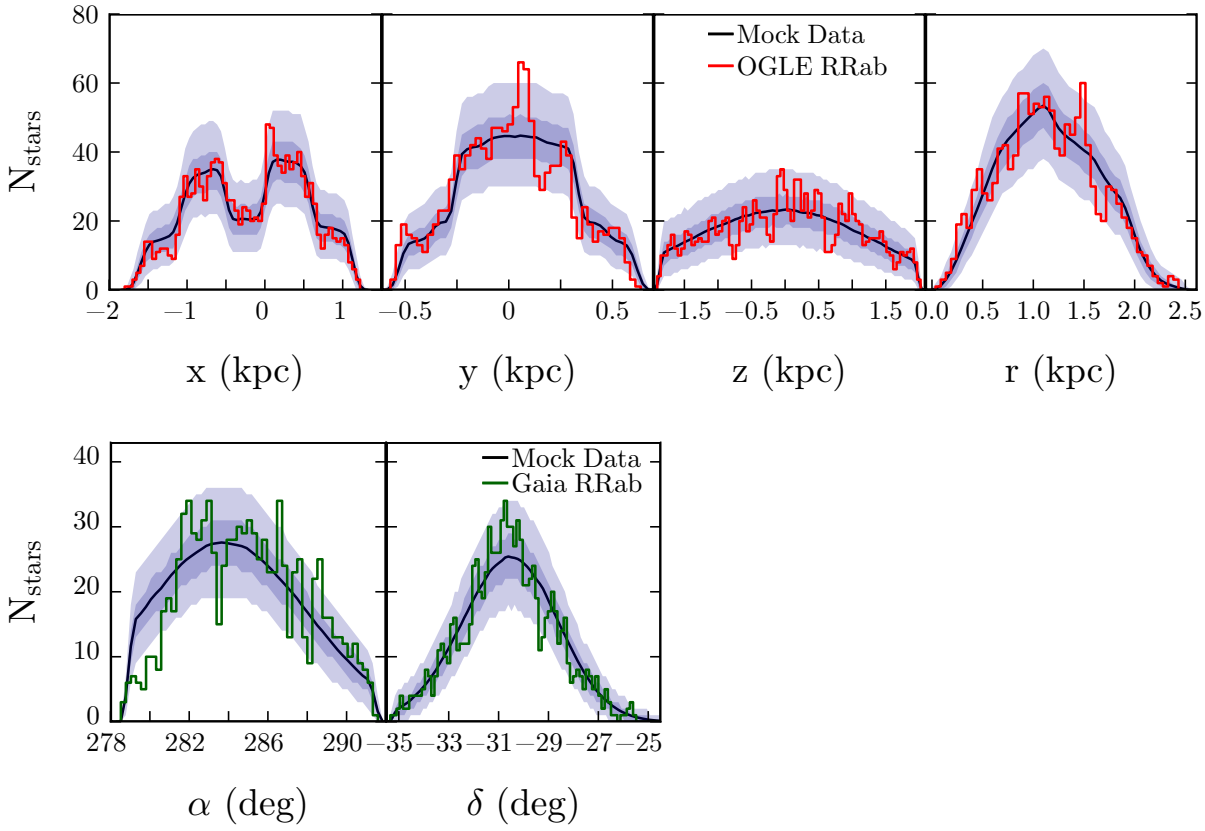

Figure 2.7 Histograms showing the distribution of OGLE RR Lyrae in different dimensions. For each panel the red (green) line shows the observed distribution of OGLE (*Gaia*) stars, the black line is the median of 1000 mock realizations drawn from the posteriors of our model, and the blue contours show 50% and 95% confidence intervals for the mock realizations. *Top row:* the panels show comparisons in x', y', z', and the radial distribution between the observed 3D positions of OGLE RR Lyrae and the model. *Bottom row:* the panels compare the observed on sky (α, δ) positions of *Gaia* RR Lyrae and the model.

2.5 Discussion and Conclusion

We have performed the first 3D modeling of the spatial distribution of stars in the core of the Sagittarius dSph. Our sample of stars comes from both *Gaia* DR2 data and from the OGLE-IV RR Lyrae catalog. We derive distances to the OGLE stars, and from these and the *Gaia* data we find that the spatial distribution is a triaxial ellipsoid. The more simple case of a prolate spheroid is ruled out at high statistical significance. These results come from a combined analysis of the *Gaia* and OGLE data– such strong results are not attainable from an individual dataset.

Our results may be compared to previous estimates of the three-dimensional structure of Sagittarius. Ibata et al. (1997) use red clump stars and find that the core is consistent with a prolate spheroid. The OGLE collaboration (Hamanowicz et al., 2016) used their RR Lyrae catalog (Soszyński et al., 2014) to measure FWHM along the line-of-sight and find the size in this dimension to be 2.42 kpc.

We have obtained the first measurement of the orientation of the stellar distribution of Sagittarius with respect to the plane of the sky and with respect to the Galactocentric frame of reference. The major axis of the RR Lyrae distribution is aligned nearly parallel to the sky plane, and the major axis is nearly perpendicular to the direction of the Galactic center.

It is interesting to compare this result to the predictions of cosmological simulations (Kuhlen et al., 2007; Barber et al., 2015). These generally find that the major axis of the dark matter distribution of subhalos is aligned with the Galactic center. This alignment is found to be stronger for systems that are closer to the Galactic center and for those that have been heavily tidally disrupted, i.e. systems like Sagittarius. These results from simulations however only apply to the dark matter distribution. It will be important in the future to develop predictions for the orientation of the dark matter distribution relative to the stellar distribution, and compare to the results we have obtained for Sagittarius.

It is also interesting to compare our results to theoretical models for the Sagittarius progenitor. For example the elongated shape may be produced in models where the progenitor

was a disk galaxy, and the system is currently at its second pericenter passage, transforming from a disk galaxy to a more spheroidal structure resembling a dwarf spheroidal (Łokas et al., 2010).

Since our RR Lyrae sample is mostly contained within the half-light radius of the Sagittarius core, the sample may be used to probe the dynamical mass distribution in the remnant core of the system that remains bound and in dynamical equilibrium. Three-dimensional positions combined with line-of-sight velocities of stars are expected to improve measurements of the velocity anisotropy parameter (Richardson et al., 2014). Targeted radial velocity measurements, along with future improvements in *Gaia* proper motions, would provide the first full six-dimensional phase space coverage of stars in a dwarf spheroidal, allowing for an unprecedented analysis of the dynamical state of the dark and luminous mass in the galaxy.

Facilities: OGLE, *Gaia*.

Software: `astropy` (Astropy Collaboration et al., 2013; Price-Whelan et al., 2018), `Matplotlib` (Hunter, 2007), `numpy` (Van Der Walt et al., 2011), `pandas` (pandas development team, 2020; Wes McKinney, 2010), `scipy` (Jones et al., 2001), `PyMultinest`, `Multinest` (Buchner et al., 2014; Feroz and Hobson, 2008; Feroz et al., 2009), `ggplot2` (Wickham, 2016).

3. DELVE-ING INTO THE JET: A THIN STREAM ON A RETROGRADE ORBIT AT 30 KPC

3.1 Introduction

Stellar streams form through the tidal disruption of dwarf galaxies and globular clusters as they accrete onto a larger host galaxy (e.g., Newberg and Carlin, 2016). The formation of stellar streams is an expected feature of hierarchical models of galaxy formation where large galaxies grow through mergers of smaller systems (Lynden-Bell and Lynden-Bell, 1995; Johnston et al., 2001). Due to their formation mechanism, transient nature, and dynamical fragility, stellar streams provide a direct and powerful probe of the gravitational field in galactic halos at both large and small scales (e.g., Johnston et al., 1999, 2002; Ibata et al., 2002). Within our Milky Way in particular, stellar streams have been proposed as sensitive probes of the large- and small-scale distributions of baryonic and dark matter within the Galactic halo (Johnston et al., 2001; Carlberg, 2013; Erkal et al., 2016; Bonaca and Hogg, 2018; Banik et al., 2019).

Milky Way stellar streams form when stars are unbound from the progenitor at the Lagrange points between the progenitor stellar system and the Milky Way. Stars that are unbound from the inner Lagrange point have lower energy and thus shorter orbital periods than the progenitor whereas those at the outer Lagrange point have higher energy and shorter orbital periods. Thus, as the progenitor is disrupted, leading and trailing streams of stars will form roughly tracing the orbit of the progenitor within the Milky Way potential (Sanders and Binney, 2013). The width of a stellar stream is proportional to the velocity dispersion of its progenitor (Johnston et al., 2001; Erkal et al., 2019), implying that stellar streams formed through the disruption of globular clusters are narrow ($\sim 100\,\mathrm{pc}$) and dynamically cold, while streams originating from dwarf galaxies are broader ($> 500\,\mathrm{pc}$) and dynamically hot. The population of cold stellar streams with small internal velocity dispersions provides

a sensitive probe of the gravitational field far from the Milky Way disk.

In a smooth gravitational potential, stellar streams form as coherent structures spanning tens of degrees on the sky (e.g., Newberg and Carlin, 2016). Long stellar streams can be used to trace the local gravitational field over tens of kpc (Bovy, 2014). In conjunction with orbit modeling and simulations, streams can constrain the total mass enclosed inside their orbits (e.g., Gibbons et al., 2014; Bowden et al., 2015; Bovy et al., 2016; Bonaca and Hogg, 2018), and the shapes and radial profiles of the gravitational field (e.g., Law and Majewski, 2010b; Koposov et al., 2010). Bonaca and Hogg (2018) find that a dozen cold stellar streams with full 6D kinematic measurements should contain enough information to constrain the mass and shape of a simple Milky Way potential with $\sim 1\%$ precision. Additionally, perturbations from large structures can induce a misalignment between the orbit and track of a stream, which can be used to constrain the mass of the perturbing object (Erkal et al., 2018; Shipp et al., 2019). For example, Erkal et al. (2019) and Vasiliev et al. (2021) used the Orphan and Sagittarius streams, respectively, to simultaneously measure the mass of the Milky Way and Large Magellanic Cloud (LMC).

Stellar streams can also probe the clustering and distribution of dark matter at small scales. The dark energy plus cold dark matter (ΛCDM) model predicts that dark matter should clump into gravitationally bound halos on scales that are much smaller than the smallest galaxies (Green et al., 2004; Diemand et al., 2005; Wang et al., 2020). Dark matter subhalos that pass close to stellar streams may gravitationally perturb the stream by altering the stream track and inducing small-scale density fluctuations. Discrete gaps in stellar streams, such as those found in the Pal 5 and GD-1 streams discovered from data collected by the Sloan Digital Sky Survey (Odenkirchen et al., 2001; Grillmair and Dionatos, 2006), can probe the population of compact subhalos with $10^6\,\mathrm{M}_\odot < M < 10^8\,\mathrm{M}_\odot$ that contain no luminous matter (e.g., Erkal et al., 2016; Bonaca et al., 2019). Additionally, the power spectrum of density fluctuations along a cold stream can place limits on the number of dark subhalos (e.g., Banik et al., 2019) and the mass of warm dark matter candidates (e.g., sterile

neutrinos; Dodelson and Widrow, 1994; Shi and Fuller, 1999). However, baryonic structures such as giant molecular clouds (Amorisco et al., 2016) or Milky Way substructure such as the disk and bar (Erkal et al., 2017; Pearson et al., 2017; Banik et al., 2019) can induce perturbations that mimic the observational signature of dark matter subhalos. It is thus crucial to characterize cold streams at large Galactocentric radii where they are less likely to be affected by baryonic structures (e.g., Li et al., 2020).

Despite the importance of Milky Way stellar streams as probes of galaxy formation in a cosmological context, they remain difficult to detect due to their low surface brightness (fainter than 28.5 mag/arcsec^2) and large extent on the sky ($\gtrsim 10^\circ$). The phase space signature of streams at large Galactocentric distances is often difficult to detect from space-based observatories (e.g., *Gaia*). Stars in these streams are either too faint to have well-measured proper motions or their proper motions overlap with the locus of faint foreground stars at small distances (Ibata et al., 2020). Distant streams have only recently been detected thanks to deep, wide-area imaging by ground-based digital sky surveys (e.g. SDSS, Pan-STARRS1, and DES, Belokurov et al., 2006; Chambers et al., 2016; Shipp et al., 2018).

The Jet stream is one such dynamically cold stellar stream that was discovered by Jethwa et al. (2018) (hereafter referred to as J18) in the Search for the Leading Arm of Magellanic Satellites (SLAMS) survey. This stream was found to have a width of 0.18° and a length of 11° (truncated on one end by the survey footprint). They found the stellar population of Jet to be well-described by an old (12.1 Gyr), metal-poor ([Fe/H] $=-1.57$) isochrone. Fits to the main sequence turn-off (MSTO) and the distribution of blue horizontal branch (BHB) stars in the central portion of the stream place its heliocentric distance at $\sim$29 kpc. At this distance the physical width of the stream corresponds to $\sim$ 90 pc, placing the stream firmly in the dynamically cold category. This narrow width also suggests the progenitor of Jet was likely a globular cluster, although no progenitor was found by J18.

We further investigate the Jet stream using data from the DECam Local Volume Exploration Survey (DELVE) Data Release 1 (DR1) (Drlica-Wagner et al., 2021). This catalog

covers over $\sim$ 4,000 deg^2 in four photometric bands (g, r, i, z) and over $\sim$ 5,000 deg^2 in each band independently. The sensitivity of DELVE has been demonstrated by the discovery of a Milky Way satellite galaxy candidate with $M_V = -5.5$ at a distance of $\sim 116\,\mathrm{kpc}$ (Centaurus I; Mau et al., 2020) and two faint star cluster candidates (DELVE 1, DELVE 2; Mau et al., 2020; Cerny et al., 2021). DELVE DR1 contiguously and homogeneously covers a large region including and extending the SLAMS survey footprint. Thus, the DELVE data are ideal to further characterize the Jet stream.

To dynamically model the stream and extract local properties of the gravitational field, additional phase space information is needed. With full 3D kinematic information, the Jet stream can become an even better tool for measuring the properties of the Milky Way, and even more can be learned about its interaction history. A combination of proper motion and radial velocity measurements are required to obtain the full 6D phase space information of the Jet stream. The high-precision astrometric survey *Gaia* has revolutionized this field and allowed for measurements of the proper motion of faint stream stars for the first time. The early third data release from *Gaia* (*Gaia* EDR3; Gaia Collaboration et al., 2016a, 2020) provides proper motion measurements for more than 1.4 billion stars down to a magnitude of $G \sim 21$. *Gaia* has previously been used to characterize the proper motions of many stellar streams (e.g. Shipp et al., 2019; Price-Whelan and Bonaca, 2018; Koposov et al., 2019) and discover tens of candidate stellar streams (e.g. Malhan and Ibata, 2018; Malhan et al., 2018; Ibata et al., 2020). In this paper we use astrometric measurements from *Gaia* and photometry from DELVE to measure the proper motion of the Jet stream for the first time and quantitatively characterize its shape. These measurements, along with future spectroscopic observations, will allow for a full characterization and dynamical modeling of this stream.

This paper is organized as follows. In Section 3.2 we briefly present the DELVE DR1 dataset. We then describe our analysis of the Jet stream in Section 3.3, initially using the DELVE DR1 dataset to characterize the stream track over an extended region of the sky.

Next, we measure a distance gradient along the stream using blue horizontal branch stars, and use this distance gradient to optimize our matched-filter. Then, we model the observations to quantitatively characterize the structure of the stream. To further characterize the stream, we use the DELVE DR1 photometry along with proper motion measurements from *Gaia* EDR3 to measure the proper motion of the Jet stream for the first time. In Section 3.4 we fit the stream with a dynamical model to determine the best-fit orbital parameters and to determine whether the stream is likely to have been significantly perturbed by large substructure such as the Milky Way bar or presence of the LMC. We discuss our results in Section 3.5 and conclude in Section 3.6.

3.2 DELVE DR1 Data

DELVE seeks to provide contiguous and homogeneous coverage of the high-Galactic-latitude ($|b| > 10^\circ$) southern sky ($\delta < 0^\circ$) in the g, r, i, z bands (Drlica-Wagner et al., 2021). This is done by assembling all existing archival DECam data and specifically observing regions of the sky that have not been previously observed by other community programs. These data are consistently processed with the same data management pipeline to create a uniform dataset (Morganson et al., 2018). The DELVE DR1 footprint consists of the region bounded by $\delta < 0^\circ$ and $b > 10^\circ$ with an additional extension to $b = 0^\circ$ in the region of $120^\circ < \alpha < 140^\circ$ to search for extensions of the Jet stream. This footprint is shown in Figure 3.1 as a light blue shading. Additionally, we searched the Jet Bridge region below the Galactic plane (light orange shading). However, no evidence of a continuation of the Jet stream was found in this region.

The DELVE DR1 dataset consists of ∼30,000 DECam exposures, with exposure times between $30\,\mathrm{s} < \mathrm{t_{exp}} < 350\,\mathrm{s}$. Additionally, the following quality cuts were applied to individual exposures: a minimum cut on the effective exposure time scale factor $\mathrm{t_{eff}} > 0.3$ (Neilsen et al., 2015) and a good astrometric solution relative to *Gaia* DR2 (For each exposure > 250 astrometric matches, $\chi^2_{\mathrm{astrom}} < 500$, where a match has $\Delta(\alpha) < 150\,\mathrm{mas}$, and $\Delta(\delta) < 150\,\mathrm{mas}$). All exposures were processed with the DES Data Management (DESDM)

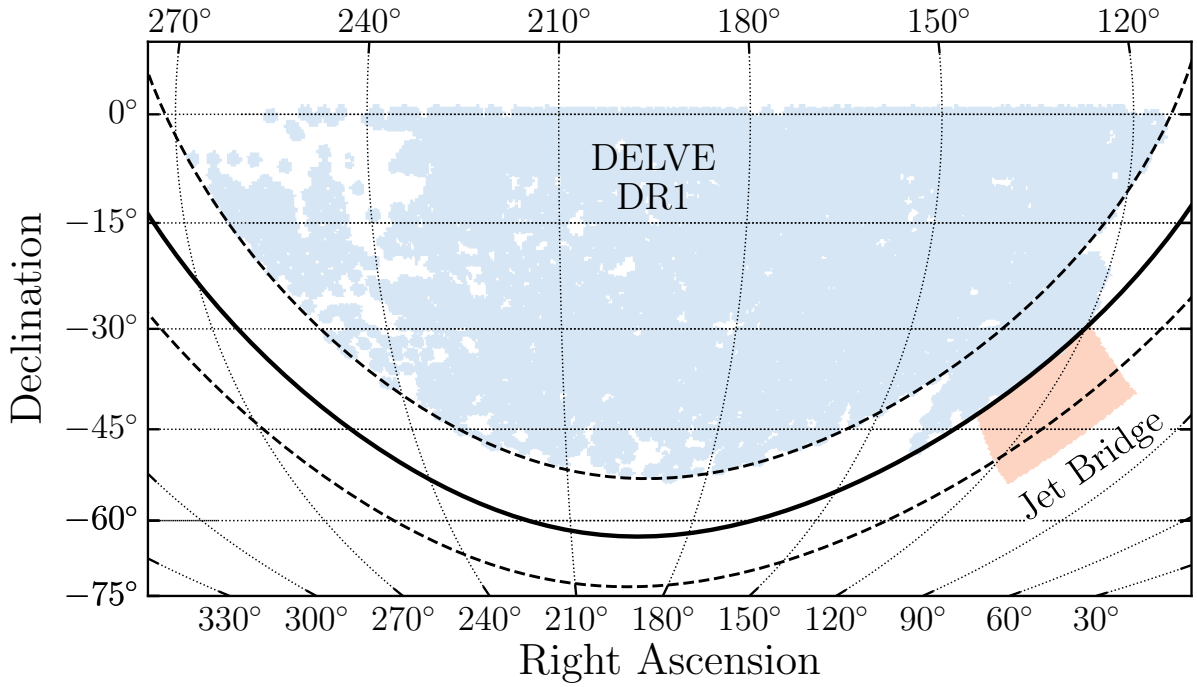

Figure 3.1 The DELVE DR1 region where our search was performed is shown in light blue. The additional region (the Jet Bridge) that was searched is shown as a light orange patch. The solid black line indicates the plane of the Milky Way ($b = 0$ °) and the two dashed lines indicate $b = \pm 10°$.

pipeline (Morganson et al., 2018), enabling sub-percent-level photometric accuracy by calibrating based on seasonally averaged bias and flat images and performing full-exposure sky background subtraction (Bernstein et al., 2018). Automatic source detection and photometric measurement is performed on each exposure using `SExtractor` and `PSFex` (Bertin and Arnouts, 1996; Bertin, 2011). Astrometric calibration was performed against *Gaia* DR2 using `SCAMP` (Bertin, 2006). Photometric zeropoints for each CCD were derived by performing a 1 arcsec match between the DELVE `SExtractor` catalogs and the ATLAS Refcat2 catalog (Tonry et al., 2018), and using transformation equations derived by comparing stars in ATLAS Refcat2 to calibrated stars from DES DR1 to convert the ATLAS Refcat2 measurements into the DECam *griz*-bandpass (Drlica-Wagner et al., 2021). The zeropoints derived

from this processing were found to agree with the DES DR1 zeropoints with a scatter of $\lesssim 0.01$ mag. Dust extinction corrections were applied using extinction maps from Schlegel et al. (1998) assuming $R_V = 3.1$ and a set of R_λ coefficients derived by DES (DES Collaboration et al., 2018) including a normalization adjustment from Schlafly and Finkbeiner (2011). Hereafter, all quoted magnitudes have been corrected for interstellar extinction. For more details on the catalog creation and validation see Drlica-Wagner et al. (2021).

A high-quality stellar sample is selected based on the `SExtractor` quantity `SPREAD_MODEL` (Desai et al., 2012) measured in the DELVE g-band. Specifically, we select objects with $|$`SPREAD_MODEL_G`$| < 0.003$. The performance of this classifier was evaluated by matching sources in the DELVE DR1 catalog with the W04 HSC-SSP PDR2 catalog (Aihara et al., 2019). For our analysis we choose a limiting magnitude of $g = 23.1$ mag where the stellar completeness drops to $\sim 60\%$ and contamination rapidly rises to $\sim 40\%$ as estimated from the HSC catalog. For more information on morphological classification in this catalog see Drlica-Wagner et al. (2021). A bright-end limit of 16th magnitude in the g-band is chosen to avoid saturation effects from bright stars. Additionally, since we are primarily interested in Main Sequence (MS) and Red Giant Branch (RGB) stars associated with old, metal-poor populations, we restrict the color range of our dataset to be $0.0 < (g - r)_0 < 1.0$. Only objects passing the above morphological, magnitude, and color cuts are used in the following matched-filter analysis.

To account for missing survey coverage over our footprint, we quantify the sky area covered by DELVE DR1 in the form of `HEALPix` maps. These maps account for missing survey coverage, gaps associated with saturated stars and other instrumental signatures. They are created using the `healsparse`[1] tool developed for the Legacy Survey of Space and Time (LSST) at the Vera C. Rubin Observatory, and its DECam implementation `decasu`[2] to pixelize the geometry of each DECam CCD exposure. The coverage is calculated at a high resolution (`nside` =16384; $\sim 0.01\,\mathrm{arcmin}^2$) and degraded to give a fraction of the lower

[1] `https://github.com/LSSTDESC/healsparse`
[2] `https://github.com/erykoff/decasu`

resolution pixel area that is covered by the survey.

3.2.1 *Gaia* cross-match with DELVE DR1

To enable a characterization of the proper motion of the Jet stream, we use the *Gaia* EDR3 dataset (Gaia Collaboration et al., 2020). We begin by performing an angular cross match between the *Gaia* EDR3 dataset and DELVE DR1 with a matching radius of $0''5$. This results in a catalog containing ~ 143 million sources. Subsequently, a number of quality cuts are applied. Nearby sources are removed by applying a parallax cut similar to Pace and Li (2019) of $\varpi - 3\sigma_{\varpi} < 0.05$. To remove sources with bad astrometric solutions we place a cut on the renormalized unit weight error (`ruwe`) of `ruwe` < 1.4. Then, a cut on BP and RP excess is applied following equation 6 of Riello et al. (2020) ($|C^{\star}| < 3\sigma_{C^{\star}}$). Additionally, only sources with `astrom_chi2_al` < 2 are kept to avoid sources with bad astrometric fits in *Gaia*. We check that no known Active Galactic Nuclei (AGN) are in our sample by removing all sources that appear in the *Gaia* table `gaiaedr3.agn_cross_id`. Finally, we remove faint sources with $G > 20$ mag to avoid contamination from stars with low signal-to-noise proper motion measurements. The resulting catalog is used for the analyses described in Sections 3.3.2 and 3.3.5.

3.3 Methods and Analysis

In this section we describe our procedure to fit the track, distance gradient, proper motion, and morphology of the Jet stream. We begin by performing an initial matched-filter selection for the Jet stream assuming the best-fit isochrone parameters and distance modulus from J18 (Section 3.3.1). This allows us to determine an initial estimate for the Jet stream track. We then select candidate BHB stars that lie along the track and are clustered in proper motion space to determine a distance gradient as a function of angular distance along the stream (Section 3.3.2). Then we create a new optimized matched-filter map of the Jet stream using the distance gradient of the candidate BHB stars, and refitting an isochrone to a Hess difference diagram (Section 3.3.3). This map is fit with a spline-based generative model

to quantitatively characterize the track, intensity and width of the stream as a function of angular distance along the stream (Section 3.3.4). Finally, we select RGB and BHB stars consistent with being members of the Jet stream and fit a two component Gaussian mixture model to the selected stars determining the proper motion for the Jet stream including a linear gradient term (Section 3.3.5).

3.3.1 Initial matched-filter Search

To investigate the Jet stream in DELVE DR1, we began by applying a matched-filter algorithm in color–magnitude space similar to Shipp et al. (2018, 2020). The matched-filter is derived from a Dotter et al. (2008) synthetic isochrone as implemented in `ugali` (Drlica-Wagner et al., 2020).[3] Candidate MS stars are selected within a range of colors around the isochrone (Equation 4 in Shipp et al. 2018) taking into account photometric uncertainty. To select stars consistent with the Jet stream, we create a matched-filter based on the best-fit parameters (including distance modulus) taken from J18: an age of 12.1 Gyr, a metallicity of [Fe/H] $=-1.57$, and a distance modulus of $m - M = 17.28\,\mathrm{mag}$.

Our selection is conducted using the DELVE DR1 catalog described in Section 3.2. Stars are selected using the matched-filter and then objects are pixelized into `HEALPix` pixels with `nside` $= 512$ (pixel area of $\sim 0.01\,\mathrm{deg}^2$). The pixelized filtered map is corrected by the survey coverage fraction for each pixel to account for survey incompleteness, and pixels with a coverage fraction less than 0.5 are removed from the analysis. Figure 3.2 shows the results of this matched-filter selection. The Jet stream can be clearly seen to extend beyond the initial discovery bounds (marked by orange circles) in both directions. At high declination the stream becomes fainter and more diffuse and appears to fan out, and at lower declination an additional prominent component can be seen with obvious density variations.

In absence of an obvious stream progenitor, we choose the stream-centered coordinate frame to be the same as J18 defined by pole $(\alpha_{pole}, \delta_{pole}) = 64.983°, 34.747°$ and a ϕ_1 center of $\phi_1 = 63°$ ($\phi_1, \phi_2 = 0°, 0°$ at $\alpha, \delta = 138.62°, 22.10°$). We define the rotation matrix to

[3] `https://github.com/DarkEnergySurvey/ugali`

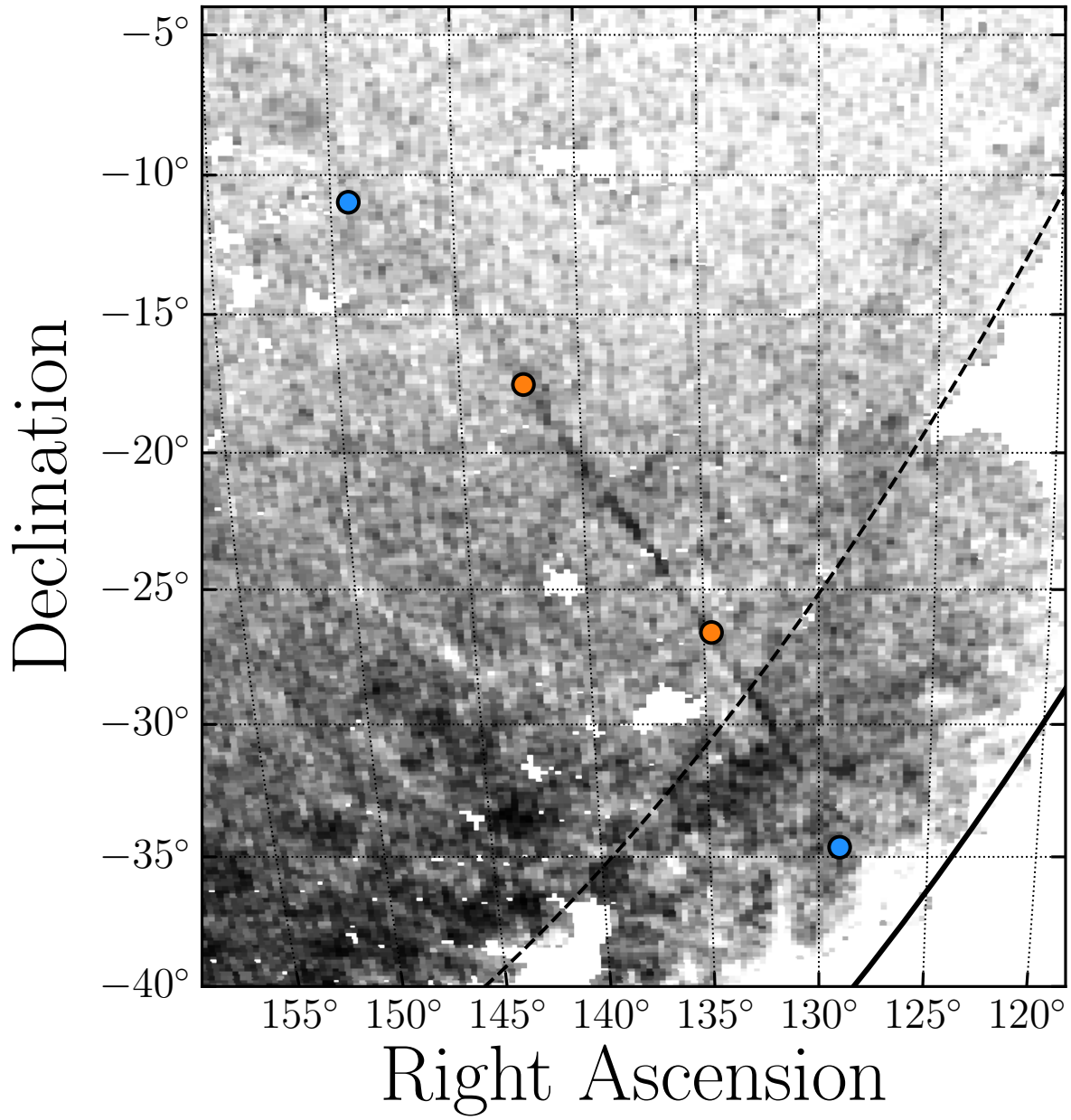

Figure 3.2 A stellar density map from the DELVE photometry showing the Jet stream at a distance modulus of $m - M = 17.28$ ($D_\odot = 28.6\,\mathrm{kpc}$). The orange points show the extent of the stream identified by Jethwa et al. (2018), and the blue points denote the new extent of the stream as detected in MSTO and BHB stars as determined in this study. The solid black line in the bottom right indicates the plane of the Milky Way ($b = 0°$), and the dashed line shows $b = 10°$.

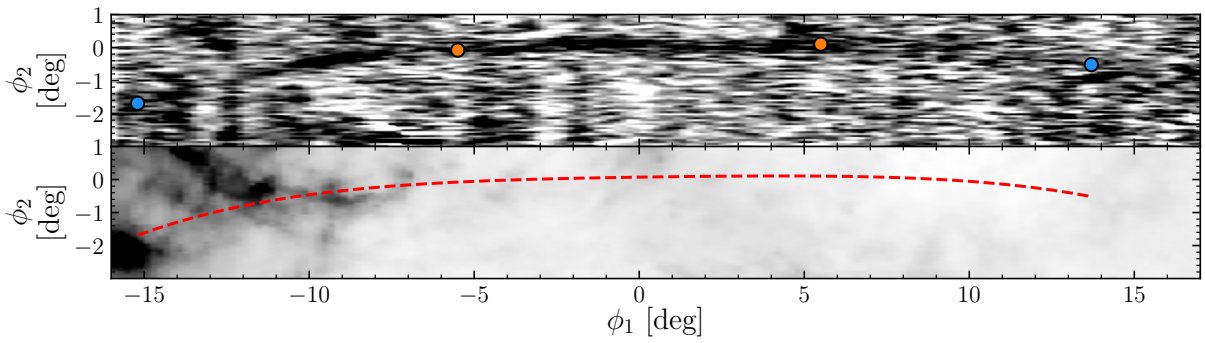

Figure 3.3 *Top:* Jet stream density after applying the same matched-filter as Figure 3.2. Additionally, deviations from great circle path $\phi_2 = 0°$ are clearly seen. The orange points show the extent of the stream identified by Jethwa et al. (2018), and the blue points denote the new extent of the stream as detected in MSTO and BHB stars. For the range $\phi_1 < -12.7°$ or $> 10°$ the stream is only detected using BHB stars. *Bottom:* SFD dust map of the same region. The red dashed line shows the track of Jet.

convert α, δ to ϕ_1, ϕ_2 to be:

$$\boldsymbol{R} = \begin{bmatrix} -0.69798645 & 0.61127501 & -0.37303856 \\ -0.62615889 & -0.26819784 & 0.73211677 \\ 0.34747655 & 0.74458900 & 0.56995374 \end{bmatrix}. \tag{3.1}$$

The top panel of Figure 3.3 shows the transformed matched-filter stellar density map. This map has been smoothed by a Gaussian kernel with a size of $\sigma = 0.06°$, and each column has been normalized to have the same median to correct for variable background stellar density along the field. The track of the stream clearly deviates from the great circle path defined by $\phi_2 = 0°$. We fit a fourth-order polynomial to the peak intensity of the stream at each ϕ_1 for the range $-14° < \phi_1 < 14°$ giving the following relation for ϕ_2 as a function of ϕ_1:

$$\begin{aligned} \phi_2(\phi_1) =& 0.07247 + 0.01475 \times (\phi_1) - 0.00138 \times (\phi_1)^2 \\ &+ 0.00006 \times (\phi_1)^3 - 0.00002 \times (\phi_1)^4. \end{aligned} \tag{3.2}$$

The bottom panel of Figure 3.3 show the Schlegel et al. (1998, SFD) dust map in the

transformed frame of Jet. This map demonstrates that the detection of the Jet stream does not correlate with any linear extinction features.

3.3.2 Distance Gradient

Using the DELVE DR1 catalog cross-matched with *Gaia* EDR3 (Section 3.2.1), we identify candidate BHB stars and use them to measure a distance gradient along the Jet stream. BHB stars are useful for determining a distance gradient because of the tight color-luminosity relation that allows for distance estimates with $\sim 10\%$ uncertainty to an individual BHB star (Deason et al., 2011). To determine a distance gradient we use a similar method to Li et al. (2020) who use BHB stars to measure the distance gradient of the ATLAS-Aliqa Uma stream. For the Jet stream, the gradient derived from BHB stars can be used to refine the matched-filter selection from Section 3.3.1, make a reflex-corrected proper motion measurement in Section 3.3.5, and improve dynamical modeling of the stream (Section 3.4). Hereafter, all proper motions $(\mu^{\star}_{\phi_1}, \mu_{\phi_2})$ are assumed to be reflex corrected unless explicitly stated otherwise. We select probable BHB stars along the track of the stream using a few criteria. Initially we select all sources with $-12^{\circ} < \phi_1 < 10^{\circ}$ and separation from the stream track $\Delta\phi_2 < 0.5^{\circ}$ (Equation 3.2). Then, a color cut is applied to select blue stars keeping only sources with $(g-r)_0$ between -0.3 and 0.0 mag. We then cut all sources with g-band magnitudes less than 17.0 mag or greater than 18.5 mag to reduce contamination from the Milky Way foreground. For each candidate we derive an estimate of its distance modulus, $m - M$, by assuming it is a BHB star and using the relation for M_g vs. $(g-r)_0$ from Belokurov and Koposov (2016).

To further remove contaminant stars from the Jet stream BHB stellar sample, we use the *Gaia* EDR3 proper motions of candidate BHB stars along the Jet stream track. We use the distance estimated for each BHB star to correct their proper motions for the solar reflex motion assuming a relative velocity of the Sun to the Galactic standard of rest to be $(U_{\odot}, V_{\odot}, W_{\odot}) = (11.1, 240.0, 7.3)$ km/s (Bovy et al., 2012a). Figure 3.4 (left panel) shows the resulting measured proper motion of our BHB candidate sample. The proper motion signal

of the Jet stream is seen at $(\mu^{\star}_{\phi_1}, \mu_{\phi_2}) \sim (-1, 0)$ mas/yr, where we define $\mu^{\star}_{\phi_1} = \mu_{\phi_1} \cos(\phi_2)$. The BHB candidates within the green box are selected as likely members of the Jet stream to be used to estimate the distance gradient. Figure 3.4 (right panels) shows on-sky positions and distances of the likely member candidate BHB stars.

Using these derived distances and assuming an uncertainty of 0.1 mag on the distance modulus for each BHB star (Deason et al., 2011), we fit for the distance modulus as a function of position along the stream using a simple linear fit. We find the following relation for the distance modulus as a function of ϕ_1 along the Jet stream,

$$(m - M) = 17.45 - 0.014 \times (\phi_1). \tag{3.3}$$

The heliocentric distance of the Jet stream is found to vary from 26 kpc to 34.5 kpc over its observed length with a gradient of -0.2 kpc/deg.

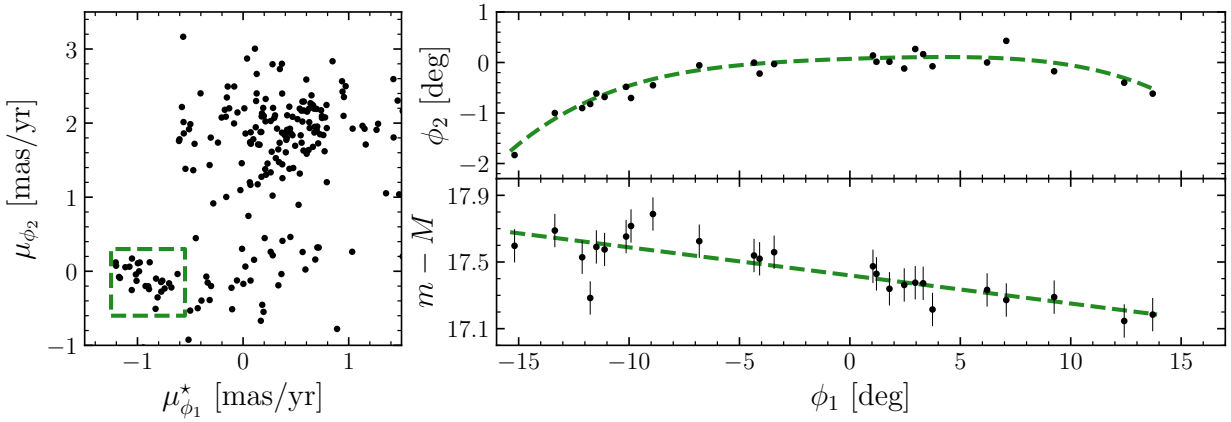

Figure 3.4 *Left:* proper motions of candidate BHB stars along the Jet stream. The green box shows our proper motion selection for likely members. The Milky Way foreground is seen at $(\mu^{\star}_{\phi_1}, \mu_{\phi_2}) \sim (0, 2)$ mas/yr *Right:* on-sky distribution (top) and distances modulus (bottom) of candidate BHB stars that are likely associated with the Jet stream. The matched-filter stream track (Equation 3.2 is shown as green dashed line on the top plot, and the linear fit on distance modulus, $(m - M)$, of the candidate BHB stars (Equation 3.3) is shown as a green dashed line on the bottom plot.

3.3.3 Creation of optimized matched-filter map

We next use our measured distance gradient to find a best-fit isochrone, and create an optimized matched-filter map to study the morphology of the stream. We begin by creating a Hess difference diagram shown in Figure 3.5. This is done by selecting stars along the stream track with $-11^\circ < \phi_1 < -8^\circ$ as well as stars with $-5^\circ < \phi_1 < 6^\circ$, excluding the area around the observed under-density in the stream at $\phi_1 \sim -6.5^\circ$ to increase signal-to-noise. In ϕ_2 we select stars within 2 times the observed width of the stream (w) as a function of ϕ_1 (the width is derived in Section 3.3.4). At $\phi_1 = 0$ we find a width of $w = 0.16^\circ$ and this value varies from $w = 0.13^\circ$ at $\phi_1 = -11^\circ$ to $w = 0.19^\circ$ at $\phi_1 = 6^\circ$. Additionally, a background region is selected to be along the same ϕ_1 range but above and below the stream, with $1^\circ < |\phi_2| < 2^\circ$. For the stars in each of these regions we compute the absolute g-band magnitude (M_g) assuming a distance modulus derived from the observed BHB stars' gradient (Equation 3.3). Then we select only stars with $M_g < 5.47$; this corresponds to the faint limit of our catalog ($g_0 = 23.1$) at $\phi_1 = -13^\circ$, the most distant portion of the detected stream. This absolute magnitude selection ensures that the observed density variations in the matched-filter map are not affected by the survey completeness. We then create binned color–magnitude diagrams (CMDs) for the on-stream and background selections and subtract the background from the on-stream region correcting for relative areas. The result of this process is shown in Figure 3.5.

Next we fit an isochrone to this Hess difference diagram using a similar methodology to Shipp et al. (2018). Briefly, we model the observed binned CMD of the stream region as a linear combination of the background region and a stellar population following a Dotter et al. (2008) isochrone. Then we compute the likelihood that the binned CMD is a Poisson sample of the model. This likelihood is then sampled using `emcee` (Foreman-Mackey et al., 2013). We find a best-fit isochrone consistent with the J18 result and distance modulus in strong agreement with the distance derived from candidate BHB stars ($(m-M)_{MS}-(m-M)_{BHB} = 0.01^{+0.05}_{-0.05}$).

Since we find consistent results, we use the J18 isochrone to create an optimized matched-filter that is used in Section 3.3.4 to quantitatively characterize distance variation. This map covers the region defined by $-16^\circ \leq \phi_1 \leq 17^\circ$, and $-3^\circ \leq \phi_1 \leq 1^\circ$. We choose a pixel size of 0.2 deg in ϕ_1 and 0.05 deg in ϕ_2. The distance modulus of the matched-filter follows Equation 3.3. The result of this more optimal matched-filter is shown in the top panel of Figure 3.6. We note that while the image in Figure 3.6 has been smoothed with a 0.08 deg Gaussian kernel, we do not apply any smoothing when fitting our model to the stream data.

3.3.4 Fitting Stream Morphology

To quantitatively characterize the observed features of the stream morphology we use a generative stream model developed by Koposov et al. (2019) and Li et al. (2020), which is similar to that of Erkal et al. (2017). This model uses natural cubic splines with different numbers of nodes to describe stream properties. This model is implemented in `STAN` (Carpenter et al., 2017) and is fit to the data using the Hamiltonian Monte Carlo No-U-Turn Sampler (NUTS) to efficiently sample the high dimensional parameter space.

The stream is modeled by a single Gaussian in ϕ_2 with central intensity, width, and track that are allowed to vary as functions of ϕ_1. The parameters of the model are $\mathcal{I}(\phi_1)$, $w(\phi_1)$, $\Phi_2(\phi_1)$, $\mathcal{B}_1(\phi_1)$, $\mathcal{B}_2(\phi_1)$, and $\mathcal{B}_3(\phi_1)$, which describe the logarithm of the stream central intensity, the logarithm of the stream width, the stream track, the log-background density, the slope of the log-background density, and the quadratic term of the log-background density, respectively. The model is fit to the binned matched-filter data described above using Equation 3.3 to describe the distance modulus as a function of ϕ_1. We assume the number of stars in an individual pixel of the matched-filter map is a Poisson sample of the model density at that location.

Following Li et al. (2020), we use Bayesian optimization to determine model complexity in a data-driven way. In particular, the number of nodes for all parameters except the stream width are determined through Bayesian optimization (Gonzalez et al., 2016; The GPyOpt authors, 2016) of the cross-validated ($k = 3$) log-likelihood function. For the parameters

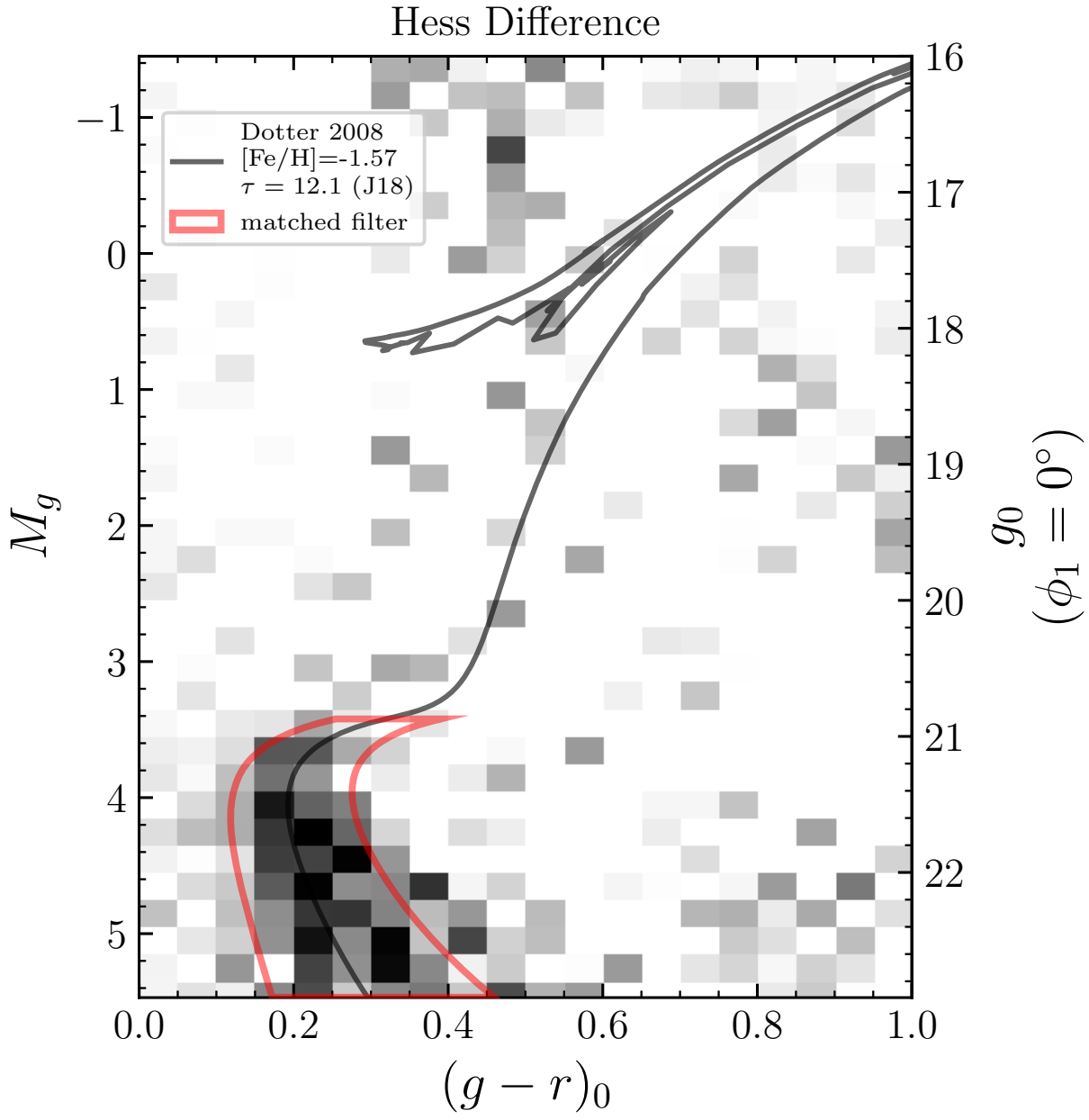

Figure 3.5 Hess difference diagram created by subtracting a background region from the on-stream region. The main sequence of the Jet stream is clearly seen. The Dotter et al. (2008) isochrone we use for our analysis with a metallicity of [Fe/H]$=-1.57$ and age of $\tau = 12.1$ Gyr is shown as a solid black line. The red line shows the matched-filter used to create the optimized map shown in the top row of Figure 3.6. The left y-axis shows the absolute magnitude of sources and the right y-axis shows the corresponding apparent magnitude at $\phi_1 = 0°$.

[$\mathcal{I}(\phi_1)$, $w(\phi_1)$, $\Phi_2(\phi_1)$, $\mathcal{B}_0(\phi_1)$, $\mathcal{B}_1(\phi_1)$, $\mathcal{B}_2(\phi_1)$] we find the optimal number of nodes to be [11, 3, 8, 28, 25, 5], respectively. For each parameter, the range of allowable nodes is 3 to 30 except for the width, $w(\phi_1)$, and quadratic term of the log-background density, $\mathcal{B}_3(\phi_1)$, which have their maximum number of nodes constrained to 15 and 10, respectively. The model is run for 1500 iterations with the first 700 discarded as burn in.

The results of the model fit are shown in Figures 3.6 and 3.7. For Figure 3.6 the top row shows the observed matched-filter map, the best-fit model is shown on the second in the same color scale, and the residual of the model subtracted from the data is shown on the bottom row. The key features captured by this model are the variations in the density of stars. A large gap can be seen at $\phi_1 = -6°$, and peaks in the intensity are found at at $\phi_1 = -9°, -2.5°$ and $4°$. The model does not capture all of the observed small-scale substructure. In particular, the off-track structure seen crossing the stream at $\phi_1 = -12$ or the overdensity above the stream at $\phi_1 = 5\,°$ are discussed in more detail in Section 3.5.2.

The nature of the on-stream structure can be better evaluated by looking at the extracted stream parameters in Figure 3.7. These plots show the stream surface brightness, the on-sky track, stream width and linear density. In each panel, the best-fit value calculated as the maximum *a posteriori* (MAP) of the posterior for each parameter as a function of ϕ_1 is shown as a black line, and the 68% containment peak interval is shown as the blue shaded region. The apparent width of the stream increases with ϕ_1, consistent with expected projection effects due to a constant width and the observed distance gradient. This is supported by the relatively constant linear density over large scales.

3.3.5 Proper Motion of the Jet Stream

In this section, we use the cross-matched DELVE DR1 and *Gaia* EDR3 catalog to measure the proper motion of the Jet stream. In Section 3.3.2 we demonstrated that the proper motion signature of BHB stars could be clearly separated from the Milky Way foreground. We seek to extend our analysis to the full stellar population of Jet, applying several additional physically motivated cuts to reduce Milky Way foreground contamination. Then we perform

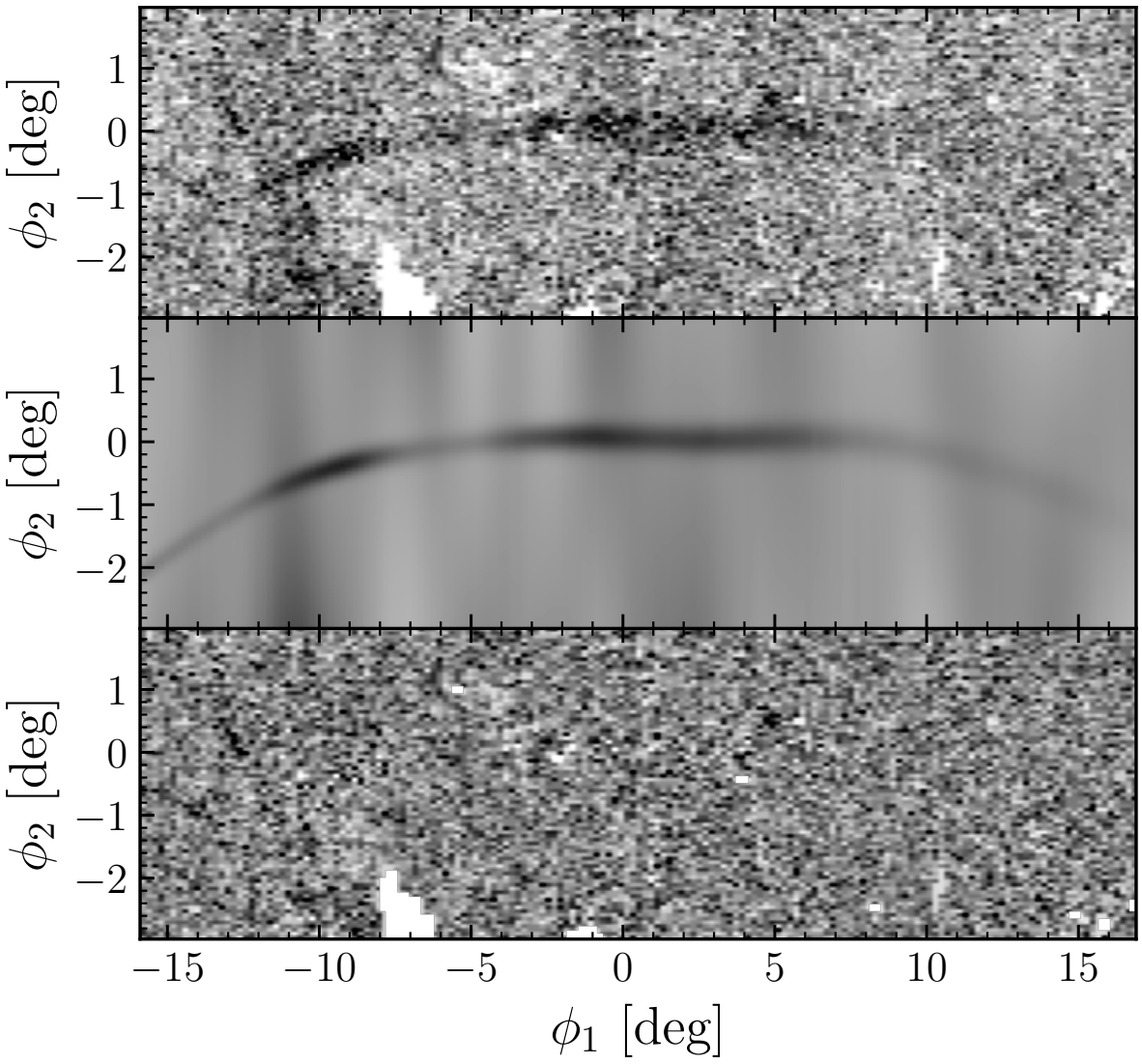

Figure 3.6 Modeling the track, width, and intensity of the Jet stream from DELVE DR1 photometric data. *Top:* The density of stars that pass the optimized matched-filter selection that takes into account the observed distance gradient in the region of the Jet stream. *Middle:* The maximum *a posteriori* (MAP) model of the data shown in the top panel containing both stream and background components. *Bottom:* The residual density map showing the observed density minus the model.

a Gaussian mixture model fit with stream and Milky Way components to measure the proper motion of Jet.

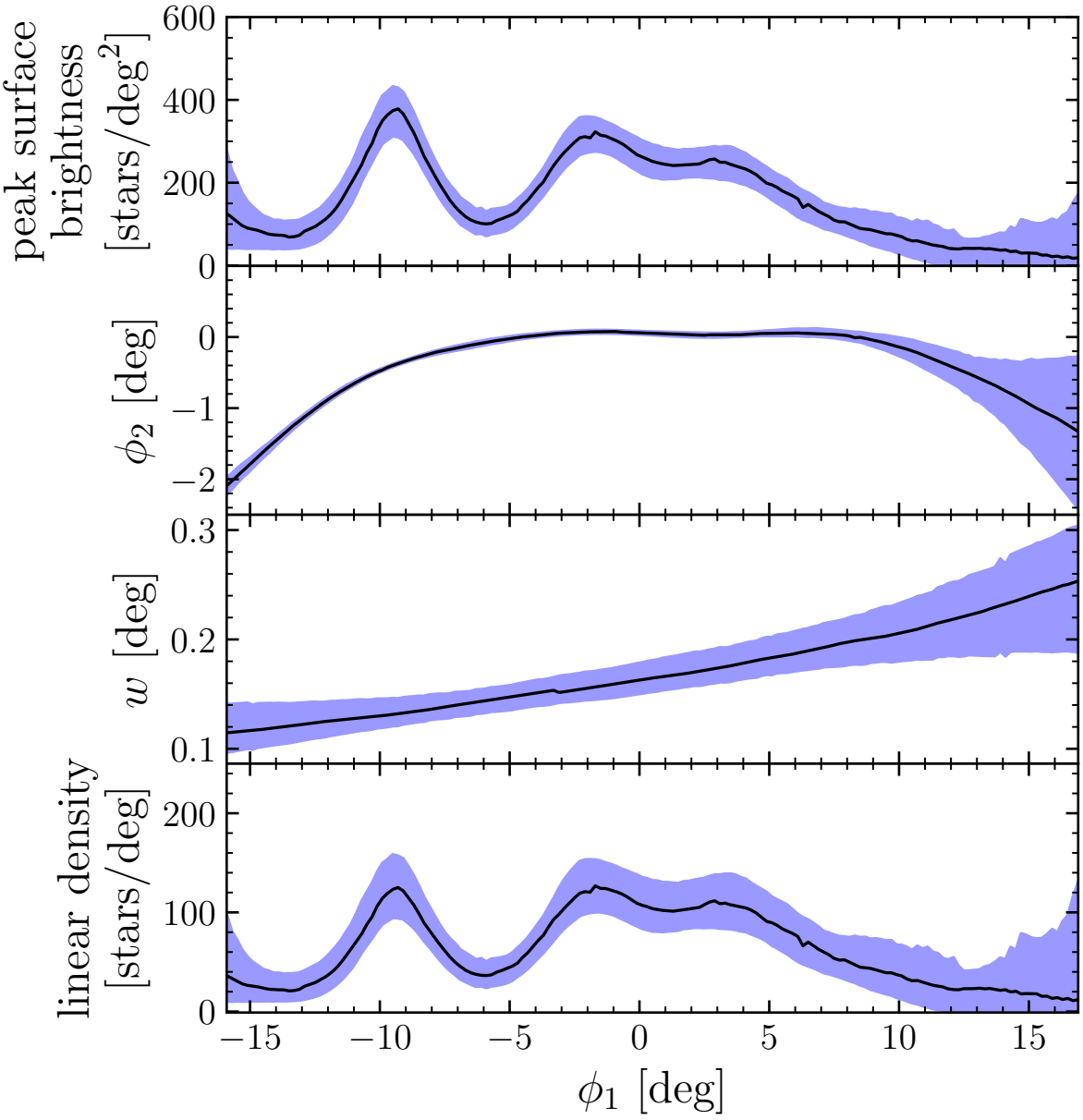

Figure 3.7 Measurement of Jet stream parameters as a function of position along the stream (ϕ_1) as derived from modeling the DELVE DR1 stellar density maps. From top to bottom are stream surface brightness, stream track, stream width, and linear density. The shaded area shows the 68% containment peak interval, and the black line shows the best-fit estimate of each parameter.

3.3.5.1 Data Preparation

Starting with the stellar catalog from Section 3.2.1, we apply several cuts to reduce Milky Way contamination in our sample and to highlight the Jet stream population. These cuts are depicted visually in the left two panels of Figure 3.8. The following selection process largely follows the methodology set out by Shipp et al. (2019) and Li et al. (2019).

We begin by calculating the absolute magnitude in the g-band (M_g) for each star assuming a distance given by the fit to the BHB stars (Equation 3.3; $m - M(\phi_1)$). A magnitude cut is made keeping only sources with $M_g < 2$ to remove faint sources with large proper motion uncertainties. Then, a color–magnitude selection is applied selecting stars in $(g-r)_0$ vs. M_g color–magnitude space (Fig. 3.8 left panel). RGB stars are selected based on the Dotter et al. (2008) isochrone used in Section 3.3.1. We select stars that meet either of the following conditions:

$$\begin{aligned} -0.08 \leq \quad & (g-r)_0 - (g-r)_{\rm Dotter} \quad \leq 0.02 \\ -0.5 \leq \quad & g_0 - (g_0)_{\rm Dotter} \quad \leq 0.5. \end{aligned} \tag{3.4}$$

where $(g-r)_{\rm Dotter}$ is the isochrone color at a given observed magnitude and $(g_0)_{\rm Dotter}$ is the isochrone magnitude at a given observed color. Next, we applied a $(g-r)_0$ vs. $(r-i)_0$ color–color cut to select metal poor stars based on an empirical stellar locus that is derived from dereddened DES data (second panel; Pace and Li, 2019; Li et al., 2018). This locus gives the median $(r-i)_0$ colors for each $(g-r)_0$ bin, For each star we compute $\Delta_{ri} = (r-i)_0 - (r-i)_{\rm med}$ where $(r-i)_0$ is the observed color of a star and $(r-i)_{\rm med}$ is the median $(r-i)_0$ color of stars with the same $(g-r)_0$ color taken from the empirical stellar locus. Only stars within $-0.02 < \Delta_{ri} < 0.1$ are kept. Finally, a spatial cut is applied only keeping stars within $3 \times w(\phi_1)$ of the stream track where $w(\phi_1)$ is the stream width and track taken from the modeling in Section 3.3.4.

To select candidate horizontal branch members for the proper motion fit, we use an em-

pirical horizontal branch of M92 initially derived in Belokurov et al. (2007) and transformed to the DES photometric system (Li et al., 2019; Pace and Li, 2019). We select stars with $(g-r)_0$ colors within ± 0.1 mag and M_g within ± 0.5 mag of the empirical horizontal branch.

After applying these cuts, we perform a reflex correction on the proper motion measurements of the remaining sources (assuming the distance fit from Equation 3.3). The proper motion signal of Jet is easily identified in the third panel of Figure 3.8 as the overdensity at $(\mu_{\phi_1}^\star, \mu_{\phi_2}) \sim (-1, 0)$ mas/yr. To quantitatively measure the proper motion and any gradient in the proper motion, we use a Gaussian mixture model based analysis described in the following section.

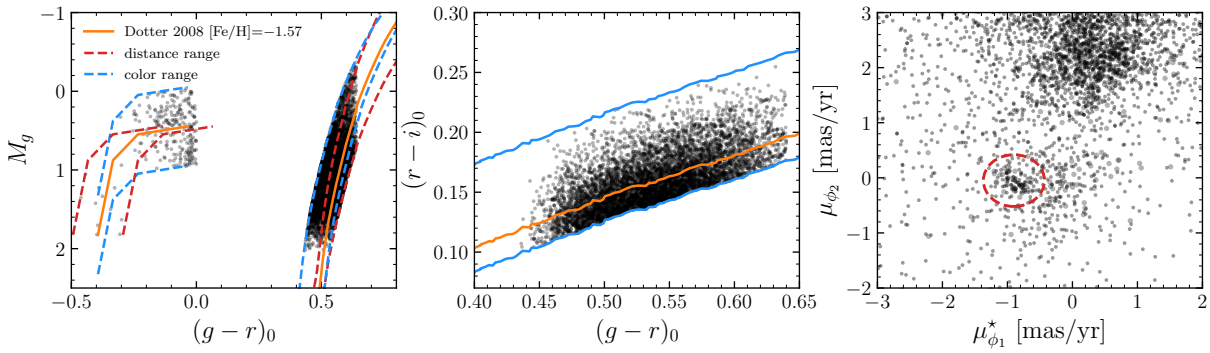

Figure 3.8 Selection of stars used to measure the proper motion of the Jet stream. *Left:* A color–magnitude diagram demonstrating the selection applied to the data. The orange lines show the empirical M92 horizontal branch and Dotter isochrone ([Fe/H] $=-1.57$) used to select data. The blue dashed lines show our selection range in distance, and the red dashed lines our selection range in color. *Center:* A color-color plot showing our selection range in blue around an empirical stellar locus of dereddened DES photometry in orange. *Right:* Proper motion in stream coordinates of the sample of stars passing all selection cuts. The signal from the Jet stream is easily seen at $(\mu_{\phi_1}^\star, \mu_{\phi_2}) \sim (-1, 0)$ mas/yr (circled in red).

3.3.5.2 Mixture Model

To determine the proper motion of the Jet stream, we use a simple mixture model consisting of Gaussian distributions for the stream and Milky Way foreground. The fit is performed

on the candidate RGB and BHB stellar sample defined in the previous section and shown in the right panel of Figure 3.8. The likelihood and fitting methodology follows that of Pace and Li (2019) and Shipp et al. (2019). The complete likelihood is given by:

$$\mathcal{L} = (1 - \lambda)\mathcal{L}_{\rm Jet} + \lambda\mathcal{L}_{\rm MW} \tag{3.5}$$

where $\mathcal{L}_{\rm Jet}$ is the likelihood that a star belongs to the Jet stream component, and $\mathcal{L}_{\rm MW}$ refers to the likelihood that a star belongs to the Milky Way foreground component. The fraction of stars that belong to the Milky Way component is denoted by λ. Each likelihood term is made up of the product of both spatial and proper motion likelihoods,

$$\mathcal{L}_{\rm Jet/MW} = \mathcal{L}_{\rm spatial}\, \mathcal{L}_{\rm PM}. \tag{3.6}$$

For the stream spatial component we use the results from Section 3.3.4 for the stream track, $\Phi_2(\phi_1)$, and width, $w(\phi_1)$, assuming the stream follows a Gaussian distribution in ϕ_2 around this track (i.e. $\phi_{2,\rm obs} - \Phi_2(\phi_1)$ with standard deviation $w(\phi_1)$. The Milky Way spatial component is assumed to be uniform.

$$\mathcal{L}_{\rm spatial} = \begin{cases} \mathcal{N}(\phi_2 \,|\, \Phi_2(\phi_1), w_{\rm Jet}) & \text{Jet component} \\ \text{Uniform} & \text{MW component} \end{cases} \tag{3.7}$$

The proper motion term of the likelihood is modeled by the combination of several multivariate Gaussians. Each Gaussian is defined to have a mean proper motion vector $\boldsymbol{\chi}$ given by $\boldsymbol{\chi} = (\mu^{\star}_{\phi_1,Jet}(\phi_1), \mu_{\phi_2,Jet}(\phi_1))$. We model both components of $\boldsymbol{\chi}$ as a linear functions of ϕ_1. The covariance, $\boldsymbol{C}$, is defined by an observational error component and an intrinsic

component:

$$\begin{aligned}\boldsymbol{C} &= \boldsymbol{C}_{obs} + \boldsymbol{C}_{intrinsic} \\ &= \begin{bmatrix} \epsilon^2_{\mu_{\phi_1}\cos\phi_2} & \epsilon_{\mu_{\phi_1}\cos\phi_2 \times \mu_{\phi_2}} \\ \epsilon_{\mu_{\phi_1}\cos\phi_2 \times \mu_{\phi_2}} & \epsilon^2_{\mu_{\phi_2}} \end{bmatrix} + \\ &\quad \begin{bmatrix} \sigma^2_{\mu_{\phi_1}\cos\phi_2} & \sigma_{\mu_{\phi_1}\cos\phi_2} \times \sigma_{\mu_{\phi_2}} \times \rho \\ \sigma_{\mu_{\phi_1}\cos\phi_2} \times \sigma_{\mu_{\phi_2}} \times \rho & \sigma^2_{\mu_{\phi_2}} \end{bmatrix}\end{aligned} \tag{3.8}$$

where ϵ represents the proper motion errors, σ is the intrinsic proper motion dispersions, and ρ is a correlation term. For the stream component, the intrinsic dispersion is assumed to be $5\,\mathrm{km/\,s} \sim 0.04\,\mathrm{mas/\,yr}$ and the correlation terms are assumed to be zero.

The model then has 9 free parameters: The systemic proper motions of the stream measured at $\phi_1 = 0^\circ$ $(\bar{\mu}_{\phi_1}\cos(\phi_2), \bar{\mu}_{\phi_2})$, the proper motion gradients in each coordinate direction for the stream $(d\mu_{\phi_1}/d\phi_1, d\mu_{\phi_2}/d\phi_1)$ in units of mas/10°, the mean proper motion of the Milky Way foreground Gaussian $(\mu_{\phi_1\,\mathrm{MW}}, \mu_{\phi_2\,\mathrm{MW}})$, the dispersion of the Milky Way foreground Gaussian $(\sigma_{\phi_1\,\mathrm{MW}}, \sigma_{\phi_2\,\mathrm{MW}})$, and the fraction of stars that belong to the stream component (λ). The proper motion of the stream component as a function of ϕ_1 is given by

$$\begin{aligned}\mu_{\phi_1,\mathrm{Jet}}(\phi_1) &= \bar{\mu}_{\phi_1} + \frac{d\mu_{\phi_1}}{d\phi_1} \times (\phi_1/10\,\mathrm{deg}) \\ \mu_{\phi_2,\mathrm{Jet}}(\phi_1) &= \bar{\mu}_{\phi_2} + \frac{d\mu_{\phi_2}}{d\phi_1} \times (\phi_1/10\,\mathrm{deg}).\end{aligned} \tag{3.9}$$

The total proper motion likelihood is then given by

$$\mathcal{L}_{\mathrm{PM}} = \sum_{N=1}^{k} \mathcal{N}((\boldsymbol{\mu}^{\star}_{\phi_1,obs}, \boldsymbol{\mu}_{\phi_2,obs})_N \,|\, \boldsymbol{\chi}_{true,N}\,, \boldsymbol{C_N}). \tag{3.10}$$

Parameter inference is conducted using a Hamiltonian Monte Carlo No-U-Turn Sampler (NUTS) implemented in `STAN` (Carpenter et al., 2017). We use 10 parallel chains with 2000 iterations each (1000 of the iterations are discarded as a burn in). Convergence is verified

using the Gelman-Rubin $\hat{R} < 1.1$ diagnostic (Gelman and Rubin, 1992).

The results of our fit are listed in Table 3.3.5.2. We find the results from the mixture model $(\bar{\mu}^{\star}_{\phi_1,\mathrm{Jet}}, \bar{\mu}_{\phi_2,\mathrm{Jet}}) = (-0.942 \pm 0.015, -0.057 \pm 0.014)$ mas/yr, which agrees with our rough estimate from the observed overdensity of candidate BHB stars in Section 3.3.2. The $\bar{\mu}_{\phi_2}$ value is near zero as expected for a stable stream that has not been heavily perturbed. We detect gradients in both proper motion coordinates that are similar in magnitude. Based on these results, the tangential velocity of the Jet stream at $\phi_1 = 0°$ is $v_{tan} = 195 \pm 3$ km/s.

A membership probability is calculated for each star by taking the ratio of the stream likelihood to the total likelihood: $p_{mem} = \lambda\mathcal{L}_{\mathrm{Jet}}/(\lambda\mathcal{L}_{\mathrm{Jet}} + (1-\lambda)\mathcal{L}_{\mathrm{MW}})$. To determine the value of $p_{mem,i}$ for each star we calculate p_{mem} for each point in the posterior of our fit and take $p_{mem,i}$ to be the median of the calculated values for each star. A star is then considered a high (medium) probability member if $p_{mem,i} > 0.8$ (0.5). For our sample, 75 (92) candidate RGB stars and 28 (28) candidate BHB stars pass this criteria.

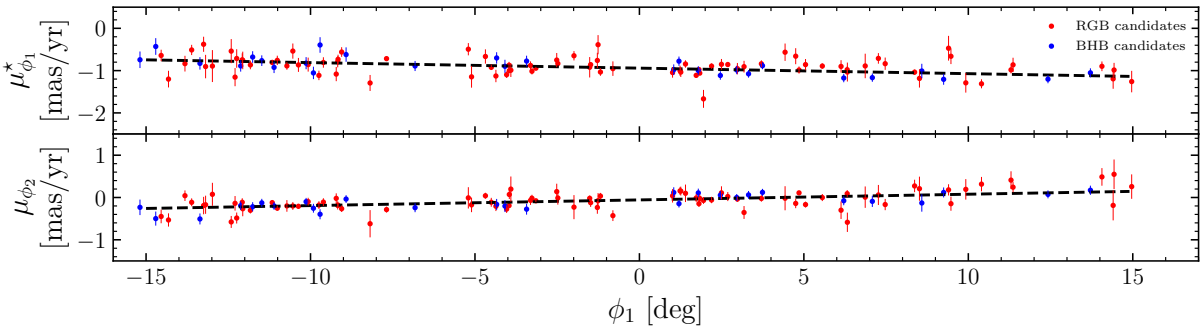

Figure 3.9 Proper motion of high probability member RGB (red) and BHB (blue) stars ($p_{mem} > 0.8$). Additionally the line of best-fit proper motion is shown as a black dashed line. All the BHB stars used to measure the distance gradient are also high probability members.

The proper motion of the high probability stars are shown in Figure 3.9 along with lines showing the best-fit stream proper motion $(\bar{\mu}^{\star}_{\phi_1}(\phi_1), \bar{\mu}_{\phi_2}(\phi_1))$ from our analysis. The BHB stellar sample (blue points) is almost identical to the sample selected by a rough cut in

Table 3.1. Results of the proper motion fit in reflex corrected proper motion coordinates

Parameter	Value	Prior	Range	Units
$\bar{\mu}^{\star}_{\phi_1}$	-0.942 ± 0.015	Uniform	-10,10	mas/yr
$\bar{\mu}_{\phi_2}$	-0.057 ± 0.014	Uniform	-10,10	mas/yr
$d\mu^{\star}_{\phi_1}/d\phi_1$	-0.131 ± 0.023	Uniform	-3,3	mas/yr/10 deg
$d\mu_{\phi_2}/d\phi_1$	0.134 ± 0.019	Uniform	3,3	mas/yr/10 deg
λ	0.081 ± 0.010	Uniform	0,1	

Figure 3.4, and it can be seen that these stars closely follow the proper motion gradient ($d\mu/d\phi_1$) found in our analysis. In Appendix B.1, we include Table B.1 that contains the properties of all candidate BHB and RGB stars with membership probability (p_{mem}) higher than 10%. With the current dataset we are only able to fit for linear evolution of the proper motion with ϕ_1, but with future spectroscopic datasets can test for a more complex evolution of the proper motion as a function of ϕ_1 (e.g., quadratic).

Previous studies such as Shipp et al. (2019) have looked for signs of large scale perturbation of stellar streams from the influence of the LMC or Milky Way bar (Li et al., 2018; Erkal et al., 2018; Koposov et al., 2019; Vasiliev et al., 2021). Evidence of these interactions sometimes appears as a mismatch between the proper motion of the stream ($\mu_{\phi_2}/\mu_{\phi_1}$) and the derivative of the stream track ($d\phi_2/d\phi_1$) (Erkal et al., 2019). In the case of Jet, we find that the ratio of the proper motions to the stream track $(\mu_{\phi_2}/\mu_{\phi_1})/(d\phi_2/d\phi_1)$ has an average value of 2.00 ± 1.18 over the extent of the stream. This is consistent with a value of one which indicates the proper motions are largely aligned with the track of the stream.

3.4 Dynamical Modeling

Using our measurements of the stream track, distance, and proper motion, we can fit a dynamical model to the data. The Jet stream is modeled in the same method as Erkal et al. (2019) and Shipp et al. (2021). We make use of the modified Lagrange Cloud Stripping (mLCS) technique developed in Gibbons et al. (2014) adapted to include the total gravi-

tational potential of the stream progenitor, the Milky Way, and the LMC. Following Erkal et al. (2019), the Milky Way and LMC are modeled as independent particles with their respective gravitational potentials which allows us to capture the response of the Milky Way to the LMC. The Milky Way potential is modeled with 6 axisymmetric components, namely bulge, dark matter halo, thin and thick stellar disk, and HI and molecular gas disk components following McMillan (2017). Following Shipp et al. (2021), we normalize the Milky Way potential to the realization of the McMillan (2017) potential that yields the best-fit from the ATLAS data ($M_{\rm MW} = 8.3 \times 10^{11} M_\odot$; Li et al., 2020). We evaluate the acceleration from the potential using `galpot` (Dehnen and Binney, 1998). We take the Sun's position ($R_0 = 8.23$ kpc) and 3D velocity, $(\mathrm{U}_\odot, \mathrm{V}_\odot, \mathrm{W}_\odot) = (8.6, 232.8, 7.1)$ km/s, from McMillan (2017).

We model the mass distribution of the LMC as a stellar disk and a dark matter halo. The stellar disk is modelled as a Miyamoto-Nagai disk (Miyamoto and Nagai, 1975) with a mass of $3 \times 10^9 M_\odot$, a scale radius of 1.5 kpc, and a scale height of 0.3 kpc. The orientation of the LMC disk matches the measurement of van der Marel and Kallivayalil (2014). The LMC's dark matter halo is modelled as a Hernquist profile (Hernquist, 1990). We fix the total infall mass of the LMC to $1.5 \times 10^{11}\,\mathrm{M}_\odot$, consistent with the value derived in Erkal et al. (2019) and Shipp et al. (2021). We fix the scale radius to match the circular velocity measurement of 91.7 km/s at 8.7 kpc from van der Marel and Kallivayalil (2014). Note that this is in agreement with more recent measurements of the LMC's circular velocity (e.g., Cullinane et al., 2020). We account for the dynamical friction of the Milky Way on the LMC using the results of Jethwa et al. (2016). We also fix the LMC's present-day proper motion, distance, and radial velocity to measured values (Kallivayalil et al., 2013; Pietrzyński et al., 2013; van der Marel et al., 2002). The LMC mass remains fixed throughout each simulation.

We model the potential of the Jet stream's progenitor as a Plummer sphere (Plummer, 1911) with a mass and scale radius chosen to match the observed stream width. During the course of tidal disruption, the progenitor's mass decreases linearly in time to account for tidal stripping. Since Jet does not have a known progenitor, we assume that the progenitor

has completely disrupted, i.e., that its present day mass is zero. Furthermore, we assume that the remnant of the progenitor is located at $\phi_1 = 0°$.

We calculate the likelihood for the stream model by producing a mock observation of a simulated stream and comparing it with the data described in the previous sections. For each stream model, we calculate the track on the sky, the radial velocity, the proper motions in ϕ_1 and ϕ_2, and the distance as functions of ϕ_1, the observed angle along the stream. We assign the mass of the progenitor in order to reproduce the observed width of the stream. Our best-fit model uses a progenitor mass of $M_{\rm prog} = 2 \times 10^4\,{\rm M}_\odot$, and a Plummer scale radius of $r_{\rm plum} = 10\,{\rm pc}$. We note that these values are highly dependent on the location of the progenitor.

We perform a Markov Chain Monte Carlo (MCMC) fit using `emcee` (Foreman-Mackey et al., 2013). Our model includes 5 free parameters. We fit the present-day progenitor ϕ_2 position, distance, radial velocity, and proper motion. The prior distributions on each parameter are listed in Table 3.4. The position of the progenitor along the stream is fixed to $\phi_1 = 0°$ (i.e., the middle of the stream's observed extent). We show the Jet data and the best-fit stream models in Figure 3.10. In each panel we show the observations in red, and simulated stream in blue. The radial velocity panel contains no observations, but can be used to predict the radial velocity of the stream. We find the best-fit model is a good fit to the observations of the distance modulus, stream track and proper motions.

We have tried fits that include/exclude the effect of the LMC and Milky Way bar. For the Milky Way bar we assume an analytic model with the same parameters as used in Li et al. (2020) (described in their Section 5.2.1) and Shipp et al. (2021). For both cases, the LMC and Milky Way bar, we find that it is unlikely that the Jet stream has been significantly affected by these substructures.

This model emphasizes some of the observed features of the Jet stream discussed in Sections 3.3.4 and 3.3.5. None of the intensity features gaps/peaks are seen in the model, and we also fail to replicate the off-track features seen in the photometry.

Table 3.2. Priors on the dynamical model

Parameter	Prior	Range	Units	Description
$\phi_{2,\mathrm{prog}}$	Uniform	(-1, 1)	deg	Location of the progenitor perpendicular to the stream track.
$\mu_{\alpha,\mathrm{prog}}, \mu_{\delta,\mathrm{prog}}$	Uniform	(-10, 10)	mas/yr	Reflex-corrected proper motion of the progenitor.
$v_{\mathrm{r,prog}}$	Uniform	(-500, 500)	km/s	Radial velocity of the progenitor.
$(m-M)_{\mathrm{prog}}$	Normal	$(m-M)_0 \pm 0.2$	mag	Distance modulus of the progenitor.
$\phi_{1,\mathrm{prog}}$	Fixed	0	deg	Location of the progenitor along the stream track.
M_{LMC}	Fixed	1.5×10^{11}	$\mathrm{M}_\odot$	Total mass of the LMC.
$\mu_{\alpha,\mathrm{LMC}}$	Normal	1.91	mas/yr	Proper motion of the LMC in RA.
$\mu_{\delta,\mathrm{LMC}}$	Normal	0.229	mas/yr	Proper motion of the LMC in Dec.
$v_{\mathrm{r,LMC}}$	Normal	262.2	km/s	Radial velocity of the LMC.
d_{LMC}	Normal	49970.0	pc	Distance of the LMC.

3.5 Discussion

3.5.1 Properties of the Jet stream

The Jet stream is now detected from $-15.2^\circ \leq \phi_1 \leq 13.7^\circ$ increasing its known length from $\sim 11^\circ$ to nearly 29°. For $\sim 23^\circ$ ($-13^\circ \leq \phi_1 \leq 10^\circ$) the main sequence turn off of the stream is strongly detected in the DELVE photometry; at $\phi_1 < -13^\circ$ and $> 10^\circ$ the intensity of the stream decreases greatly, and so is only significantly detected using BHB and RGB stars with measured proper motions. At observed distances ranging from $\sim 26 - 34.5$ kpc, the stream has a physical length of 16 kpc, with a strong photometric detection covering 13.4 kpc. This makes the extent of the Jet stream comparable to the kinematically cold Phoenix, ATLAS, and GD-1 streams (Balbinot et al., 2016; Koposov et al., 2014; Grillmair and Dionatos, 2006), which span ~ 5 kpc (13.6°; Shipp et al., 2018), ~ 12 kpc (34° including Aliqa Uma; Li et al., 2020) and ~ 15.4 kpc ($\sim 100^\circ$; de Boer et al., 2020; Webb and Bovy, 2019; Price-Whelan and Bonaca, 2018; Malhan et al., 2018), respectively. Our dynamical models place Jet on a retrograde orbit with a pericenter of 12.7 kpc which is comparable to the pericenters of Phoenix (~ 13 kpc; Wan et al., 2020) ATLAS (13.3 kpc; Li et al., 2020), and GD-1 (~ 14 kpc; Koposov et al., 2010).

As discussed in Section 3.3.5, the proper motion of the Jet stream members and the observed track of the stream are fairly well aligned, suggesting that the Jet stream has not

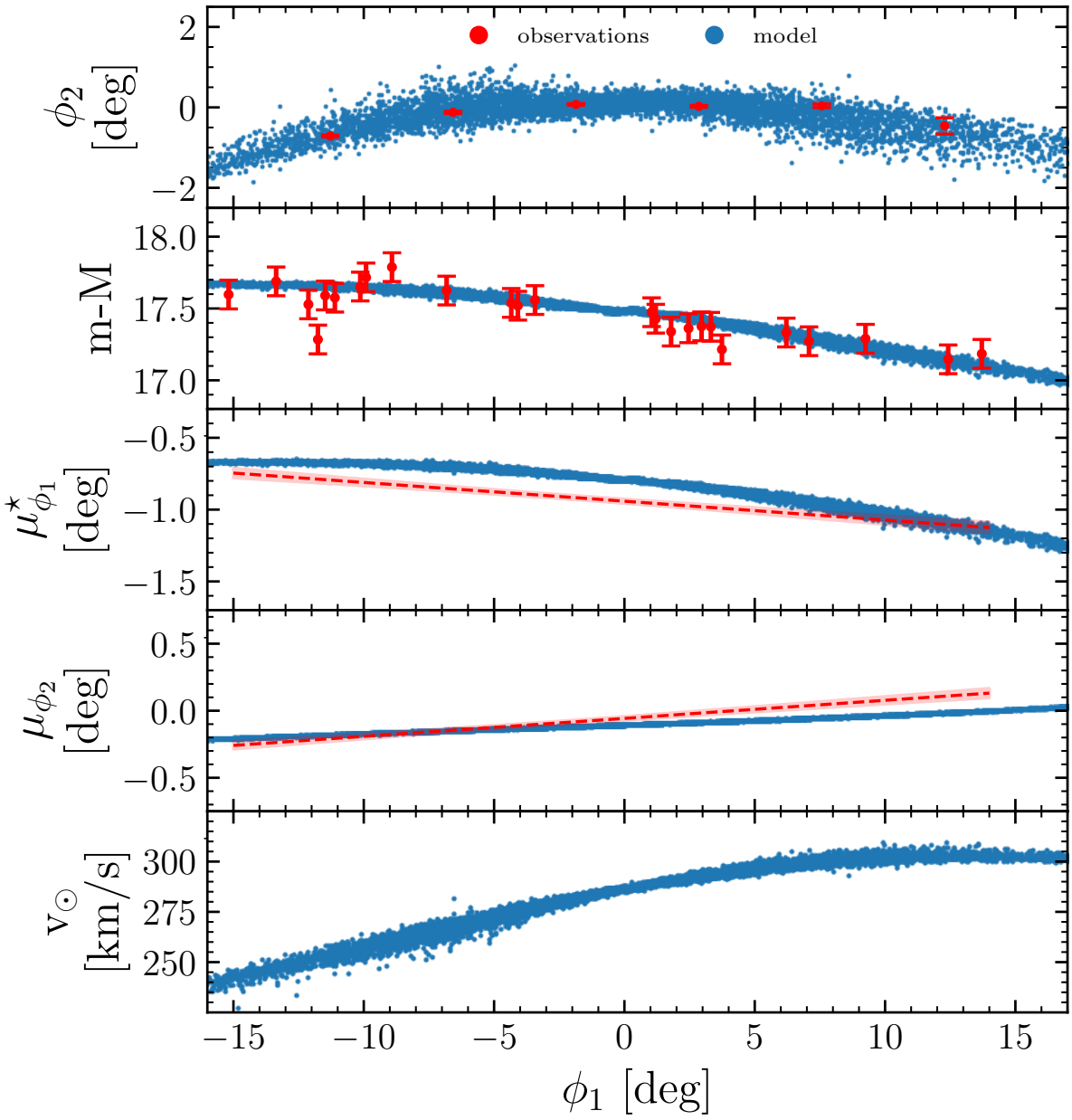

Figure 3.10 Best-fit stream model to the Jet stream. In each row the dark blue points show the best-fit stream model and the red points show the observations to which the model was fit. *First row:* the on-sky distribution of the stream. *Second row:* the distance modulus of the stream. *Third and Fourth rows:* The reflex-corrected proper motions of the stream in ϕ_1 and ϕ_2 respectively. *Fifth row:* predicted heliocentric velocities of the stream.

been strongly perturbed perpendicular to the line of sight from interactions with large Milky Way substructures. However, perturbations in the radial or track direction are difficult to

measure from proper motion alone.

3.5.2 Small-Scale Features

This detailed view of the Jet stream has started to reveal its complexity, adding it to the group of streams that show small-scale features (e.g., Erkal et al., 2017; Price-Whelan and Bonaca, 2018; Li et al., 2020; Caldwell et al., 2020). Most noticeably, a $\sim 4^\circ$ gap in the stream is seen centered on $\phi_1 = -6^\circ$ extending from -. This structure may be due to interactions between the Jet stream and its environment (e.g., a dark matter subhalo passing by and perturbing the stream). Alternatively, this structure could also be the result of a complete dissolution of the progenitor as suggested by Webb and Bovy (2019) in relation to the GD-1 stream. Understanding the nature of this gap will be important for future studies with deeper photometry and radial velocities of member stars near this region. We also note that in the top row of Figure 3.6 the stream looks extremely clumpy on smaller scales than our model probes. Deeper photometric observations, such as those possible with the Vera C. Rubin Observatory's Legacy Survey of Space and Time (LSST), will increase the signal-to-noise of these features, allowing better modeling and therefore a more complete understanding of the system. Finally, there are density features seen off of the main track of the stream. At $\phi_1 \sim 5^\circ$ a signal is seen in the matched-filter map just above the stream (Figure 3.6). This could be a substructure similar to the "spur" of GD-1 (Price-Whelan and Bonaca, 2018) or evidence of some other type of interaction. At $\phi_1 \sim -12.5^\circ$, a feature is seen both above and below the stream; it is possible that the increased reddening in this region is causing this feature, or it could be even more evidence of past interactions between the Jet stream and other substructure. To fully understand these features, followup spectra will be crucial, as these observations will enable the use of radial velocities and metallicities to robustly identify members, as well as allow for the use of the 6D information of members in these off track features to determine their origin.

The observations of small-scale structure in the Jet stream are particularly interesting given its orbital properties. The Jet stream's current Galactocentric radius ($r_G = 30 - 37$

kpc), orbital pericenter (r_{peri} = 12.7 kpc), lack of perturbation from the Milky Way bar in our simulations, and retrograde orbit suggest the Jet stream is less likely to have been perturbed on small scales due to interaction with baryonic matter (Pearson et al., 2017; Banik et al., 2021). This indicates that the Jet stream is likely be one of the best known streams for constraining dark matter substructure in the Milky Way.

3.5.3 Stream Mass and Progenitor Properties

Based on the DELVE photometry, Jet appears to be another stellar stream with no obvious detected progenitor (e.g., Phoenix, ATLAS, GD-1, and many others). Although we do not detect a progenitor for Jet, we can use our observations and modeling to further constrain the properties of the progenitor of the Jet stream. J18 determined the current stellar mass of the Jet stream by fitting the observed stream-weighted CMD and found that the total stellar mass is $2.5 \pm 0.2 \times 10^4\,\mathrm{M}_\odot$. We can set a lower limit on the stellar mass of the Jet stream using the number of high confidence BHB candidates we detect. Based on the color–magnitude and proper motion selections applied in Sections 3.3.2 and 3.3.5, we detect 28 high confidence BHB candidates along the stream. Assuming a Chabrier (2001) initial mass function, an age of 12.1 Gyr and a metallicity of [Fe/H]=−1.57, we find that a stellar mass of $2.6^{+0.6}_{-0.4} \times 10^4\,\mathrm{M}_\odot$ is required to produce the observed number of BHB stars. This estimate is in good agreement with the previous results of J18.

Erkal et al. (2016) suggested that the total dynamical mass of a stream can be estimated from its width. This was used by Shipp et al. (2018) to estimate dynamical masses of the DES streams, and J18 applied the same procedure to estimate that the total dynamical mass of the Jet progenitor is expected to be $\sim 6.4 \times 10^4\,\mathrm{M}_\odot$. In this analysis, we find the observed angular width of Jet varies by a factor of ~ 2 over its extent (Section 3.3.4). However, if we account for the measured distance gradient (Section 3.3.2), the observations are consistent with a constant physical width of $\sim$ 90 pc over the range $\phi_1 = -12^\circ - 10^\circ$. The stream appears to fan out even more in the region $\phi_1 > 10^\circ$ where the intensity of the stream drops greatly. The observed complex physical structure makes it difficult to motivate the simple

scaling between stream width and dynamical mass from Erkal et al. (2016). Thus, we instead estimate the dynamical mass from the best-fit orbital model of the Jet stream described in Section 3.4. We find that these simulations prefer a total dynamical mass of $\sim 2 \times 10^4\,\mathrm{M}_\odot$ which is a factor of ~ 3 less massive than the estimate of J18, but our mass estimate is highly dependent on the location of the progenitor which we assume is $\phi_1 = 0°$. For a progenitor at $\phi_1 = 20°$ we find a worse fit to the overall stream properties but recover a dynamical mass consistent with J18. The ratio of stellar and dynamical mass (~ 1) supports the hypothesis that the progenitor of Jet was a globular cluster ($\mathrm{M/L} \sim 1 - 2$; Kruijssen, 2008) rather than a dwarf galaxy ($\mathrm{M/L} \sim 10^2 - 10^4$ for $\mathrm{L} \sim 2 \times 10^4$; Simon, 2019).

The results of our MCMC modeling can be used to estimate the heliocentric velocity ($\mathrm{v}_\odot$) of the stream and other orbital parameters. We find a predicted heliocentric velocity at $\phi_1 = 0°$ of $\mathrm{v}_\odot = 286 \pm 10\,\mathrm{km/\,s}$.[4] For the orbit of Jet we find a pericenter of $r_{\mathrm{peri}} = 12.7 \pm 0.9\,\mathrm{kpc}$, an apocenter of $r_{\mathrm{apo}} = 38 \pm 1\,\mathrm{kpc}$, and an eccentricity of 0.59 and an orbital period of 0.5 Gyr.

These orbital properties can be used to explore whether Jet could be associated with other known globular clusters or streams. The predicted R_v estimate, along with the measured proper motion of the Jet stream, give an expected angular momentum perpendicular to the Galactic disk ($\hat{z}$ direction) L_z and total energy E_{tot}. These two quantities, L_z and E_{tot}, are both conserved assuming a static axis-symmetric Milky Way potential. To compute these parameters we use the same Milky Way plus LMC potential from Section 3.4. We randomly draw from the posteriors of our fit values for the proper motions, ϕ_2 position and radial velocity of the Jet stream at $\phi_1 = 0°$, and repeat this 1000 times. Then for each draw we compute the L_z and E_{tot} of the Jet stream at $\phi_1 = 0°$. Doing this we find the predicted L_z and E_{tot} of the Jet stream to be $L_z = 1.9 \pm 0.1\,\mathrm{kpc}^2/\mathrm{Myr}$ and predicted $E_{\mathrm{tot}} = -0.103 \pm 0.001\,\mathrm{kpc}^2/\mathrm{Myr}^2$. Using these results we look for globular clusters with similar E_{tot} and L_z properties that could have been the progenitor of the Jet stream. From

[4]This agrees with unpublished spectroscopic data from AAT/2dF (T. S. Li, private communication).

the Vasiliev (2019) catalog of globular cluster orbital properties we find no close matches suggesting that the progenitor of the Jet stream is either fully disrupted or undiscovered.

Comparing these results to Figures 1 and 2 in Bonaca et al. (2020), we find that the Jet stream is on a retrograde orbit with orbital parameters closest to Phelgethon ($L_z \sim 1.93\,\mathrm{kpc}^2/\,\mathrm{Myr}^2$, $E_{\mathrm{tot}} \sim -0.10\,\mathrm{kpc}^2/\,\mathrm{Myr}^2$) and nearby Wambelong and Ylgr as well. It seems likely that the progenitors of Phelgethon and Jet were accreted onto the Milky Way in the same accretion event. The work of Naidu et al. (2020) with the H3 survey identified a number of Milky Way accretion events, and localized them in the $E_{tot} - L_z$ paramter space. The $E_{tot} - L_z$ properties of the Jet stream places it in the region of parameter space likely associated with the Sequoia, I'itoi, and Arjuna progenitors (their Figure 2), suggesting that the progenitor of the Jet stream was a globular cluster associated with one of these accretion events (Naidu et al., 2020; Bonaca et al., 2020).

3.6 Conclusions

We have presented deep photometric and astrometric measurement of the Jet stream. We utilized the deep, wide-field, homogeneous DELVE DR1 data, which allowed us to discover substantial extensions of the Jet stream. We used both DELVE photometry and proper motions from *Gaia* EDR3 to select a sample of candidate BHB member stars. These stars allow us to resolve a distance gradient along the stream. The DELVE photometry is then used to model the stream intensity, track, and width, quantitatively characterizing the observed density variations. Additionally, we are able to use BHB and RGB stars to measure the systemic proper motion and proper motion gradient of Jet for the first time. Finally, we fit the stream with a dynamical model to constrain the orbit of the Jet stream.

The results of these analyses are summarized as follows:

- We extend the known extent of the Jet stream from 11° to $\sim$29° corresponding to a physical length of $\sim$16 kpc.
- We measure a distance gradient of -0.2 kpc/deg along the stream ranging from $D_\odot \sim$

34.2 kpc at $\phi_1 = -15°$ to $D_\odot \sim 27.4$ kpc at $\phi_1 = 13.7°$.

- We model the stream morphology to quantitatively characterize the stream track, width and linear density. We identify a gap in the stream and two features off the main track of the stream.

- We measure the proper motion of the Jet stream for the first time, and identify likely member RGB/BHB stars from their proper motions.

- Our modeling suggests Jet is on a retrograde orbit, unlikely to have been significantly affected by the LMC or Milky Way bar, and has an orbital pericenter of $r_{peri} = 12.7$ kpc.

Our analysis of the Jet stream has already been used to target spectroscopic measurements with AAT/2dF as part of the Southern Spectroscopic Stellar Stream Survey ($\mathcal{S}^5$; Li et al., 2018). Medium-resolution spectroscopic measurements with $\mathcal{S}^5$will confirm stream membership, provide radial velocities for stream members, and measure metallicities from the equivalent widths of the calcium triplet lines (Li et al., 2018). Such measurements have already yielded interesting dynamical information for the ATLAS stream (Li et al., 2020) and measured an extremely low metallicity for the Phoenix stream (Wan et al., 2020). These measurements will further allow the targeting of high-resolution spectroscopy, which can provide detailed elemental abundances for Jet member stars (Ji et al., 2020), and help to determine the nature of the Jet stream progenitor. The future of resolved stellar studies is bright with ongoing and future deep and wide-area photometric surveys. In particular, detailed studies of stellar streams will provide important information for modeling both the large and small-scale structure of the Milky Way halo, ultimately helping to constrain the fundamental nature of dark matter (Drlica-Wagner et al., 2019). In the near future, DELVE will significantly improve the extent and homogeneity of the southern sky coverage, setting the stage for the LSST-era. Our work on the Jet stream provides an important precursor to similar measurements that will be possible with LSST.

Facilities: Blanco, *Gaia*.

Software:`astropy` (Astropy Collaboration et al., 2013; Price-Whelan et al., 2018), `emcee` (Foreman-Mackey et al., 2013), `fitsio`,[5] `HEALPix` (Górski et al., 2005),[6] `healpy`,[7] `Matplotlib` (Hunter, 2007), `numpy` (Van Der Walt et al., 2011), `pandas` (pandas development team, 2020; Wes McKinney, 2010), `scipy` (Jones et al., 2001), `STAN` (Carpenter et al., 2017) `ugali` (Bechtol et al., 2015).[8]

[5] `https://github.com/esheldon/fitsio`
[6] `http://healpix.sourceforge.net`
[7] `https://github.com/healpy/healpy`
[8] `https://github.com/DarkEnergySurvey/ugali`

4. THE DEVELOPMENT AND TESTING OF TCal: A MOBILE SPECTROPHOTOMETRIC CALIBRATION UNIT FOR ASTRONOMICAL IMAGING SYSTEMS*

4.1 INTRODUCTION

In Astronomy, photometric surveys are one of the fundamental tools used to investigate the Universe. Recently, these surveys have become increasingly ambitious in their goals, and as a result increasingly reliant on precise calibrations of their data products. Projects such as the Sloan Digital Sky Survey (SDSS; York, 2000), Two Micron All Sky Survey (2MASS; Skrutskie, 2006), Pan-STARRS (Kaiser, 2002), the Dark Energy Survey(DES; DES Collaboration et al., 2016), and The Palomar Transient Factory (PTF; Law, 2009) have produced rich catalogs containing multi-color and/or multi-epoch data. These data can then be used to probe fundamental parameters of the Universe and investigate astrophysically interesting phenomena. The next generation of large astronomical projects includes the Legacy Survey of Space and Time(LSST; Ivezić, 2008) at the Vera Rubin Observatory (VRO), which will deeply image more than two thirds of the sky synoptically monitoring billions of stars and galaxies. To continue to benefit from previous surveys and to properly exploit the LSST catalog, it will be important to fuse new data with existing catalogs as well as to devote significant resources to LSST follow-up. This means that a greater importance must be placed on reducing systematic error when comparing results from multiple instruments, and that properly calibrating existing imaging systems will help increase the scientific yield of future projects.

* this chapter uses material the following SPIE conference proceedings: *Development of TCal: a mobile spectrophotometric calibration unit for astronomical imaging systems*, P. Ferguson; D. L. DePoy; L. Schmidt; J. L. Marshall; T. Prochaska; D. Freeman; L. Gardner; I. Gutierrez; D. Kim; Z. Kunnummal; M. Sauseda; H. Sharp; M. Torregosa, Proc. Volume 10702, Ground-based and Airborne Instrumentation for Astronomy VII; 107023A (2018) and *Further development and testing of TCal: a mobile spectrophotometric calibration unit for astronomical imaging system*, P. S. Ferguson, L. Barba, D. L. DePoy, L. M. Schmidt, J. L. Marshall, T. Prochaska, L. Bush, J. Mason, M. Sauseda, Proc. Volume 11447, Ground-based and Airborne Instrumentation for Astronomy VIII; 114475U (2020)

One specific example, using LSST imaging data to explore properties of supernovae to z $\sim$ 0.8 is among thousands of LSST science goals where data fusion plays a major role. Determining these supernovae properties is useful in many cosmological applications. In particular, supernovae luminosity distances can be used as a direct measure of the redshift-distance relation. This relation will be used to distinguish between a constant equation of state and a redshift-dependent one, independently constrain the value of w to $< 5\%$, and further explore the physics of Dark Energy (LSST Science Collaboration and Abell, 2009). But, LSST does not plan frequent filter changes, meaning that to take full advantage of LSST other observatories will have to devote significant resources to rapid follow-up to characterize the color and evolution of these transient events. LSST plans to have photometry that is stable and uniform over the sky to $< 1\%$ (< 0.01 mag). It is then obvious that follow-up efforts will also require extremely precise and accurate photometry (0.01 mag) when combined with LSST observations to enhance the scientific return of the survey.

Typically, the spectrophotometric throughput of astronomical imaging systems is not very well known. Filter transmission profiles, quantum efficiency versus wavelength for detectors, reflectivity of mirrors, and lens throughput are estimated from vendor-supplied information and multiplied together to form an estimate of the total system performance. This process is subject to many assumptions, critical measurement errors, and relatively large uncertainty. In order to robustly calibrate modern wide field imaging data, an in situ measurement of the response function of the complete imaging system must be made.

Our lab has previously deployed systems to make this measurement of the response function. We designed, built, and deployed DECal, a spectrophotometric calibration system for the u, g, r, i, z, Y filters used in the Dark Energy Camera (DECam) on the 4 m Blanco telescope at Cerro Tololo Inter-American Observatory (Rheault, 2010, 2012; Marshall, 2016). This permanent system has allowed us to monitor the response function of DECam both as a function of position on the focal plane and as a function of time. This constant monitoring and calibration of DECam has helped the Dark Energy Survey achieve $< 1\%$ errors

on its photometry (Li, 2016; Burke, 2018). Additionally, in the past we characterized the spectrophotometric properties of the imaging equipment used by the Carnegie Supernova Project. In particular we measured the throughput of the u, g, r, i, B, V, Y, J, H, and K_s filters used in the WIRC and RetroCam instruments at the Swope 1 m and du Pont 2.5 m telescopes at Las Campanas Observatory to an accuracy of $< 1\%$ (Rheault, 2014).

DECal and the system used at Las Campanas are similar in design. They use a monochromator-based light source to project narrow band ($\sim$ 1 nm) light onto a flat field screen. This signal is then measured by a photodiode with known response function and at the same time the instrument to be calibrated acquires an image. The ratio of the signal seen by the photodiode and the signal on the instrument detector is an in situ measurement of the instrumental throughput at that wavelength. This measurement is repeated at different wavelengths resulting in a defined response function over the desired spectral range. An example from previous work can be seen in Figure 4.1 which shows the relative throughput as a function of wavelength for the RetroCam instrument on the Swope telescope used in the Carnegie Supernova Project (Marshall, 2016).

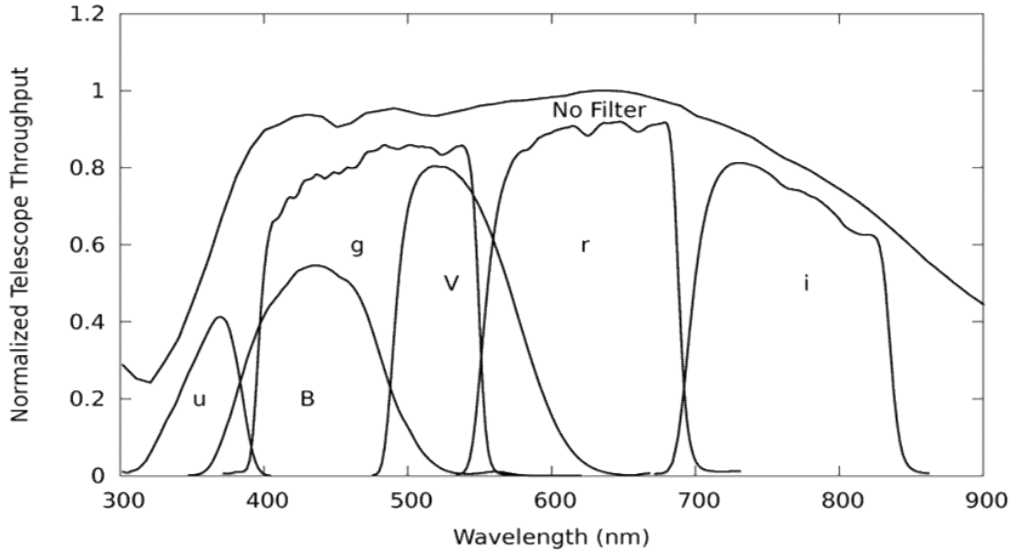

Figure 4.1 Scan of optical filters used in the Carnegie Supernova Project (Marshall, 2016). This is similar to the expected data product of TCal.

Building on this previous work, and in an effort to support the astronomical community in the age of LSST, we are developing TCal, a mobile spectrophotometric calibration system that will measure the throughput of the complete telescope plus instrument system as a function of wavelength. This system will be taken to multiple 1-8 m telescopes at observatories around the world that plan to spend significant time following up LSST or benefit from being photometrically calibratable to LSST data products. TCal will be used to characterize these systems' filter transmission functions from 300 nm $< \lambda <$ 1100 nm. This calibration will enable photometric measurements that are accurate to $< 1\%$ (< 0.01 mag), and generally reduce overall systematic errors.

The experimental setup of the TCal instrument is described in detail in Section 4.2. The software developed, measurement procedure, and data reduction pipeline are discussed in Section 4.3. In Section 4.4 we present the results of the initial deployment of our system at McDonald Observatory, and conclude with Section 4.5.

4.2 EXPERIMENTAL SETUP

A schematic of the TCal system is shown in Figure 4.2 and a detailed model/image are shown in 4.4. To summarize, the system consists of a broadband light source that passes through a filter wheel and into a monochromator. This monochromator is used to select a narrow bandwidth ($\sim$ 1-2 nm Full Width Half Maximum; FWHM), and the narrow-band light is fed into a fiber bundle; one of the fibers leads to a monitoring spectrometer, and the rest of the fibers send the light to a diffuser based projection system at the top of the telescope. The monitoring spectrometer gives real-time measurements of the projected bandpass to verify the width and central wavelength of the signal. The projection system uniformly illuminates a flat field screen mounted inside the telescope dome. A signal, from the flat field screen, is measured simultaneously by the system to be calibrated (Target CCD) and the TCal monitor charge coupled device (Monitor CCD). Then, the ratio of these two signals can be used to determine the instrumental transmission at a given wavelength. TCal is designed to measure the response function of imaging instruments over the spectral range

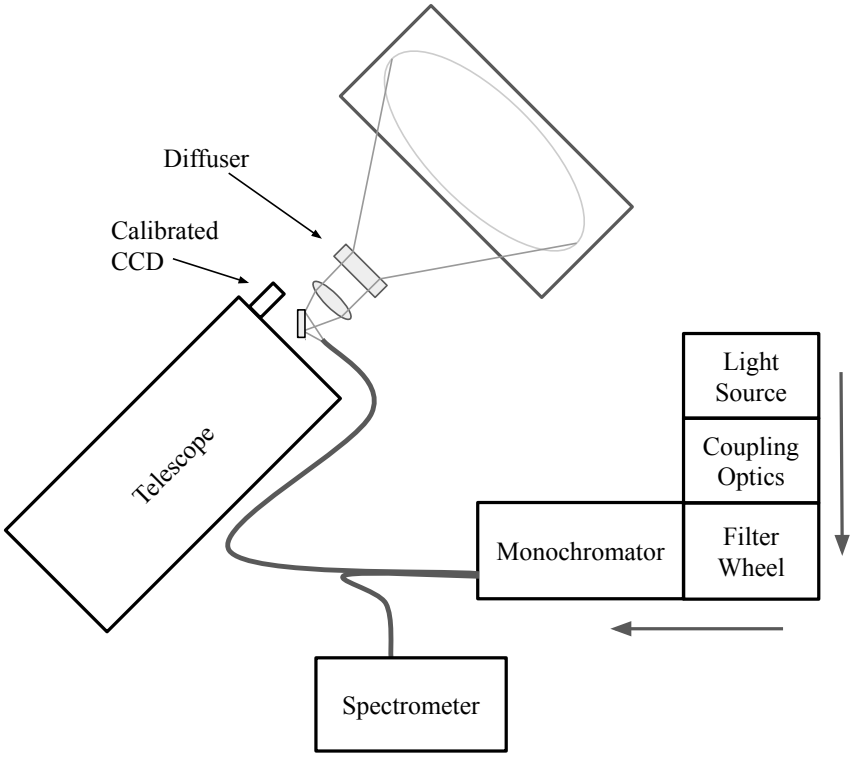

Figure 4.2 Schematic of the TCal system. The large arrows on the right hand side show the direction that light travels through these components of the system.

of 300 nm to 1100 nm. The following subsections (4.2.1-4.2.10) provide more detail on the components that make up TCal. Since many of the parts for TCal are re-purposed from previous systems we have developed, past papers provide a good resource for additional information (Rheault, 2010, 2012; Marshall, 2016; Rheault, 2014).

4.2.1 Light source

We use a commercial laser driven light source, the EQ-99x, manufactured by Energetiq. This source strongly emits from 170-1700 nm as seen in Figure 4.3. This emission entirely encompasses the spectral range we plan to calibrate. The laser driven light source is a particularly good option because of its high surface brightness and radiance that is roughly 10 times that of a traditional quartz lamp (as was used in our previous systems).

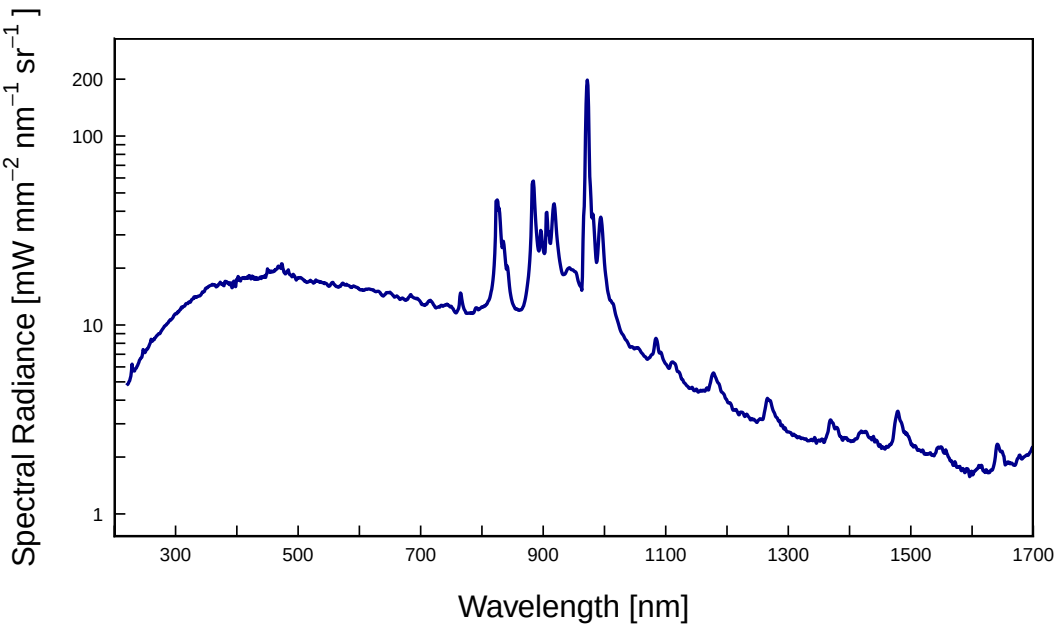

Figure 4.3 Spectral Radiance of EQ-99x as measured in the lab by Energetiq

4.2.2 Coupling Optics

Light from the light source is coupled to the monochromator via two off-axis parabolic (OAP) mirrors manufactured by Thorlabs. The assembly is mounted on a five axis stage to allow easy and repeatable alignment of the light source and the monochromator. Baffling in this enclosure reduces the levels of stray light. The exiting beam is $f/4$ and is fed directly into the monochromator. Figure 4.4 shows an engineering drawing of the setup coupling the light source to the monochromator.

4.2.3 Filter Wheel

We use a computer controlled filter wheel from ThorLabs, specifically the FW102. The filters are placed between the coupling optics and the monochromator as shown in figure 4.4. This allows us to easily change as a function of wavelength the broadband light signal that is fed into the monochromator. At blue wavelengths 350-445 nm we use short pass (SP) filters to remove out-of-band light that was scattering into the fiber as discussed in more detail

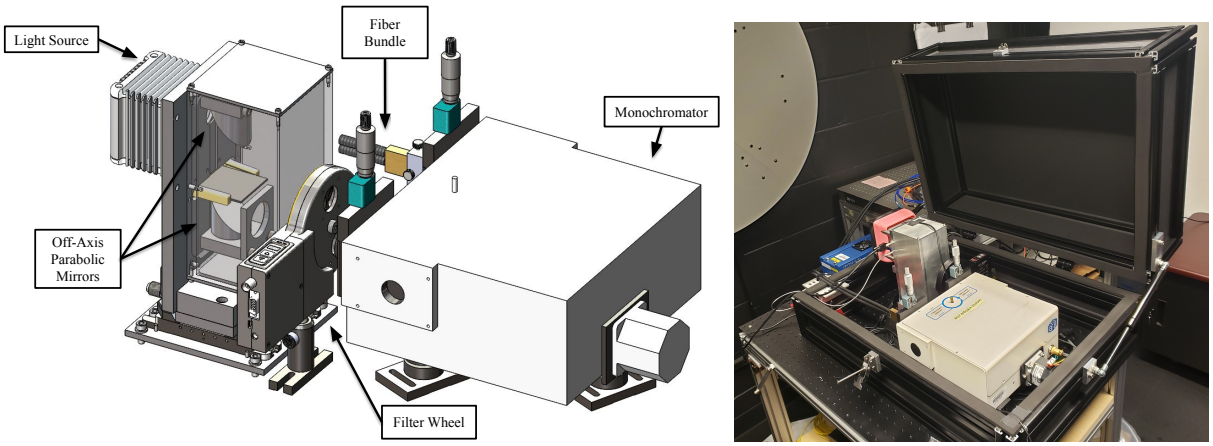

Figure 4.4 *Left:* A model of the light source, coupling optics, filter wheel and monochromator. *Right:* Image of the TCal system in the lab, including the enclosure and dedicated table.

in Section 4.4.1. At redder wavelengths we use long pass (LP) filters to block higher order diffractions. This removes bluer out of band light that would otherwise be injected into the fiber bundle. In total the filter wheel has 6 slots. We use 3 for SP filters (400, 425 and 450 nm) 2 for LP filters (500 and 550 nm) and leave one slot open. This setup allows us to create a pure narrowband signal ranging from 350-1100 nm.

4.2.4 Monochromator

We use an $f/4$ Czerny-Turner type monochromator (manufactured by Horiba iHR-320) with a 1200 g/mm grating. This setup gives a dispersion of 4.2 nm/mm which is large enough to create the desired $\sim$1 nm bandpass, and small enough to scan from 300-1100 nm without switching gratings. Additionally, the exit slit size can be increased to create a larger bandpass. This helps to reduce measurement time when conducting an out-of-bandpass scan to ensure the filters do not leak outside their desired spectral range. For these out-of-bandpass scans the fine wavelength information is not necessary, and a coarser mode can be used.

4.2.5 Fiber Bundle

A custom 9 m long fiber bundle assembled by Fibertech Optica is used. This is a broad spectrum fiber that transmits well both in the UV and IR. The bundle contains 10 fibers with 600 micron cores arranged in a line at the monochromator output. One of the fibers is split off and illuminates the monitoring spectrometer. The rest of the fibers are arranged in a circular output that feeds into the projection system mounted on the telescope.

4.2.6 Monitoring Spectrometer

To monitor in real time the spectral information of the signal projected onto the screen, we feed one of the fibers from the bundle into a spectrometer. This monitoring spectrometer records a spectrum for each exposure that is a direct measure of the central wavelength and FWHM of the light leaving the monochromator. We use a spectrometer with high enough resolution to characterize the central wavelength and FWHM with a precision of ~ 0.1 nm. Our spectrometer is calibrated using Mercury calibration lamps.

4.2.7 Projection System

As discussed in previous work by our team, while it is not required for the illumination of the flat field screen to be completely uniform, large scale gradients should be avoided to keep the focal plane evenly illuminated (Marshall and DePoy, 2013). To this end we use polymer-on-glass circular Engineered Diffusers (EDC) manufactured by RPC Photonics to project the light onto the flat field screen. Depending on the size of the telescope and the size/distance of the flat field screen, different diffusers with cones of light ranging from $2^\circ - 60^\circ$ can be used. This will ensure an even illumination of the screen for any of the telescopes we will calibrate.

4.2.8 Flat Field Screen

We conducted significant testing to find an appropriate portable screen material to be illuminated. A mixed nylon-spandex material from *stretchyscreens.com* was found to be both

relatively Lambertian, and highly reflective as seen in Figure 4.5. More information on this and other measured white materials can be found in Schmidt et al. (2018). This material is easily mounted on a frame and hung inside the dome to provide a highly reflective standard flat field screen. Figure 4.5 shows a photograph of a 1.2 m flat field screen mounted in a commercial frame (also provided by *stretchyscreens.com*).

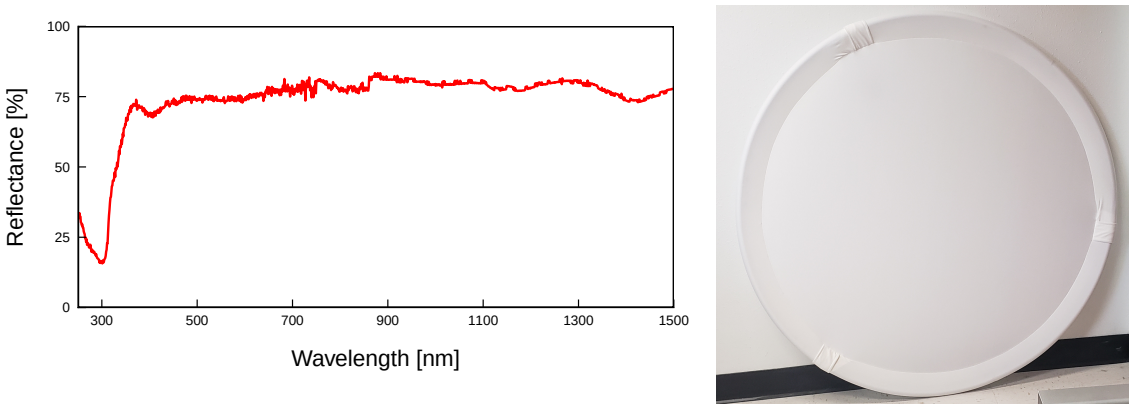

Figure 4.5 *Left*: Reflectance measurements for the mixed nylon-spandex material from Schmidt *et al. in prep*,Schmidt (2018) note that it reflects well into the UV unlike other screen materials tested. Right: Image of 1.2 m screen.

4.2.9 Monitor CCD

For TCal we use the commercially available STF-8300M CCD from SBIG as a calibrated monitoring device to measure the signal reflected off of the screen. This CCD will be mounted on the telescope and baffled using an adjustable aperture; to only be a measure of the light reflected from the screen and not saturate during the course of a scan. We chose to use a CCD system unlike our previous system DECal, which use a NIST-calibrated photodiode. This choice was made because of how easily a CCD based system integrates with TCal and the flexibility it gives us when setting up TCal in many different configurations. The system functions well over our desired spectral range (350-1100 nm), and has pre-written drivers that are easy to integrate with our custom LabVIEW software. We have found it to be quite

stable over a single scan due to the built-in cooling system. Additionally, our ability during reduction and processing to only include pixels that measure signal allows us to easily and quickly setup and optimize the system for any desired deployment. The monitor CCD has been calibrated using a NIST calibrated photodiode in the lab. This calibration was done by running 15 spectral scans (using the methodology described in Section 4.3.2) with the photodiode acting as a monitor and the STF-8300M as the system to be calibrated. Then, the median value at each wavelength of these scans is used as the relative response function of the CCD.

4.2.10 Instrument Enclosure/Stand

Due to the mobile nature of TCal we designed a compact and collapsible enclosure/stand for this system. The enclosure, a black box, is shown on the right side of Figure 4.4. This baffles the system and ensures that there is no stray light introduced from TCal during a scan. Since there is no longer good air circulation, we have also implemented an active cooling system for the laser driven light source consisting of the pink shroud and fan seen in figure 4.4. Both TCal and the enclosure are mounted on an aluminum breadboad that allows for easy setup and alignment of the system. A collapsible item rail based stand supports the breadboard. The lower shelf of the stand compactly holds a computer, the monitoring spectrometer, the control system for the monochromator, and various cables. Plastic panels are used to baffle the lower shelf further reducing scattered light. This compact infrastructure contributes to the flexibility of TCal allowing us to quickly and robustly set up the system in a wide range of situations.

4.3 SOFTWARE

This section discusses in detail the software we have developed to run a scan and the data reduction pipeline we have developed to process a scan once the data has been taken. The scan software is mainly written in LabVIEW and communicates with the TCal system as well as the control system of the imager to be calibrated (target CCD). The scan software

and reduction pipeline have been designed to be user-friendly letting one individual easily and remotely run a scan with minimal effort. Additionally we have made the software with an eye towards flexibility, so it can be easily adjusted to integrate a range of imaging systems.

4.3.1 Scan Software

Below we outline the steps taken when making measurements with TCal. The graphical user interface for a TCal scan is shown in figure 4.6. This interface is used to setup a scan and monitor the current progress of a scan. The left hand panel is used to set up and configure a scan, whereas the right hand region shows the overall progress and progress in an individual step.

The target and monitor data are acquired simultaneously to prevent any minor fluctuations in the lamp brightness from introducing systematic error into the throughput measurement. Additionally, dark images are taken between each observation so that gradual changes in scattered light or background illumination do not bias the measurement. After measurements have been made, the data reduction pipeline concatenates measurements of the Target CCD signal, Monitor CCD signal, central wavelength, measured FWHM, and our final measurement, the transmission of the imager to be calibrated as a function of wavelength.

4.3.1.1 Scan Initialization

Prior to the start of a scan the following parameters are set:

- File location
- Scan name
- Beginning and ending wavelengths
- Step size
- Monitoring spectrometer integration time

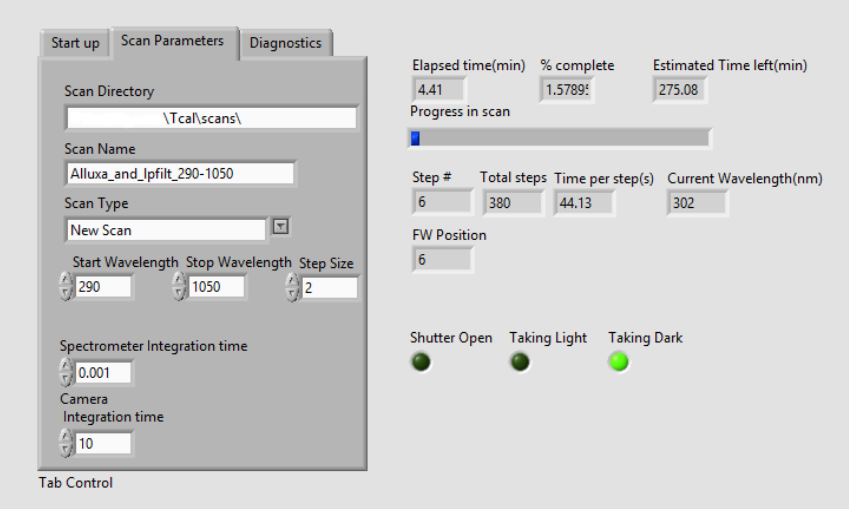

Figure 4.6 Graphical Control for TCal scan written in LabView.

- Monitor CCD integration time

The monitor CCD integration time can also be set to depend on wavelength but is set to be the same as the target CCD integration time.

4.3.2 Scan Procedure

During a scan our LabVIEW code controls all of the elements of TCal the steps taken are listed below.

1. Close light source shutter
2. Check current wavelength and ensure proper filter is in place.
3. Dark image:
   (a) Take target CCD image that will be used to remove background light
   (b) Expose monitor CCD for the duration of target CCD exposure
4. Open light source shutter
5. Light image:

(a) Take target CCD image

(b) Expose monitor CCD for the duration of target CCD exposure

6. Re-shutter light source

7. Move monochromator to next position, usually 1-2 nm higher

8. Repeat steps 2-7 until scan is complete

4.3.3 Data Reduction Pipeline

Once a scan has been completed, the extraction of the transmission of the target system as a function of wavelength is performed in the following manner. At the beginning of each deployment of TCal, we identify the pixels on the Target CCD that are illuminated. Only these pixels are considered as part of the signal to reduce overall noise. Then for each step of the scan, the monitor spectrometer is used to define the true central wavelength and bandpass width. The light images from the Monitor and Target systems are dark-subtracted using the average of the dark images taken before and after each light image. For the Monitor CCD, the previously identified illuminated pixels are summed and corrected for wavelength sensitivity, amplifier gain, and temperature. This gives a measurement of the number of photons seen by the Monitor CCD over the integration time. Then each of the Target systems pixels are divided by the Monitor signal giving the relative throughput of the system at that wavelength. In general, to increase the signal to noise of the measurement we bin the signal from the pixels of the Target CCD. This is done by splitting the Target CCD into regions and summing the pixels within a region. This binning is flexible and can be customized for each deployment of TCal. This procedure is repeated for every step in the scan resulting in a characterized transmission function such as the one discussed in Section 4.4 and shown in Figure 4.7.

4.4 TESTING OF PROTOTYPE

To test the TCal system we took a prototype version to McDonald Observatory during the summer of 2019. During this period, a protoype version of the Exoplanet Transmission Spectroscopy Imager (ETSI) was mounted on the 0.9 m telescope. A detailed description of the ETSI instrument can be found in (Limbach et al., 2020). Briefly summarizing, this instrument used a SBIG STF-8300M CCD, a Chroma 435 nm LP filter and and Alluxa ULTRA series quad-bandpass filter (`https://www.alluxa.com/`). The Alluxa filter bandpasses had central wavelength of 431, 509.5, 592 and 681 nm and FWHM of 30, 16, 30, 38 nm respectively. The dashed line in Figure 4.7 shows the expected relative transmission of the SBIG CCD $\times$ Alluxa Quad filter $\times$ Chroma LP filter convolved with a Gaussian the same size as our scan bandpass (FWHM=5 nm). The theoretical bandpasses of the two filters are provided online by their vendors.

The goal of this test was to ensure TCal could precisely measure the transmission function of an imaging instrument and that TCal could easily be configured in a remote environment. We setup TCal and ran two scans of the ETSI instrument. The spectral range of these scans was from 400-750 nm. We used a 1.2 mm slit on the monochromator output resulting in an output bandpass FWHM of 5 nm. We did not split the ETSI detector into regions, but rather summed the signal over the entire detector. Figure 4.7 shows the results of these scans; a measured relative throughput of the prototype ETSI instrument. The blue line shows the average of two TCal scans.

The error on this measurement can be broken down into a few components. The systematic uncertainty on the Monitor CCD is estimated to be 1%. The relative noise level of both the Monitor CCD and the ETSI CCD measurements was found to be 0.03%. This when added in quadrature gives a total uncertainty of 1%. Due to the precision of the monitoring spectrometer, we find the uncertainty on the central wavelength of the projected bandpass to be 0.1 nm.

Overall this test was successful; we were able to quickly and easily deploy TCal in a remote

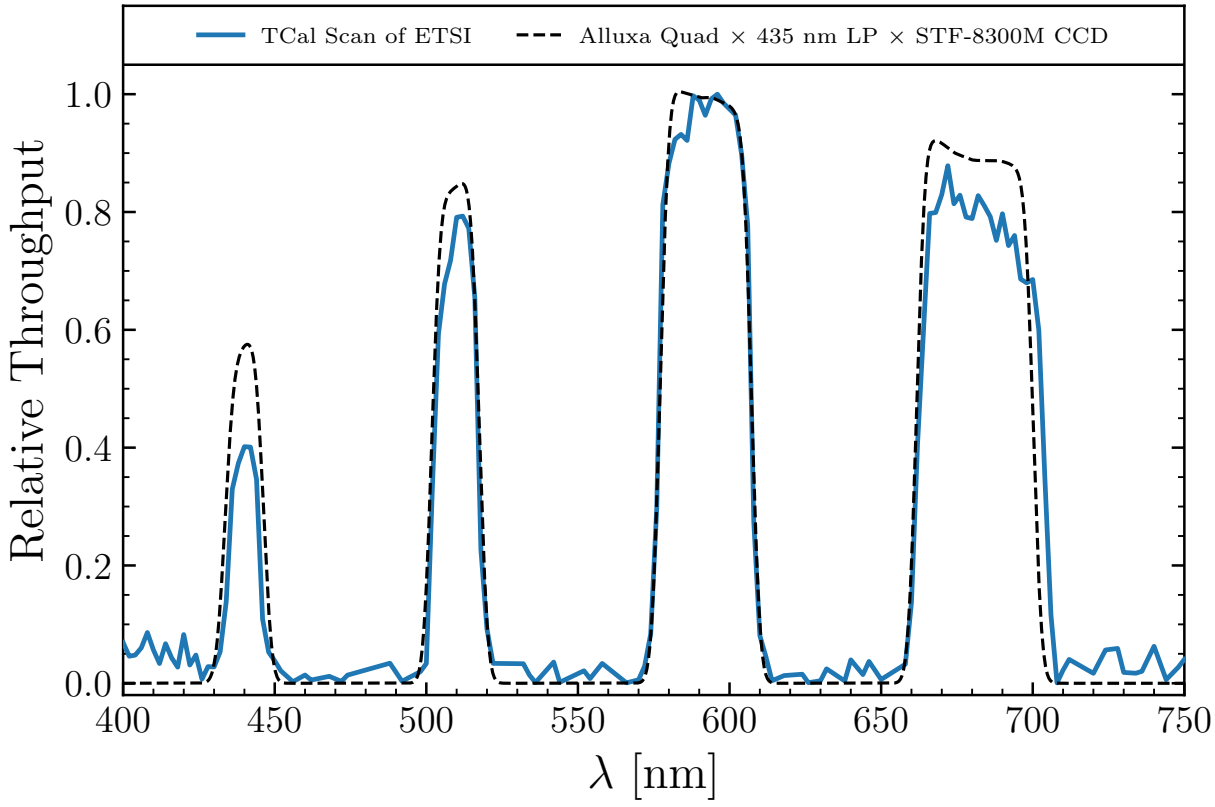

Figure 4.7 The results of our scan of ETSI mounted on the 0.9 m telescope at McDonald Observatory. The blue line shows our measurement the relative transmission as a function of wavelength for ETSI. The dashed line is a prediction of the bandpass solely taking into account the theoretical transmission functions of the Alluxa Quad filter and 435 nm long pass (LP) filter and our lab measured transmission function of the STF-8300M CCD.

environment. The results of the scan (blue line) show the cut-on and cut-off wavelengths and general shape of the relative transmission function largely agrees with the expected transmission (black dashed line). The measured signal at wavelengths less than 430 nm is discussed in the next subsection. The other differences seen between the prediction and measurement showcase the importance of this calibration.

4.4.1 Stray Light At Blue Wavelengths

At blue wavelengths (< 430 nm) it can be seen that we detected a small but significant signal although there is predicted to be no transmission from both the 435 nm LP and

Alluxa filters at these wavelengths. Taking spectra in the lab through both filters confirms this. What we did find was that light redward of the desired bandpass was being scattered onto the exit slit of the monochromator. This scattered light component appeared to have a wavelength of 440 nm. This component was strongest when the monochromator was set to $\sim$ 390 nm but appeared to mainly affect the range from 370-420 nm.

A number of approaches were taken to address this scattered light component. First, we tried to increase the baffling inside the monochromator as much as possible, but the light appeared to be a spatially diffuse signal mainly on the optical axis of our $f/4$ Czerny-Turner type monochromator. So, baffling was unable to address the issue. We tried 3D printing a mask for the diffraction grating to remove doubly diffracted on-axis stray light as discussed by other authors.Penchina (1967); Mitteldorf and Landon (1968) Again this failed to removed the stray light component. The solution that we settled on was to use multiple short pass filters to prevent the red light from entering the monochromator when scanning the affected spectral region. For wavelengths blueward of 390 nm, we use a 400 nm SP filter. From 390-415 nm a 425 nm SP filter is used, and from 415-440 nm a 450 nm SP filter is used. From extensive in-lab testing this appears to have removed the out-of-band signal.

4.5 CONCLUSION

We have fully developed and tested a traveling spectrophotometric system, TCal. This system builds on previous systems developed by our lab but is more compact and easily deployable. We discuss the recent hardware developments, consisting of a filter wheel, calibrated Monitor CCD, and instrument enclosure. Next, a newly developed scan software and data reduction pipeline are explained. Finally, we describe our successful testing of a prototype version of TCal at McDonald Observatory. TCal can be used to measure system transmission as a function of wavelength and location on the focal plane with $\sim$ 1% precision. In the next 1-2 years we plan to calibrate various 1-8 m telescopes that expect to see significant scientific benefits from this calibration. This will serve to enhance the scientific return of LSST follow-up, benefiting the astronomical community as a whole.

Facility: McDonald Observatory.

Software:`astropy` (Astropy Collaboration et al., 2013; Price-Whelan et al., 2018), `Matplotlib` (Hunter, 2007), `numpy` (Van Der Walt et al., 2011), `pandas` (pandas development team, 2020; Wes McKinney, 2010), `scipy` (Jones et al., 2001).

5. SUMMARY AND CONCLUSIONS

In this dissertation, we have presented works focused on either using large scale surveys to better understand the nature of substructure in the Milky Way halo or instrumentation geared towards improving the scientific return of large scale surveys. This adds to the body of work characterizing the Milky Way halo, which helps to better understand the structure and evolution of the Milky Way, probe environments in the early universe, and place constraints on the nature of dark matter.

In Chapter 2, we used RR Lyrae stars from the OGLE and *Gaia* DR2 surveys and developed a modeling framework to constrain the three dimensional shape of the Sagittarius dSph core. We found the shape of the core to be highly triaxial, and unlikely to be well represented by an axisymmetric model, one commonly used to describe the kinematics of galaxies. These constraints on the three dimensional structure of this dwarf galaxy will help to better model the kinematics within the core. In particular, if radial velocities are obtained for the sample of OGLE stars with precise three-dimensional positions, we will be able to determine if the core of this satellite is in equilibrium and possibly determine exactly how anisotropically the mass is distributed in this galaxy. This dataset, if created, will be the best six-dimensional dataset in a dwarf galaxy due to the size of Sagittarius and its proximity to the Earth.

In Chapter 3, we use the photometry from the DELVE survey and proper motions from the *Gaia* EDR3 survey to characterize the nature of the Jet stellar stream. We measure the extent, distance gradient and proper motion of the stream. Then, we use these observations to infer the orbit of the stream, finding it is on a retrograde orbit with a current Galactocentric radius of ~ 30 kpc and a pericenter of $r_{peri} \sim 13$ kpc. These characteristics, a retrograde orbit and large pericenter, indicate that density variations in Jet stream will likely provide some of the strongest constraints on the low mass dark matter subhalo mass function. To this end, we modeled the matched-filter photometry of the Jet stream to quan-

titatively characterize density variations enabling future studies to turn these measurements into constraints.

Finally, in Chapter 4 we discuss the development of TCal, a mobile spectrophotometric calibration device that will help to enhance the scientific return of large scale imaging surveys. We have designed, built, tested this calibration system, and presented some results from observations taken at McDonald observatory of the ETSI instrument (Limbach et al., 2020). In the near future TCal will be taken to various 1-8 m telescopes around the world that expect to devote significant time to survey follow-up. We plan to measure the instrumental response function of these instruments at the 1-2 % level which will reduce systematic error associated with fusion of data products and help to enable precision survey science over the coming decade.

REFERENCES

Abbott, T. M. C., Abdalla, F. B., Alarcon, A., Aleksić, J., Allam, S., Allen, S., Amara, A., Annis, J., Asorey, J., Avila, S., and et al. (2018). Dark Energy Survey year 1 results: Cosmological constraints from galaxy clustering and weak lensing. *Phys. Rev. D*, 98(4):043526.

Aihara, H., AlSayyad, Y., Ando, M., Armstrong, R., Bosch, J., Egami, E., Furusawa, H., Furusawa, J., Goulding, A., Harikane, Y., Hikage, C., Ho, P. T. P., Hsieh, B.-C., Huang, S., Ikeda, H., Imanishi, M., Ito, K., Iwata, I., Jaelani, A. T., Kakuma, R., Kawana, K., Kikuta, S., Kobayashi, U., Koike, M., Komiyama, Y., Li, X., Liang, Y., Lin, Y.-T., Luo, W., Lupton, R., Lust, N. B., MacArthur, L. A., Matsuoka, Y., Mineo, S., Miyatake, H., Miyazaki, S., More, S., Murata, R., Namiki, S. V., Nishizawa, A. J., Oguri, M., Okabe, N., Okamoto, S., Okura, Y., Ono, Y., Onodera, M., Onoue, M., Osato, K., Ouchi, M., Shibuya, T., Strauss, M. A., Sugiyama, N., Suto, Y., Takada, M., Takagi, Y., Takata, T., Takita, S., Tanaka, M., Terai, T., Toba, Y., Uchiyama, H., Utsumi, Y., Wang, S.-Y., Wang, W., and Yamada, Y. (2019). Second data release of the Hyper Suprime-Cam Subaru Strategic Program. **??***jnlPASJ*, 71(6):114.

Amorisco, N. C., Gómez, F. A., Vegetti, S., and White, S. D. M. (2016). Gaps in globular cluster streams: giant molecular clouds can cause them too. *MNRAS*, 463(1):L17–L21.

Astropy Collaboration, Robitaille, T. P., Tollerud, E. J., Greenfield, P., Droettboom, M., Bray, E., Aldcroft, T., Davis, M., Ginsburg, A., Price-Whelan, A. M., Kerzendorf, W. E., Conley, A., Crighton, N., Barbary, K., Muna, D., Ferguson, H., Grollier, F., Parikh, M. M., Nair, P. H., Unther, H. M., Deil, C., Woillez, J., Conseil, S., Kramer, R., Turner, J. E. H., Singer, L., Fox, R., Weaver, B. A., Zabalza, V., Edwards, Z. I., Azalee Bostroem, K., Burke, D. J., Casey, A. R., Crawford, S. M., Dencheva, N., Ely, J., Jenness, T., Labrie, K., Lim, P. L., Pierfederici, F., Pontzen, A., Ptak, A., Refsdal, B., Servillat, M., and Streicher, O. (2013). Astropy: A community Python package for astronomy. *A&A*,

558:A33.

Balbinot, E., Yanny, B., Li, T. S., Santiago, B., Marshall, J. L., et al. (2016). The Phoenix Stream: A Cold Stream in the Southern Hemisphere. *ApJ*, 820(1):58.

Banik, N., Bovy, J., Bertone, G., Erkal, D., and de Boer, T. J. L. (2019). Novel constraints on the particle nature of dark matter from stellar streams. *arXiv e-prints*, page arXiv:1911.02663.

Banik, N., Bovy, J., Bertone, G., Erkal, D., and de Boer, T. J. L. (2021). Evidence of a population of dark subhaloes from Gaia and Pan-STARRS observations of the GD-1 stream. *MNRAS*, 502(2):2364–2380.

Barber, C., Starkenburg, E., Navarro, J. F., and McConnachie, A. W. (2015). Galactic tides and the shape and orientation of dwarf galaxy satellites. *MNRAS*, 447(2):1112–1125.

Battaglia, G., Helmi, A., and Breddels, M. (2013). Internal kinematics and dynamical models of dwarf spheroidal galaxies around the Milky Way. *New Astron. Rev.*, 57(3-4):52–79.

Bechtol, K., Drlica-Wagner, A., Balbinot, E., Pieres, A., Simon, J. D., Yanny, B., Santiago, B., Wechsler, R. H., Frieman, J., Walker, A. R., Williams, P., Rozo, E., Rykoff, E. S., Queiroz, A., Luque, E., Benoit-Lévy, A., Tucker, D., Sevilla, I., Gruendl, R. A., da Costa, L. N., Fausti Neto, A., Maia, M. A. G., Abbott, T., Allam, S., Armstrong, R., Bauer, A. H., Bernstein, G. M., Bernstein, R. A., Bertin, E., Brooks, D., Buckley-Geer, E., Burke, D. L., Carnero Rosell, A., Castander, F. J., Covarrubias, R., D'Andrea, C. B., DePoy, D. L., Desai, S., Diehl, H. T., Eifler, T. F., Estrada, J., Evrard, A. E., Fernandez, E., Finley, D. A., Flaugher, B., Gaztanaga, E., Gerdes, D., Girardi, L., Gladders, M., Gruen, D., Gutierrez, G., Hao, J., Honscheid, K., Jain, B., James, D., Kent, S., Kron, R., Kuehn, K., Kuropatkin, N., Lahav, O., Li, T. S., Lin, H., Makler, M., March, M., Marshall, J., Martini, P., Merritt, K. W., Miller, C., Miquel, R., Mohr, J., Neilsen, E., Nichol, R., Nord, B., Ogando, R., Peoples, J., Petravick, D., Plazas, A. A., Romer, A. K., Roodman, A., Sako, M., Sanchez, E., Scarpine, V., Schubnell, M., Smith, R. C., Soares-Santos, M., Sobreira, F., Suchyta, E., Swanson, M. E. C., Tarle, G., Thaler, J., Thomas, D.,

Wester, W., Zuntz, J., and DES Collaboration (2015). Eight New Milky Way Companions Discovered in First-year Dark Energy Survey Data. *ApJ*, 807(1):50.

Belokurov, V. and Koposov, S. E. (2016). Stellar streams around the Magellanic Clouds. *MNRAS*, 456(1):602–616.

Belokurov, V., Koposov, S. E., Evans, N. W., Peñarrubia, J., Irwin, M. J., Smith, M. C., Lewis, G. F., Gieles, M., Wilkinson, M. I., and Gilmore, G. (2014). Precession of the Sagittarius stream. *MNRAS*, 437(1):116–131.

Belokurov, V., Zucker, D. B., Evans, N. W., Gilmore, G., Vidrih, S., Bramich, D. M., Newberg, H. J., Wyse, R. F. G., Irwin, M. J., Fellhauer, M., Hewett, P. C., Walton, N. A., Wilkinson, M. I., Cole, N., Yanny, B., Rockosi, C. M., Beers, T. C., Bell, E. F., Brinkmann, J., Ivezić, Ž., and Lupton, R. (2006). The Field of Streams: Sagittarius and Its Siblings. *ApJ*, 642(2):L137–L140.

Belokurov, V., Zucker, D. B., Evans, N. W., Kleyna, J. T., Koposov, S., Hodgkin, S. T., Irwin, M. J., Gilmore, G., Wilkinson, M. I., Fellhauer, M., Bramich, D. M., Hewett, P. C., Vidrih, S., De Jong, J. T. A., Smith, J. A., Rix, H. W., Bell, E. F., Wyse, R. F. G., Newberg, H. J., Mayeur, P. A., Yanny, B., Rockosi, C. M., Gnedin, O. Y., Schneider, D. P., Beers, T. C., Barentine, J. C., Brewington, H., Brinkmann, J., Harvanek, M., Kleinman, S. J., Krzesinski, J., Long, D., Nitta, A., and Snedden, S. A. (2007). Cats and Dogs, Hair and a Hero: A Quintet of New Milky Way Companions. *ApJ*, 654(2):897–906.

Bernstein, G. M., Abbott, T. M. C., Armstrong, R., Burke, D. L., Diehl, H. T., Gruendl, R. A., Johnson, M. D., Li, T. S., Rykoff, E. S., Walker, A. R., Wester, W., and Yanny, B. (2018). Photometric Characterization of the Dark Energy Camera. **??***jnlPASP*, 130(987):054501.

Bertin, E. (2006). Automatic Astrometric and Photometric Calibration with SCAMP. In Gabriel, C., Arviset, C., Ponz, D., and Enrique, S., editors, *Astronomical Data Analysis Software and Systems XV*, volume 351 of *Astronomical Society of the Pacific Conference Series*, page 112.

Bertin, E. (2011). Automated morphometry with sextractor and psfex. In Evans, I. N., Accomazzi, A., Mink, D. J., and Rots, A. H., editors, *Astronomical Data Analysis Software and Systems XX*, volume 442 of *Astronomical Society of the Pacific Conference Series*, page 435, San Francisco, CA.

Bertin, E. and Arnouts, S. (1996). SExtractor: Software for source extraction. **??***jnlA&AS*, 117:393–404.

Bonaca, A. and Hogg, D. W. (2018). The Information Content in Cold Stellar Streams. *ApJ*, 867(2):101.

Bonaca, A., Hogg, D. W., Price-Whelan, A. M., and Conroy, C. (2019). The Spur and the Gap in GD-1: Dynamical Evidence for a Dark Substructure in the Milky Way Halo. *ApJ*, 880(1):38.

Bonaca, A., Naidu, R. P., Conroy, C., Caldwell, N., Cargile, P. A., Han, J. J., Johnson, B. D., Kruijssen, J. M. D., Myeong, G. C., Speagle, J., Ting, Y.-S., and Zaritsky, D. (2020). Orbital Clustering Identifies the Origins of Galactic Stellar Streams. *arXiv e-prints*, page arXiv:2012.09171.

Bovy, J. (2014). Dynamical Modeling of Tidal Streams. *ApJ*, 795(1):95.

Bovy, J., Allende Prieto, C., Beers, T. C., Bizyaev, D., da Costa, L. N., Cunha, K., Ebelke, G. L., Eisenstein, D. J., Frinchaboy, P. M., García Pérez, A. E., Girardi, L., Hearty, F. R., Hogg, D. W., Holtzman, J., Maia, M. A. G., Majewski, S. R., Malanushenko, E., Malanushenko, V., Mészáros, S., Nidever, D. L., O'Connell, R. W., O'Donnell, C., Oravetz, A., Pan, K., Rocha-Pinto, H. J., Schiavon, R. P., Schneider, D. P., Schultheis, M., Skrutskie, M., Smith, V. V., Weinberg, D. H., Wilson, J. C., and Zasowski, G. (2012a). The Milky Way's Circular-velocity Curve between 4 and 14 kpc from APOGEE data. *ApJ*, 759(2):131.

Bovy, J., Bahmanyar, A., Fritz, T. K., and Kallivayalil, N. (2016). The Shape of the Inner Milky Way Halo from Observations of the Pal 5 and GD–1 Stellar Streams. *ApJ*, 833(1):31.

Bovy, J., Rix, H.-W., Liu, C., Hogg, D. W., Beers, T. C., and Lee, Y. S. (2012b). The Spatial

Structure of Mono-abundance Sub-populations of the Milky Way Disk. *ApJ*, 753(2):148.

Bowden, A., Belokurov, V., and Evans, N. W. (2015). Dipping our toes in the water: first models of GD-1 as a stream. *MNRAS*, 449(2):1391–1400.

Braga, V. F., Dall'Ora, M., Bono, G., Stetson, P. B., Ferraro, I., Iannicola, G., Marengo, M., Neeley, J., Persson, S. E., and Buonanno, R. (2015). On the Distance of the Globular Cluster M4 (NGC 6121) Using RR Lyrae Stars. I. Optical and Near-infrared Period-Luminosity and Period-Wesenheit Relations. *ApJ*, 799(2):165.

Buchner, J., Georgakakis, A., Nandra, K., Hsu, L., Rangel, C., Brightman, M., Merloni, A., Salvato, M., Donley, J., and Kocevski, D. (2014). X-ray spectral modelling of the AGN obscuring region in the CDFS: Bayesian model selection and catalogue. *A&A*, 564:A125.

Bullock, J. S. and Boylan-Kolchin, M. (2017). Small-Scale Challenges to the ΛCDM Paradigm. **??***jnlARA&A*, 55(1):343–387.

Burke, D. L., *et al.* (2018). Forward Global Photometric Calibration of the Dark Energy Survey. *ApJ*, 155:41.

Caldwell, N., Bonaca, A., Price-Whelan, A. M., Sesar, B., and Walker, M. G. (2020). A Larger Extent for the Ophiuchus Stream. *AJ*, 159(6):287.

Carlberg, R. G. (2013). The Dynamics of Star Stream Gaps. *ApJ*, 775(2):90.

Carpenter, B., Gelman, A., Hoffman, M. D., Lee, D., Goodrich, B., Betancourt, M., Brubaker, M., Guo, J., Li, P., and Riddell, A. (2017). Stan: A probabilistic programming language. *Journal of Statistical Software, Articles*, 76(1):1–32.

Carretta, E., Bragaglia, A., Gratton, R., D'Orazi, V., and Lucatello, S. (2009). Intrinsic iron spread and a new metallicity scale for globular clusters. *A&A*, 508(2):695–706.

Cerny, W., Pace, A. B., Drlica-Wagner, A., Ferguson, P. S., Mau, S., Adamów, M., Carlin, J. L., Choi, Y., Erkal, D., Johnson, L. C., Li, T. S., Martínez-Vázquez, C. E., Mutlu-Pakdil, B., Nidever, D. L., Olsen, K. A. G., Pieres, A., Simon, J. D., Tollerud, E. J., Vivas, A. K., James, D. J., Kuropatkin, N., Majewski, S., Martínez-Delgado, D., Massana, P., Miller, A., Noël, N. E. D., Riley, A. H., Sand, D. J., Santana-Silva, L., Stringfellow,

G. S., Neilsen, E. H., and Tucker, D. L. (2021). Discovery of an Ultra-Faint Stellar System near the Magellanic Clouds with the DECam Local Volume Exploration (DELVE) Survey. *arXiv e-prints*, page arXiv:2009.08550.

Chabrier, G. (2001). The Galactic Disk Mass Budget. I. Stellar Mass Function and Density. *ApJ*, 554:1274–1281.

Chambers, K. C., Magnier, E. A., Metcalfe, N., Flewelling, H. A., Huber, M. E., Waters, C. Z., Denneau, L., Draper, P. W., Farrow, D., Finkbeiner, D. P., Holmberg, C., Koppenhoefer, J., Price, P. A., Saglia, R. P., Schlafly, E. F., Smartt, S. J., Sweeney, W., Wainscoat, R. J., Burgett, W. S., Grav, T., Heasley, J. N., Hodapp, K. W., Jedicke, R., Kaiser, N., Kudritzki, R.-P., Luppino, G. A., Lupton, R. H., Monet, D. G., Morgan, J. S., Onaka, P. M., Stubbs, C. W., Tonry, J. L., Banados, E., Bell, E. F., Bender, R., Bernard, E. J., Botticella, M. T., Casertano, S., Chastel, S., Chen, W.-P., Chen, X., Cole, S., Deacon, N., Frenk, C., Fitzsimmons, A., Gezari, S., Goessl, C., Goggia, T., Goldman, B., Grebel, E. K., Hambly, N. C., Hasinger, G., Heavens, A. F., Heckman, T. M., Henderson, R., Henning, T., Holman, M., Hopp, U., Ip, W.-H., Isani, S., Keyes, C. D., Koekemoer, A., Kotak, R., Long, K. S., Lucey, J. R., Liu, M., Martin, N. F., McLean, B., Morganson, E., Murphy, D. N. A., Nieto-Santisteban, M. A., Norberg, P., Peacock, J. A., Pier, E. A., Postman, M., Primak, N., Rae, C., Rest, A., Riess, A., Riffeser, A., Rix, H. W., Roser, S., Schilbach, E., Schultz, A. S. B., Scolnic, D., Szalay, A., Seitz, S., Shiao, B., Small, E., Smith, K. W., Soderblom, D., Taylor, A. N., Thakar, A. R., Thiel, J., Thilker, D., Urata, Y., Valenti, J., Walter, F., Watters, S. P., Werner, S., White, R., Wood-Vasey, W. M., and Wyse, R. (2016). The Pan-STARRS1 Surveys. *ArXiv e-prints*.

Clementini, G., Ripepi, V., Molinaro, R., Garofalo, A., Muraveva, T., Rimoldini, L., Guy, L. P., Jevardat de Fombelle, G., Nienartowicz, K., and Marchal, O. (2019). Gaia Data Release 2. Specific characterisation and validation of all-sky Cepheids and RR Lyrae stars. *A&A*, 622:A60.

Conroy, C., Bonaca, A., Cargile, P., Johnson, B. D., Caldwell, N., Naidu, R. P., Zaritsky, D.,

Fabricant, D., Moran, S., Rhee, J., Szentgyorgyi, A., Berlind, P., Calkins, M. L., Kattner, S., and Ly, C. (2019). Mapping the Stellar Halo with the H3 Spectroscopic Survey. *ApJ*, 883(1):107.

Cullinane, L. R., Mackey, A. D., Da Costa, G. S., Koposov, S. E., Belokurov, V., Erkal, D., Koch, A., Kunder, A., and Nataf, D. M. (2020). The Magellanic Edges Survey I: Description and first results. *MNRAS*, 497(3):3055–3075.

de Boer, T. J. L., Erkal, D., and Gieles, M. (2020). A closer look at the spur, blob, wiggle, and gaps in GD-1. *MNRAS*, 494(4):5315–5332.

Deason, A. J., Belokurov, V., and Evans, N. W. (2011). The Milky Way stellar halo out to 40 kpc: squashed, broken but smooth. *MNRAS*, 416(4):2903–2915.

Deb, S. (2017). Distance, reddening and three dimensional structure of the SMC - I: Using RRab stars. *arXiv e-prints*, page arXiv:1707.03130.

Deb, S., Ngeow, C.-C., Kanbur, S. M., Singh, H. P., Wysocki, D., and Kumar, S. (2018). Geometry of the Large Magellanic Cloud using multiwavelength photometry of classical Cepheids. *MNRAS*, 478(2):2526–2540.

Dehnen, W. and Binney, J. (1998). Mass models of the Milky Way. *MNRAS*, 294:429.

DES Collaboration, Abbott, T., Abdalla, F. B., Aleksić, J., Allam, S., Amara, A., Bacon, D., Balbinot, E., Banerji, M., Bechtol, K., Benoit-Lévy, A., Bernstein, G. M., Bertin, E., Blazek, J., Bonnett, C., Bridle, S., Brooks, D., Brunner, R. J., Buckley-Geer, E., Burke, D. L., Caminha, G. B., Capozzi, D., Carlsen, J., Carnero-Rosell, A., Carollo, M., Carrasco-Kind, M., Carretero, J., Castander, F. J., Clerkin, L., Collett, T., Conselice, C., Crocce, M., Cunha, C. E., D'Andrea, C. B., da Costa, L. N., Davis, T. M., Desai, S., Diehl, H. T., Dietrich, J. P., Dodelson, S., Doel, P., Drlica-Wagner, A., Estrada, J., Etherington, J., Evrard, A. E., Fabbri, J., Finley, D. A., Flaugher, B., Foley, R. J., Fosalba, P., Frieman, J., García-Bellido, J., Gaztanaga, E., Gerdes, D. W., Giannantonio, T., Goldstein, D. A., Gruen, D., Gruendl, R. A., Guarnieri, P., Gutierrez, G., Hartley, W., Honscheid, K., Jain, B., James, D. J., Jeltema, T., Jouvel, S., Kessler, R., King,

A., Kirk, D., Kron, R., Kuehn, K., Kuropatkin, N., Lahav, O., Li, T. S., Lima, M., Lin, H., Maia, M. A. G., Makler, M., Manera, M., Maraston, C., Marshall, J. L., Martini, P., McMahon, R. G., Melchior, P., Merson, A., Miller, C. J., Miquel, R., Mohr, J. J., Morice-Atkinson, X., Naidoo, K., Neilsen, E., Nichol, R. C., Nord, B., Ogando, R., Ostrovski, F., Palmese, A., Papadopoulos, A., Peiris, H. V., Peoples, J., Percival, W. J., Plazas, A. A., Reed, S. L., Refregier, A., Romer, A. K., Roodman, A., Ross, A., Rozo, E., Rykoff, E. S., Sadeh, I., Sako, M., Sánchez, C., Sanchez, E., Santiago, B., Scarpine, V., Schubnell, M., Sevilla-Noarbe, I., Sheldon, E., Smith, M., Smith, R. C., Soares-Santos, M., Sobreira, F., Soumagnac, M., Suchyta, E., Sullivan, M., Swanson, M., Tarle, G., Thaler, J., Thomas, D., Thomas, R. C., Tucker, D., Vieira, J. D., Vikram, V., Walker, A. R., Wechsler, R. H., Weller, J., Wester, W., Whiteway, L., Wilcox, H., Yanny, B., Zhang, Y., and Zuntz, J. (2016). The Dark Energy Survey: more than dark energy - an overview. *MNRAS*, 460(2):1270–1299.

DES Collaboration, Abbott, T. M. C., Abdalla, F. B., Alarcon, A., Aleksić, J., Allam, S., Allen, S., Amara, A., Annis, J., Asorey, J., Avila, S., Bacon, D., Balbinot, E., Banerji, M., Banik, N., Barkhouse, W., Baumer, M., Baxter, E., Bechtol, K., Becker, M. R., Benoit-Lévy, A., Benson, B. A., Bernstein, G. M., Bertin, E., Blazek, J., Bridle, S. L., Brooks, D., Brout, D., Buckley-Geer, E., Burke, D. L., Busha, M. T., Campos, A., Capozzi, D., Carnero Rosell, A., Carrasco Kind, M., Carretero, J., Castander, F. J., Cawthon, R., Chang, C., Chen, N., Childress, M., Choi, A., Conselice, C., Crittenden, R., Crocce, M., Cunha, C. E., D'Andrea, C. B., da Costa, L. N., Das, R., Davis, T. M., Davis, C., De Vicente, J., DePoy, D. L., DeRose, J., Desai, S., Diehl, H. T., Dietrich, J. P., Dodelson, S., Doel, P., Drlica-Wagner, A., Eifler, T. F., Elliott, A. E., Elsner, F., Elvin-Poole, J., Estrada, J., Evrard, A. E., Fang, Y., Fernandez, E., Ferté, A., Finley, D. A., Flaugher, B., Fosalba, P., Friedrich, O., Frieman, J., García-Bellido, J., Garcia-Fernandez, M., Gatti, M., Gaztanaga, E., Gerdes, D. W., Giannantonio, T., Gill, M. S. S., Glazebrook, K., Goldstein, D. A., Gruen, D., Gruendl, R. A., Gschwend, J., Gutierrez, G., Hamilton, S.,

Hartley, W. G., Hinton, S. R., Honscheid, K., Hoyle, B., Huterer, D., Jain, B., James, D. J., Jarvis, M., Jeltema, T., Johnson, M. D., Johnson, M. W. G., Kacprzak, T., Kent, S., Kim, A. G., King, A., Kirk, D., Kokron, N., Kovacs, A., Krause, E., Krawiec, C., Kremin, A., Kuehn, K., Kuhlmann, S., Kuropatkin, N., Lacasa, F., Lahav, O., Li, T. S., Liddle, A. R., Lidman, C., Lima, M., Lin, H., MacCrann, N., Maia, M. A. G., Makler, M., Manera, M., March, M., Marshall, J. L., Martini, P., McMahon, R. G., Melchior, P., Menanteau, F., Miquel, R., Miranda, V., Mudd, D., Muir, J., Möller, A., Neilsen, E., Nichol, R. C., Nord, B., Nugent, P., Ogando, R. L. C., Palmese, A., Peacock, J., Peiris, H. V., Peoples, J., Percival, W. J., Petravick, D., Plazas, A. A., Porredon, A., Prat, J., Pujol, A., Rau, M. M., Refregier, A., Ricker, P. M., Roe, N., Rollins, R. P., Romer, A. K., Roodman, A., Rosenfeld, R., Ross, A. J., Rozo, E., Rykoff, E. S., Sako, M., Salvador, A. I., Samuroff, S., Sánchez, C., Sanchez, E., Santiago, B., Scarpine, V., Schindler, R., Scolnic, D., Secco, L. F., Serrano, S., Sevilla-Noarbe, I., Sheldon, E., Smith, R. C., Smith, M., Smith, J., Soares-Santos, M., Sobreira, F., Suchyta, E., Tarle, G., Thomas, D., Troxel, M. A., Tucker, D. L., Tucker, B. E., Uddin, S. A., Varga, T. N., Vielzeuf, P., Vikram, V., Vivas, A. K., Walker, A. R., Wang, M., Wechsler, R. H., Weller, J., Wester, W., Wolf, R. C., Yanny, B., Yuan, F., Zenteno, A., Zhang, B., Zhang, Y., and Zuntz, J. (2018). Dark Energy Survey year 1 results: Cosmological constraints from galaxy clustering and weak lensing. *Phys. Rev. D*, 98(4):043526.

Desai, S., Armstrong, R., Mohr, J. J., Semler, D. R., Liu, J., Bertin, E., Allam, S. S., Barkhouse, W. A., Bazin, G., Buckley-Geer, E. J., Cooper, M. C., Hansen, S. M., High, F. W., Lin, H., Lin, Y. T., Ngeow, C. C., Rest, A., Song, J., Tucker, D., and Zenteno, A. (2012). The Blanco Cosmology Survey: Data Acquisition, Processing, Calibration, Quality Diagnostics, and Data Release. *ApJ*, 757(1):83.

Diemand, J., Moore, B., and Stadel, J. (2005). Earth-mass dark-matter haloes as the first structures in the early Universe. **??***jnlNature*, 433(7024):389–391.

Dierickx, M. I. P. and Loeb, A. (2017). Predicted Extension of the Sagittarius Stream to the

Milky Way Virial Radius. *ApJ*, 836(1):92.

Dodelson, S. and Widrow, L. M. (1994). Sterile neutrinos as dark matter. **??***jnlPhRvL*, 72(1):17–20.

Dotter, A., Chaboyer, B., Jevremović, D., Kostov, V., Baron, E., and Ferguson, J. W. (2008). The Dartmouth Stellar Evolution Database. **??***jnlApJS*, 178:89–101.

Drlica-Wagner, A., Bechtol, K., Mau, S., McNanna, M., Nadler, E. O., Pace, A. B., Li, T. S., Pieres, A., Rozo, E., Simon, J. D., Walker, A. R., Wechsler, R. H., Abbott, T. M. C., Allam, S., Annis, J., Bertin, E., Brooks, D., Burke, D. L., Rosell, A. C., Carrasco Kind, M., Carretero, J., Costanzi, M., da Costa, L. N., De Vicente, J., Desai, S., Diehl, H. T., Doel, P., Eifler, T. F., Everett, S., Flaugher, B., Frieman, J., García-Bellido, J., Gaztanaga, E., Gruen, D., Gruendl, R. A., Gschwend, J., Gutierrez, G., Honscheid, K., James, D. J., Krause, E., Kuehn, K., Kuropatkin, N., Lahav, O., Maia, M. A. G., Marshall, J. L., Melchior, P., Menanteau, F., Miquel, R., Palmese, A., Plazas, A. A., Sanchez, E., Scarpine, V., Schubnell, M., Serrano, S., Sevilla-Noarbe, I., Smith, M., Suchyta, E., Tarle, G., and DES Collaboration (2020). Milky Way Satellite Census. I. The Observational Selection Function for Milky Way Satellites in DES Y3 and Pan-STARRS DR1. *ApJ*, 893(1):47.

Drlica-Wagner, A., Carlin, J. L., Nidever, D. L., Ferguson, P. S., Kuropatkin, N., Adamów, M., Cerny, W., Choi, Y., Esteves, J. H., Martínez-Vázquez, C. E., Mau, S., Miller, A. E., Mutlu-Pakdil, B., Neilsen, E. H., Olsen, K. A. G., Pace, A. B., Riley, A. H., Sakowska, J. D., Sand, D. J., Santana-Silva, L., Tollerud, E. J., Tucker, D. L., Vivas, A. K., Zaborowski, E., Zenteno, A., Abbott, T. M. C., Allam, S., Bechtol, K., Bell, C. P. M., Bell, E. F., Bilaji, P., Bom, C. R., Carballo-Bello, J. A., Cioni, M. R. L., Diaz-Ocampo, A., de Boer, T. J. L., Erkal, D., Gruendl, R. A., Hernandez-Lang, D., Hughes, A. K., James, D. J., Johnson, L. C., Li, T. S., Mao, Y. Y., Martínez-Delgado, D., Massana, P., McNanna, M., Morgan, R., Nadler, E. O., Noël, N. E. D., Palmese, A., Peter, A. H. G., Rykoff, E. S., Sánchez, J., Shipp, N., Simon, J. D., Smercina, A., Soares-Santos, M., Stringfellow, G. S., Tavangar, K., van der Marel, R. P., Walker, A. R., Wechsler, R. H.,

Wu, J. F., Yanny, B., Fitzpatrick, M., Huang, L., Jacques, A., Nikutta, R., and Scott, A. (2021). The DECam Local Volume Exploration Survey: Overview and First Data Release. *arXiv e-prints*, page arXiv:2103.07476.

Drlica-Wagner, A., Mao, Y.-Y., Adhikari, S., Armstrong, R., Banerjee, A., Banik, N., Bechtol, K., Bird, S., Boddy, K. K., Bonaca, A., Bovy, J., Buckley, M. R., Bulbul, E., Chang, C., Chapline, G., Cohen-Tanugi, J., Cuoco, A., Cyr-Racine, F.-Y., Dawson, W. A., Díaz Rivero, A., Dvorkin, C., Erkal, D., Fassnacht, C. D., García-Bellido, J., Giannotti, M., Gluscevic, V., Golovich, N., Hendel, D., Hezaveh, Y. D., Horiuchi, S., Jee, M. J., Kaplinghat, M., Keeton, C. R., Koposov, S. E., Lam, C. Y., Li, T. S., Lu, J. R., Mandelbaum, R., McDermott, S. D., McNanna, M., Medford, M., Meyer, M., Marc, M., Murgia, S., Nadler, E. O., Necib, L., Nuss, E., Pace, A. B., Peter, A. H. G., Polin, D. A., Prescod-Weinstein, C., Read, J. I., Rosenfeld, R., Shipp, N., Simon, J. D., Slatyer, T. R., Straniero, O., Strigari, L. E., Tollerud, E., Tyson, J. A., Wang, M.-Y., Wechsler, R. H., Wittman, D., Yu, H.-B., Zaharijas, G., Ali-Haïmoud, Y., Annis, J., Birrer, S., Biswas, R., Blazek, J., Brooks, A. M., Buckley-Geer, E., Caputo, R., Charles, E., Digel, S., Dodelson, S., Flaugher, B., Frieman, J., Gawiser, E., Hearin, A. P., Hložek, R., Jain, B., Jeltema, T. E., Koushiappas, S. M., Lisanti, M., LoVerde, M., Mishra-Sharma, S., Newman, J. A., Nord, B., Nourbakhsh, E., Ritz, S., Robertson, B. E., Sánchez-Conde, M. A., Slosar, A., Tait, T. M. P., Verma, A., Vilalta, R., Walter, C. W., Yanny, B., and Zentner, A. R. (2019). Probing the Fundamental Nature of Dark Matter with the Large Synoptic Survey Telescope. *arXiv e-prints*, page arXiv:1902.01055.

Eggen, O. J., Lynden-Bell, D., and Sandage, A. R. (1962). Evidence from the motions of old stars that the Galaxy collapsed. *ApJ*, 136:748.

Erkal, D., Belokurov, V., Laporte, C. F. P., Koposov, S. E., Li, T. S., Grillmair, C. J., Kallivayalil, N., Price-Whelan, A. M., Evans, N. W., Hawkins, K., Hendel, D., Mateu, C., Navarro, J. F., del Pino, A., Slater, C. T., Sohn, S. T., and Orphan Aspen Treasury Collaboration (2019). The total mass of the Large Magellanic Cloud from its perturbation

on the Orphan stream. *MNRAS*, 487(2):2685–2700.

Erkal, D., Koposov, S. E., and Belokurov, V. (2017). A sharper view of Pal 5's tails: discovery of stream perturbations with a novel non-parametric technique. *MNRAS*, 470(1):60–84.

Erkal, D., Li, T. S., Koposov, S. E., Belokurov, V., Balbinot, E., Bechtol, K., Buncher, B., Drlica-Wagner, A., Kuehn, K., Marshall, J. L., Martínez-Vázquez, C. E., Pace, A. B., Shipp, N., Simon, J. D., Stringer, K. M., Vivas, A. K., Wechsler, R. H., Yanny, B., Abdalla, F. B., Allam, S., Annis, J., Avila, S., Bertin, E., Brooks, D., Buckley-Geer, E., Burke, D. L., Carnero Rosell, A., Carrasco Kind, M., Carretero, J., D'Andrea, C. B., da Costa, L. N., Davis, C., De Vicente, J., Doel, P., Eifler, T. F., Evrard, A. E., Flaugher, B., Frieman, J., García-Bellido, J., Gaztanaga, E., Gerdes, D. W., Gruen, D., Gruendl, R. A., Gschwend, J., Gutierrez, G., Hartley, W. G., Hollowood, D. L., Honscheid, K., James, D. J., Krause, E., Maia, M. A. G., March, M., Menanteau, F., Miquel, R., Ogando, R. L. C., Plazas, A. A., Sanchez, E., Santiago, B., Scarpine, V., Schindler, R., Sevilla-Noarbe, I., Smith, M., Smith, R. C., Soares-Santos, M., Sobreira, F., Suchyta, E., Swanson, M. E. C., Tarle, G., Tucker, D. L., and Walker, A. R. (2018). Modelling the Tucana III stream - a close passage with the LMC. *MNRAS*, 481(3):3148–3159.

Erkal, D., Sanders, J. L., and Belokurov, V. (2016). Stray, swing and scatter: angular momentum evolution of orbits and streams in aspherical potentials. *MNRAS*, 461(2):1590–1604.

Ferguson, P. and DePoy, D. L. *et al.* (2018). Development of TCal: a mobile spectrophotometric calibration unit for astronomical imaging systems. In Evans, C. J., Simard, L., and Takami, H., editors, *Ground-based and Airborne Instrumentation for Astronomy VII*, volume 10702 of *Society of Photo-Optical Instrumentation Engineers (SPIE) Conference Series*, page 107023A.

Feroz, F. and Hobson, M. P. (2008). Multimodal nested sampling: an efficient and robust alternative to Markov Chain Monte Carlo methods for astronomical data analyses. *Monthly Notices of the Royal Astronomical Society*, 384(2):449–463.

Feroz, F., Hobson, M. P., and Bridges, M. (2009). MultiNest: an efficient and robust Bayesian inference tool for cosmology and particle physics. *Monthly Notices of the Royal Astronomical Society*, 398(4):1601–1614.

Foreman-Mackey, D., Hogg, D. W., Lang, D., and Goodman, J. (2013). emcee: The MCMC Hammer. **??***jnlPASP*, 125:306.

Freeman, K. and Bland-Hawthorn, J. (2002). The New Galaxy: Signatures of Its Formation. **??***jnlARA&A*, 40:487–537.

Frinchaboy, P. M., Majewski, S. R., Muñoz, R. R., Law, D. R., Łokas, E. L., Kunkel, W. E., Patterson, R. J., and Johnston, K. V. (2012). A 2MASS All-sky View of the Sagittarius Dwarf Galaxy. VII. Kinematics of the Main Body of the Sagittarius dSph. *ApJ*, 756:74.

Fritz, T. K., Battaglia, G., Pawlowski, M. S., Kallivayalil, N., van der Marel, R., Sohn, S. T., Brook, C., and Besla, G. (2018). Gaia DR2 proper motions of dwarf galaxies within 420 kpc. Orbits, Milky Way mass, tidal influences, planar alignments, and group infall. *A&A*, 619:A103.

Gaia Collaboration, Brown, A. G. A., Vallenari, A., Prusti, T., de Bruijne, J. H. J., Babusiaux, C., Bailer-Jones, C. A. L., Biermann, M., Evans, D. W., and Eyer, L. (2018a). Gaia Data Release 2. Summary of the contents and survey properties. *A&A*, 616:A1.

Gaia Collaboration, Brown, A. G. A., Vallenari, A., Prusti, T., de Bruijne, J. H. J., Babusiaux, C., and Biermann, M. (2020). Gaia Early Data Release 3: Summary of the contents and survey properties. *arXiv e-prints*, page arXiv:2012.01533.

Gaia Collaboration, Brown, A. G. A., Vallenari, A., Prusti, T., de Bruijne, J. H. J., Babusiaux, C., Biermann, M., Creevey, O. L., Evans, D. W., Eyer, L., and et al. (2021). Gaia Early Data Release 3. Summary of the contents and survey properties. *A&A*, 649:A1.

Gaia Collaboration, Helmi, A., van Leeuwen, F., McMillan, P. J., Massari, D., Antoja, T., Robin, A. C., Lindegren, L., Bastian, U., Arenou, F., Babusiaux, C., Biermann, M., Breddels, M. A., Hobbs, D., Jordi, C., Pancino, E., Reylé, C., Veljanoski, J., Brown, A. G. A., Vallenari, A., Prusti, T., de Bruijne, J. H. J., Bailer-Jones, C. A. L., Evans, D. W., Eyer,

L., Jansen, F., Klioner, S. A., Lammers, U., Luri, X., Mignard, F., Panem, C., Pourbaix, D., Randich, S., Sartoretti, P., Siddiqui, H. I., Soubiran, C., Walton, N. A., Cropper, M., Drimmel, R., Katz, D., Lattanzi, M. G., Bakker, J., Cacciari, C., Castañeda, J., Chaoul, L., Cheek, N., De Angeli, F., Fabricius, C., Guerra, R., Holl, B., Masana, E., Messineo, R., Mowlavi, N., Nienartowicz, K., Panuzzo, P., Portell, J., Riello, M., Seabroke, G. M., Tanga, P., Thévenin, F., Gracia-Abril, G., Comoretto, G., Garcia-Reinaldos, M., Teyssier, D., Altmann, M., Andrae, R., Audard, M., Bellas-Velidis, I., Benson, K., Berthier, J., Blomme, R., Burgess, P., Busso, G., Carry, B., Cellino, A., Clementini, G., Clotet, M., Creevey, O., Davidson, M., De Ridder, J., Delchambre, L., Dell'Oro, A., Ducourant, C., Fernández-Hernández, J., Fouesneau, M., Frémat, Y., Galluccio, L., García-Torres, M., González-Núñez, J., González-Vidal, J. J., Gosset, E., Guy, L. P., Halbwachs, J. L., Hambly, N. C., Harrison, D. L., Hernández, J., Hestroffer, D., Hodgkin, S. T., Hutton, A., Jasniewicz, G., Jean-Antoine-Piccolo, A., Jordan, S., Korn, A. J., Krone-Martins, A., Lanzafame, A. C., Lebzelter, T., Löffler, W., Manteiga, M., Marrese, P. M., Martín-Fleitas, J. M., Moitinho, A., Mora, A., Muinonen, K., Osinde, J., Pauwels, T., Petit, J. M., Recio-Blanco, A., Richards, P. J., Rimoldini, L., Sarro, L. M., Siopis, C., Smith, M., Sozzetti, A., Süveges, M., Torra, J., van Reeven, W., Abbas, U., Abreu Aramburu, A., Accart, S., Aerts, C., Altavilla, G., Álvarez, M. A., Alvarez, R., Alves, J., Anderson, R. I., Andrei, A. H., Anglada Varela, E., Antiche, E., Arcay, B., Astraatmadja, T. L., Bach, N., Baker, S. G., Balaguer-Núñez, L., Balm, P., Barache, C., Barata, C., Barbato, D., Barblan, F., Barklem, P. S., Barrado, D., Barros, M., Barstow, M. A., Bartholomé Muñoz, S., Bassilana, J. L., Becciani, U., Bellazzini, M., Berihuete, A., Bertone, S., Bianchi, L., Bienaymé, O., Blanco-Cuaresma, S., Boch, T., Boeche, C., Bombrun, A., Borrachero, R., Bossini, D., Bouquillon, S., Bourda, G., Bragaglia, A., Bramante, L., Bressan, A., Brouillet, N., Brüsemeister, T., Brugaletta, E., Bucciarelli, B., Burlacu, A., Busonero, D., Butkevich, A. G., Buzzi, R., Caffau, E., Cancelliere, R., Cannizzaro, G., Cantat-Gaudin, T., Carballo, R., Carlucci, T., Carrasco, J. M., Casamiquela, L., Castellani, M., Castro-Ginard, A., Charlot,

P., Chemin, L., Chiavassa, A., Cocozza, G., Costigan, G., Cowell, S., Crifo, F., Crosta, M., Crowley, C., Cuypers, J., Dafonte, C., Damerdji, Y., Dapergolas, A., David, P., David, M., de Laverny, P., De Luise, F., De March, R., de Martino, D., de Souza, R., de Torres, A., Debosscher, J., del Pozo, E., Delbo, M., Delgado, A., Delgado, H. E., Di Matteo, P., Diakite, S., Diener, C., Distefano, E., Dolding, C., Drazinos, P., Durán, J., Edvardsson, B., Enke, H., Eriksson, K., Esquej, P., Eynard Bontemps, G., Fabre, C., Fabrizio, M., Faigler, S., Falcão, A. J., Farràs Casas, M., Federici, L., Fedorets, G., Fernique, P., Figueras, F., Filippi, F., Findeisen, K., Fonti, A., Fraile, E., Fraser, M., Frézouls, B., Gai, M., Galleti, S., Garabato, D., García-Sedano, F., Garofalo, A., Garralda, N., Gavel, A., Gavras, P., Gerssen, J., Geyer, R., Giacobbe, P., Gilmore, G., Girona, S., Giuffrida, G., Glass, F., Gomes, M., Granvik, M., Gueguen, A., Guerrier, A., Guiraud, J., Gutiérrez-Sánchez, R., Hofmann, W., Holland, G., Huckle, H. E., Hypki, A., Icardi, V., Janßen, K., Jevardat de Fombelle, G., Jonker, P. G., Juhász, Á. L., Julbe, F., Karampelas, A., Kewley, A., Klar, J., Kochoska, A., Kohley, R., Kolenberg, K., Kontizas, M., Kontizas, E., Koposov, S. E., Kordopatis, G., Kostrzewa-Rutkowska, Z., Koubsky, P., Lambert, S., Lanza, A. F., Lasne, Y., Lavigne, J. B., Le Fustec, Y., Le Poncin-Lafitte, C., Lebreton, Y., Leccia, S., Leclerc, N., Lecoeur-Taibi, I., Lenhardt, H., Leroux, F., Liao, S., Licata, E., Lindstrøm, H. E. P., Lister, T. A., Livanou, E., Lobel, A., López, M., Managau, S., Mann, R. G., Mantelet, G., Marchal, O., Marchant, J. M., Marconi, M., Marinoni, S., Marschalkó, G., Marshall, D. J., Martino, M., Marton, G., Mary, N., Matijevič, G., Mazeh, T., Messina, S., Michalik, D., Millar, N. R., Molina, D., Molinaro, R., Molnár, L., Montegriffo, P., Mor, R., Morbidelli, R., Morel, T., Morris, D., Mulone, A. F., Muraveva, T., Musella, I., Nelemans, G., Nicastro, L., Noval, L., O'Mullane, W., Ordénovic, C., Ordóñez-Blanco, D., Osborne, P., Pagani, C., Pagano, I., Pailler, F., Palacin, H., Palaversa, L., Panahi, A., Pawlak, M., Piersimoni, A. M., Pineau, F. X., Plachy, E., Plum, G., Poggio, E., Poujoulet, E., Prša, A., Pulone, L., Racero, E., Ragaini, S., Rambaux, N., Ramos-Lerate, M., Regibo, S., Riclet, F., Ripepi, V., Riva, A., Rivard, A., Rixon, G., Roegiers, T., Roelens,

M., Romero-Gómez, M., Rowell, N., Royer, F., Ruiz-Dern, L., Sadowski, G., Sagristà Sellés, T., Sahlmann, J., Salgado, J., Salguero, E., Sanna, N., Santana-Ros, T., Sarasso, M., Savietto, H., Schultheis, M., Sciacca, E., Segol, M., Segovia, J. C., Ségransan, D., Shih, I. C., Siltala, L., Silva, A. F., Smart, R. L., Smith, K. W., Solano, E., Solitro, F., Sordo, R., Soria Nieto, S., Souchay, J., Spagna, A., Spoto, F., Stampa, U., Steele, I. A., Steidelmüller, H., Stephenson, C. A., Stoev, H., Suess, F. F., Surdej, J., Szabados, L., Szegedi-Elek, E., Tapiador, D., Taris, F., Tauran, G., Taylor, M. B., Teixeira, R., Terrett, D., Teyssand ier, P., Thuillot, W., Titarenko, A., Torra Clotet, F., Turon, C., Ulla, A., Utrilla, E., Uzzi, S., Vaillant, M., Valentini, G., Valette, V., van Elteren, A., Van Hemelryck, E., van Leeuwen, M., Vaschetto, M., Vecchiato, A., Viala, Y., Vicente, D., Vogt, S., von Essen, C., Voss, H., Votruba, V., Voutsinas, S., Walmsley, G., Weiler, M., Wertz, O., Wevems, T., Wyrzykowski, Ł., Yoldas, A., Žerjal, M., Ziaeepour, H., Zorec, J., Zschocke, S., Zucker, S., Zurbach, C., and Zwitter, T. (2018b). Gaia Data Release 2. Kinematics of globular clusters and dwarf galaxies around the Milky Way. *A&A*, 616:A12.

Gaia Collaboration, Prusti, T., de Bruijne, J. H. J., Brown, A. G. A., Vallenari, A., Babusiaux, C., Bailer-Jones, C. A. L., Bastian, U., Biermann, M., Evans, D. W., Eyer, L., Jansen, F., Jordi, C., Klioner, S. A., Lammers, U., Lindegren, L., Luri, X., Mignard, F., Milligan, D. J., Panem, C., Poinsignon, V., Pourbaix, D., Randich, S., Sarri, G., Sartoretti, P., Siddiqui, H. I., Soubiran, C., Valette, V., van Leeuwen, F., Walton, N. A., Aerts, C., Arenou, F., Cropper, M., Drimmel, R., Høg, E., Katz, D., Lattanzi, M. G., O'Mullane, W., Grebel, E. K., Holland, A. D., Huc, C., Passot, X., Bramante, L., Cacciari, C., Castañeda, J., Chaoul, L., Cheek, N., De Angeli, F., Fabricius, C., Guerra, R., Hernández, J., Jean-Antoine-Piccolo, A., Masana, E., Messineo, R., Mowlavi, N., Nienartowicz, K., Ordóñez-Blanco, D., Panuzzo, P., Portell, J., Richards, P. J., Riello, M., Seabroke, G. M., Tanga, P., Thévenin, F., Torra, J., Els, S. G., Gracia-Abril, G., Comoretto, G., Garcia-Reinaldos, M., Lock, T., Mercier, E., Altmann, M., Andrae, R., Astraatmadja, T. L., Bellas-Velidis, I., Benson, K., Berthier, J., Blomme, R., Busso, G., Carry, B., Cellino,

A., Clementini, G., Cowell, S., Creevey, O., Cuypers, J., Davidson, M., De Ridder, J., de Torres, A., Delchambre, L., Dell'Oro, A., Ducourant, C., Frémat, Y., García-Torres, M., Gosset, E., Halbwachs, J. L., Hambly, N. C., Harrison, D. L., Hauser, M., Hestroffer, D., Hodgkin, S. T., Huckle, H. E., Hutton, A., Jasniewicz, G., Jordan, S., Kontizas, M., Korn, A. J., Lanzafame, A. C., Manteiga, M., Moitinho, A., Muinonen, K., Osinde, J., Pancino, E., Pauwels, T., Petit, J. M., Recio-Blanco, A., Robin, A. C., Sarro, L. M., Siopis, C., Smith, M., Smith, K. W., Sozzetti, A., Thuillot, W., van Reeven, W., Viala, Y., Abbas, U., Abreu Aramburu, A., Accart, S., Aguado, J. J., Allan, P. M., Allasia, W., Altavilla, G., Álvarez, M. A., Alves, J., Anderson, R. I., Andrei, A. H., Anglada Varela, E., Antiche, E., Antoja, T., Antón, S., Arcay, B., Atzei, A., Ayache, L., Bach, N., Baker, S. G., Balaguer-Núñez, L., Barache, C., Barata, C., Barbier, A., Barblan, F., Baroni, M., Barrado y Navascués, D., Barros, M., Barstow, M. A., Becciani, U., Bellazzini, M., Bellei, G., Bello García, A., Belokurov, V., Bendjoya, P., Berihuete, A., Bianchi, L., Bienaymé, O., Billebaud, F., Blagorodnova, N., Blanco-Cuaresma, S., Boch, T., Bombrun, A., Borrachero, R., Bouquillon, S., Bourda, G., Bouy, H., Bragaglia, A., Breddels, M. A., Brouillet, N., Brüsemeister, T., Bucciarelli, B., Budnik, F., Burgess, P., Burgon, R., Burlacu, A., Busonero, D., Buzzi, R., Caffau, E., Cambras, J., Campbell, H., Cancelliere, R., Cantat-Gaudin, T., Carlucci, T., Carrasco, J. M., Castellani, M., Charlot, P., Charnas, J., Charvet, P., Chassat, F., Chiavassa, A., Clotet, M., Cocozza, G., Collins, R. S., Collins, P., Costigan, G., Crifo, F., Cross, N. J. G., Crosta, M., Crowley, C., Dafonte, C., Damerdji, Y., Dapergolas, A., David, P., David, M., De Cat, P., de Felice, F., de Laverny, P., De Luise, F., De March, R., de Martino, D., de Souza, R., Debosscher, J., del Pozo, E., Delbo, M., Delgado, A., Delgado, H. E., di Marco, F., Di Matteo, P., Diakite, S., Distefano, E., Dolding, C., Dos Anjos, S., Drazinos, P., Durán, J., Dzigan, Y., Ecale, E., Edvardsson, B., Enke, H., Erdmann, M., Escolar, D., Espina, M., Evans, N. W., Eynard Bontemps, G., Fabre, C., Fabrizio, M., Faigler, S., Falcão, A. J., Farràs Casas, M., Faye, F., Federici, L., Fedorets, G., Fernández-Hernández, J., Fernique, P., Fienga, A., Figueras,

F., Filippi, F., Findeisen, K., Fonti, A., Fouesneau, M., Fraile, E., Fraser, M., Fuchs, J., Furnell, R., Gai, M., Galleti, S., Galluccio, L., Garabato, D., García-Sedano, F., Garé, P., Garofalo, A., Garralda, N., Gavras, P., Gerssen, J., Geyer, R., Gilmore, G., Girona, S., Giuffrida, G., Gomes, M., González-Marcos, A., González-Núñez, J., González-Vidal, J. J., Granvik, M., Guerrier, A., Guillout, P., Guiraud, J., Gúrpide, A., Gutiérrez-Sánchez, R., Guy, L. P., Haigron, R., Hatzidimitriou, D., Haywood, M., Heiter, U., Helmi, A., Hobbs, D., Hofmann, W., Holl, B., Holland, G., Hunt, J. A. S., Hypki, A., Icardi, V., Irwin, M., Jevardat de Fombelle, G., Jofré, P., Jonker, P. G., Jorissen, A., Julbe, F., Karampelas, A., Kochoska, A., Kohley, R., Kolenberg, K., Kontizas, E., Koposov, S. E., Kordopatis, G., Koubsky, P., Kowalczyk, A., Krone-Martins, A., Kudryashova, M., Kull, I., Bachchan, R. K., Lacoste-Seris, F., Lanza, A. F., Lavigne, J. B., Le Poncin-Lafitte, C., Lebreton, Y., Lebzelter, T., Leccia, S., Leclerc, N., Lecoeur-Taibi, I., Lemaitre, V., Lenhardt, H., Leroux, F., Liao, S., Licata, E., Lindstrøm, H. E. P., Lister, T. A., Livanou, E., Lobel, A., Löffler, W., López, M., Lopez-Lozano, A., Lorenz, D., Loureiro, T., MacDonald, I., Magalhães Fernandes, T., Managau, S., Mann, R. G., Mantelet, G., Marchal, O., Marchant, J. M., Marconi, M., Marie, J., Marinoni, S., Marrese, P. M., Marschalkó, G., Marshall, D. J., Martín-Fleitas, J. M., Martino, M., Mary, N., Matijevič, G., Mazeh, T., McMillan, P. J., Messina, S., Mestre, A., Michalik, D., Millar, N. R., Miranda, B. M. H., Molina, D., Molinaro, R., Molinaro, M., Molnár, L., Moniez, M., Montegriffo, P., Monteiro, D., Mor, R., Mora, A., Morbidelli, R., Morel, T., Morgenthaler, S., Morley, T., Morris, D., Mulone, A. F., Muraveva, T., Musella, I., Narbonne, J., Nelemans, G., Nicastro, L., Noval, L., Ordénovic, C., Ordieres-Meré, J., Osborne, P., Pagani, C., Pagano, I., Pailler, F., Palacin, H., Palaversa, L., Parsons, P., Paulsen, T., Pecoraro, M., Pedrosa, R., Pentikäinen, H., Pereira, J., Pichon, B., Piersimoni, A. M., Pineau, F. X., Plachy, E., Plum, G., Poujoulet, E., Prša, A., Pulone, L., Ragaini, S., Rago, S., Rambaux, N., Ramos-Lerate, M., Ranalli, P., Rauw, G., Read, A., Regibo, S., Renk, F., Reylé, C., Ribeiro, R. A., Rimoldini, L., Ripepi, V., Riva, A., Rixon, G., Roelens, M., Romero-Gómez, M., Rowell,

N., Royer, F., Rudolph, A., Ruiz-Dern, L., Sadowski, G., Sagristà Sellés, T., Sahlmann, J., Salgado, J., Salguero, E., Sarasso, M., Savietto, H., Schnorhk, A., Schultheis, M., Sciacca, E., Segol, M., Segovia, J. C., Segransan, D., Serpell, E., Shih, I. C., Smareglia, R., Smart, R. L., Smith, C., Solano, E., Solitro, F., Sordo, R., Soria Nieto, S., Souchay, J., Spagna, A., Spoto, F., Stampa, U., Steele, I. A., Steidelmüller, H., Stephenson, C. A., Stoev, H., Suess, F. F., Süveges, M., Surdej, J., Szabados, L., Szegedi-Elek, E., Tapiador, D., Taris, F., Tauran, G., Taylor, M. B., Teixeira, R., Terrett, D., Tingley, B., Trager, S. C., Turon, C., Ulla, A., Utrilla, E., Valentini, G., van Elteren, A., Van Hemelryck, E., van Leeuwen, M., Varadi, M., Vecchiato, A., Veljanoski, J., Via, T., Vicente, D., Vogt, S., Voss, H., Votruba, V., Voutsinas, S., Walmsley, G., Weiler, M., Weingrill, K., Werner, D., Wevers, T., Whitehead, G., Wyrzykowski, Ł., Yoldas, A., Žerjal, M., Zucker, S., Zurbach, C., Zwitter, T., Alecu, A., Allen, M., Allende Prieto, C., Amorim, A., Anglada-Escudé, G., Arsenijevic, V., Azaz, S., Balm, P., Beck, M., Bernstein, H. H., Bigot, L., Bijaoui, A., Blasco, C., Bonfigli, M., Bono, G., Boudreault, S., Bressan, A., Brown, S., Brunet, P. M., Bunclark, P., Buonanno, R., Butkevich, A. G., Carret, C., Carrion, C., Chemin, L., Chéreau, F., Corcione, L., Darmigny, E., de Boer, K. S., de Teodoro, P., de Zeeuw, P. T., Delle Luche, C., Domingues, C. D., Dubath, P., Fodor, F., Frézouls, B., Fries, A., Fustes, D., Fyfe, D., Gallardo, E., Gallegos, J., Gardiol, D., Gebran, M., Gomboc, A., Gómez, A., Grux, E., Gueguen, A., Heyrovsky, A., Hoar, J., Iannicola, G., Isasi Parache, Y., Janotto, A. M., Joliet, E., Jonckheere, A., Keil, R., Kim, D. W., Klagyivik, P., Klar, J., Knude, J., Kochukhov, O., Kolka, I., Kos, J., Kutka, A., Lainey, V., LeBouquin, D., Liu, C., Loreggia, D., Makarov, V. V., Marseille, M. G., Martayan, C., Martinez-Rubi, O., Massart, B., Meynadier, F., Mignot, S., Munari, U., Nguyen, A. T., Nordlander, T., Ocvirk, P., O'Flaherty, K. S., Olias Sanz, A., Ortiz, P., Osorio, J., Oszkiewicz, D., Ouzounis, A., Palmer, M., Park, P., Pasquato, E., Peltzer, C., Peralta, J., Péturaud, F., Pieniluoma, T., Pigozzi, E., Poels, J., Prat, G., Prod'homme, T., Raison, F., Rebordao, J. M., Risquez, D., Rocca-Volmerange, B., Rosen, S., Ruiz-Fuertes, M. I., Russo, F., Sembay, S., Serraller

Vizcaino, I., Short, A., Siebert, A., Silva, H., Sinachopoulos, D., Slezak, E., Soffel, M., Sosnowska, D., Straižys, V., ter Linden, M., Terrell, D., Theil, S., Tiede, C., Troisi, L., Tsalmantza, P., Tur, D., Vaccari, M., Vachier, F., Valles, P., Van Hamme, W., Veltz, L., Virtanen, J., Wallut, J. M., Wichmann, R., Wilkinson, M. I., Ziaeepour, H., and Zschocke, S. (2016a). The Gaia mission. *A&A*, 595:A1.

Gaia Collaboration, Prusti, T., de Bruijne, J. H. J., Brown, A. G. A., Vallenari, A., Babusiaux, C., Bailer-Jones, C. A. L., Bastian, U., Biermann, M., Evans, D. W., Eyer, L., Jansen, F., Jordi, C., Klioner, S. A., Lammers, U., Lindegren, L., Luri, X., Mignard, F., Milligan, D. J., Panem, C., Poinsignon, V., Pourbaix, D., Randich, S., Sarri, G., Sartoretti, P., Siddiqui, H. I., Soubiran, C., Valette, V., van Leeuwen, F., Walton, N. A., Aerts, C., Arenou, F., Cropper, M., Drimmel, R., Høg, E., Katz, D., Lattanzi, M. G., O´Mullane, W., Grebel, E. K., Holland, A. D., Huc, C., Passot, X., Bramante, L., Cacciari, C., Castañeda, J., Chaoul, L., Cheek, N., De Angeli, F., Fabricius, C., Guerra, R., Hernández, J., Jean-Antoine-Piccolo, A., Masana, E., Messineo, R., Mowlavi, N., Nienartowicz, K., Ordóñez-Blanco, D., Panuzzo, P., Portell, J., Richards, P. J., Riello, M., Seabroke, G. M., Tanga, P., Thévenin, F., Torra, J., Els, S. G., Gracia-Abril, G., Comoretto, G., Garcia-Reinaldos, M., Lock, T., Mercier, E., Altmann, M., Andrae, R., Astraatmadja, T. L., Bellas-Velidis, I., Benson, K., Berthier, J., Blomme, R., Busso, G., Carry, B., Cellino, A., Clementini, G., Cowell, S., Creevey, O., Cuypers, J., Davidson, M., De Ridder, J., de Torres, A., Delchambre, L., Dell´Oro, A., Ducourant, C., Frémat, Y., García-Torres, M., Gosset, E., Halbwachs, J.-L., Hambly, N. C., Harrison, D. L., Hauser, M., Hestroffer, D., Hodgkin, S. T., Huckle, H. E., Hutton, A., Jasniewicz, G., Jordan, S., Kontizas, M., Korn, A. J., Lanzafame, A. C., Manteiga, M., Moitinho, A., Muinonen, K., Osinde, J., Pancino, E., Pauwels, T., Petit, J.-M., Recio-Blanco, A., Robin, A. C., Sarro, L. M., Siopis, C., Smith, M., Smith, K. W., Sozzetti, A., Thuillot, W., van Reeven, W., Viala, Y., Abbas, U., Abreu Aramburu, A., Accart, S., Aguado, J. J., Allan, P. M., Allasia, W., Altavilla, G., Álvarez, M. A., Alves, J., Anderson, R. I., Andrei, A. H., Anglada Varela,

E., Antiche, E., Antoja, T., Antón, S., Arcay, B., Atzei, A., Ayache, L., Bach, N., Baker, S. G., Balaguer-Núñez, L., Barache, C., Barata, C., Barbier, A., Barblan, F., Baroni, M., Barrado y Navascués, D., Barros, M., Barstow, M. A., Becciani, U., Bellazzini, M., Bellei, G., Bello García, A., Belokurov, V., Bendjoya, P., Berihuete, A., Bianchi, L., Bienaymé, O., Billebaud, F., Blagorodnova, N., Blanco-Cuaresma, S., Boch, T., Bombrun, A., Borrachero, R., Bouquillon, S., Bourda, G., Bouy, H., Bragaglia, A., Breddels, M. A., Brouillet, N., Brüsemeister, T., Bucciarelli, B., Budnik, F., Burgess, P., Burgon, R., Burlacu, A., Busonero, D., Buzzi, R., Caffau, E., Cambras, J., Campbell, H., Cancelliere, R., Cantat-Gaudin, T., Carlucci, T., Carrasco, J. M., Castellani, M., Charlot, P., Charnas, J., Charvet, P., Chassat, F., Chiavassa, A., Clotet, M., Cocozza, G., Collins, R. S., Collins, P., Costigan, G., Crifo, F., Cross, N. J. G., Crosta, M., Crowley, C., Dafonte, C., Damerdji, Y., Dapergolas, A., David, P., David, M., De Cat, P., de Felice, F., de Laverny, P., De Luise, F., De March, R., de Martino, D., de Souza, R., Debosscher, J., del Pozo, E., Delbo, M., Delgado, A., Delgado, H. E., di Marco, F., Di Matteo, P., Diakite, S., Distefano, E., Dolding, C., Dos Anjos, S., Drazinos, P., Durán, J., Dzigan, Y., Ecale, E., Edvardsson, B., Enke, H., Erdmann, M., Escolar, D., Espina, M., Evans, N. W., Eynard Bontemps, G., Fabre, C., Fabrizio, M., Faigler, S., Falcão, A. J., Farràs Casas, M., Faye, F., Federici, L., Fedorets, G., Fernández-Hernández, J., Fernique, P., Fienga, A., Figueras, F., Filippi, F., Findeisen, K., Fonti, A., Fouesneau, M., Fraile, E., Fraser, M., Fuchs, J., Furnell, R., Gai, M., Galleti, S., Galluccio, L., Garabato, D., García-Sedano, F., Garé, P., Garofalo, A., Garralda, N., Gavras, P., Gerssen, J., Geyer, R., Gilmore, G., Girona, S., Giuffrida, G., Gomes, M., González-Marcos, A., González-Núñez, J., González-Vidal, J. J., Granvik, M., Guerrier, A., Guillout, P., Guiraud, J., Gúrpide, A., Gutiérrez-Sánchez, R., Guy, L. P., Haigron, R., Hatzidimitriou, D., Haywood, M., Heiter, U., Helmi, A., Hobbs, D., Hofmann, W., Holl, B., Holland, G., Hunt, J. A. S., Hypki, A., Icardi, V., Irwin, M., Jevardat de Fombelle, G., Jofré, P., Jonker, P. G., Jorissen, A., Julbe, F., Karampelas, A., Kochoska, A., Kohley, R., Kolenberg, K., Kontizas, E., Koposov, S. E., Kordopatis,

G., Koubsky, P., Kowalczyk, A., Krone-Martins, A., Kudryashova, M., Kull, I., Bachchan, R. K., Lacoste-Seris, F., Lanza, A. F., Lavigne, J.-B., Le Poncin-Lafitte, C., Lebreton, Y., Lebzelter, T., Leccia, S., Leclerc, N., Lecoeur-Taibi, I., Lemaitre, V., Lenhardt, H., Leroux, F., Liao, S., Licata, E., Lindstrøm, H. E. P., Lister, T. A., Livanou, E., Lobel, A., Löffler, W., López, M., Lopez-Lozano, A., Lorenz, D., Loureiro, T., MacDonald, I., Magalhães Fernandes, T., Managau, S., Mann, R. G., Mantelet, G., Marchal, O., Marchant, J. M., Marconi, M., Marie, J., Marinoni, S., Marrese, P. M., Marschalkó, G., Marshall, D. J., Martín-Fleitas, J. M., Martino, M., Mary, N., Matijevic, G., Mazeh, T., McMillan, P. J., Messina, S., Mestre, A., Michalik, D., Millar, N. R., Miranda, B. M. H., Molina, D., Molinaro, R., Molinaro, M., Molnár, L., Moniez, M., Montegriffo, P., Monteiro, D., Mor, R., Mora, A., Morbidelli, R., Morel, T., Morgenthaler, S., Morley, T., Morris, D., Mulone, A. F., Muraveva, T., Musella, I., Narbonne, J., Nelemans, G., Nicastro, L., Noval, L., Ordénovic, C., Ordieres-Meré, J., Osborne, P., Pagani, C., Pagano, I., Pailler, F., Palacin, H., Palaversa, L., Parsons, P., Paulsen, T., Pecoraro, M., Pedrosa, R., Pentikäinen, H., Pereira, J., Pichon, B., Piersimoni, A. M., Pineau, F.-X., Plachy, E., Plum, G., Poujoulet, E., Prsa, A., Pulone, L., Ragaini, S., Rago, S., Rambaux, N., Ramos-Lerate, M., Ranalli, P., Rauw, G., Read, A., Regibo, S., Renk, F., Reylé, C., Ribeiro, R. A., Rimoldini, L., Ripepi, V., Riva, A., Rixon, G., Roelens, M., Romero-Gómez, M., Rowell, N., Royer, F., Rudolph, A., Ruiz-Dern, L., Sadowski, G., Sagristà Sellés, T., Sahlmann, J., Salgado, J., Salguero, E., Sarasso, M., Savietto, H., Schnorhk, A., Schultheis, M., Sciacca, E., Segol, M., Segovia, J. C., Segransan, D., Serpell, E., Shih, I-C., Smareglia, R., Smart, R. L., Smith, C., Solano, E., Solitro, F., Sordo, R., Soria Nieto, S., Souchay, J., Spagna, A., Spoto, F., Stampa, U., Steele, I. A., Steidelmüller, H., Stephenson, C. A., Stoev, H., Suess, F. F., Süveges, M., Surdej, J., Szabados, L., Szegedi-Elek, E., Tapiador, D., Taris, F., Tauran, G., Taylor, M. B., Teixeira, R., Terrett, D., Tingley, B., Trager, S. C., Turon, C., Ulla, A., Utrilla, E., Valentini, G., van Elteren, A., Van Hemelryck, E., van Leeuwen, M., Varadi, M., Vecchiato, A., Veljanoski, J., Via, T., Vicente, D., Vogt, S.,

Voss, H., Votruba, V., Voutsinas, S., Walmsley, G., Weiler, M., Weingrill, K., Werner, D., Wevers, T., Whitehead, G., Wyrzykowski, L., Yoldas, A., Zerjal, M., Zucker, S., Zurbach, C., Zwitter, T., Alecu, A., Allen, M., Allende Prieto, C., Amorim, A., Anglada-Escudé, G., Arsenijevic, V., Azaz, S., Balm, P., Beck, M., Bernstein, H.-H., Bigot, L., Bijaoui, A., Blasco, C., Bonfigli, M., Bono, G., Boudreault, S., Bressan, A., Brown, S., Brunet, P.-M., Bunclark, P., Buonanno, R., Butkevich, A. G., Carret, C., Carrion, C., Chemin, L., Chéreau, F., Corcione, L., Darmigny, E., de Boer, K. S., de Teodoro, P., de Zeeuw, P. T., Delle Luche, C., Domingues, C. D., Dubath, P., Fodor, F., Frézouls, B., Fries, A., Fustes, D., Fyfe, D., Gallardo, E., Gallegos, J., Gardiol, D., Gebran, M., Gomboc, A., Gómez, A., Grux, E., Gueguen, A., Heyrovsky, A., Hoar, J., Iannicola, G., Isasi Parache, Y., Janotto, A.-M., Joliet, E., Jonckheere, A., Keil, R., Kim, D.-W., Klagyivik, P., Klar, J., Knude, J., Kochukhov, O., Kolka, I., Kos, J., Kutka, A., Lainey, V., LeBouquin, D., Liu, C., Loreggia, D., Makarov, V. V., Marseille, M. G., Martayan, C., Martinez-Rubi, O., Massart, B., Meynadier, F., Mignot, S., Munari, U., Nguyen, A.-T., Nordlander, T., Ocvirk, P., O´Flaherty, K. S., Olias Sanz, A., Ortiz, P., Osorio, J., Oszkiewicz, D., Ouzounis, A., Palmer, M., Park, P., Pasquato, E., Peltzer, C., Peralta, J., Péturaud, F., Pieniluoma, T., Pigozzi, E., Poels, J., Prat, G., Prod´homme, T., Raison, F., Rebordao, J. M., Risquez, D., Rocca-Volmerange, B., Rosen, S., Ruiz-Fuertes, M. I., Russo, F., Sembay, S., Serraller Vizcaino, I., Short, A., Siebert, A., Silva, H., Sinachopoulos, D., Slezak, E., Soffel, M., Sosnowska, D., Straizys, V., ter Linden, M., Terrell, D., Theil, S., Tiede, C., Troisi, L., Tsalmantza, P., Tur, D., Vaccari, M., Vachier, F., Valles, P., Van Hamme, W., Veltz, L., Virtanen, J., Wallut, J.-M., Wichmann, R., Wilkinson, M. I., Ziaeepour, H., and Zschocke, S. (2016b). The gaia mission. *A&A*, 595:A1.

Gelman, A. and Rubin, D. B. (1992). Inference from Iterative Simulation Using Multiple Sequences. *Statistical Science*, 7(4):457 – 472.

Gibbons, S. L. J., Belokurov, V., and Evans, N. W. (2014). 'Skinny Milky Way please', says Sagittarius. *MNRAS*, 445:3788–3802.

Gibbons, S. L. J., Belokurov, V., and Evans, N. W. (2017). A tail of two populations: chemo-dynamics of the Sagittarius stream and implications for its original mass. *MNRAS*, 464(1):794–809.

Gonzalez, J., Dai, Z., Hennig, P., and Lawrence, N. (2016). Batch bayesian optimization via local penalization. In Gretton, A. and Robert, C. C., editors, *Proceedings of the 19th International Conference on Artificial Intelligence and Statistics*, volume 51 of *Proceedings of Machine Learning Research*, pages 648–657, Cadiz, Spain. PMLR.

Górski, K. M., Hivon, E., Banday, A. J., Wandelt, B. D., Hansen, F. K., Reinecke, M., and Bartelmann, M. (2005). HEALPix: A Framework for High-Resolution Discretization and Fast Analysis of Data Distributed on the Sphere. *ApJ*, 622:759–771.

Gravity Collaboration, Abuter, R., Amorim, A., Bauböck, M., Berger, J. P., Bonnet, H., Brand ner, W., Clénet, Y., Coudé Du Foresto, V., de Zeeuw, P. T., Dexter, J., Duvert, G., Eckart, A., Eisenhauer, F., Förster Schreiber, N. M., Garcia, P., Gao, F., Gendron, E., Genzel, R., Gerhard, O., Gillessen, S., Habibi, M., Haubois, X., Henning, T., Hippler, S., Horrobin, M., Jiménez-Rosales, A., Jocou, L., Kervella, P., Lacour, S., Lapeyrère, V., Le Bouquin, J. B., Léna, P., Ott, T., Paumard, T., Perraut, K., Perrin, G., Pfuhl, O., Rabien, S., Rodriguez Coira, G., Rousset, G., Scheithauer, S., Sternberg, A., Straub, O., Straubmeier, C., Sturm, E., Tacconi, L. J., Vincent, F., von Fellenberg, S., Waisberg, I., Widmann, F., Wieprecht, E., Wiezorrek, E., Woillez, J., and Yazici, S. (2019). A geometric distance measurement to the Galactic center black hole with 0.3% uncertainty. *A&A*, 625:L10.

Green, A. M., Hofmann, S., and Schwarz, D. J. (2004). The power spectrum of SUSY-CDM on subgalactic scales. *MNRAS*, 353(3):L23–L27.

Grillmair, C. J. and Dionatos, O. (2006). Detection of a 63° Cold Stellar Stream in the Sloan Digital Sky Survey. *ApJ*, 643(1):L17–L20.

Hamanowicz, A., Pietrukowicz, P., Udalski, A., Mróz, P., Soszyński, I., Szymański, M. K., Skowron, J., Poleski, R., Wyrzykowski, Ł., Kozłowski, S., Pawlak, M., and Ulaczyk, K.

(2016). OGLE Study of the Sagittarius Dwarf Spheroidal Galaxy and its M54 Globular Cluster. *Acta Astron.*, 66:197–217.

Hayashi, K. and Chiba, M. (2015). Structural Properties of Non-spherical Dark Halos in Milky Way and Andromeda Dwarf Spheroidal Galaxies. *ApJ*, 810(1):22.

Helmi, A. (2020). Streams, Substructures, and the Early History of the Milky Way. **??***jnlARA&A*, 58:205–256.

Hernitschek, N., Sesar, B., Rix, H.-W., Belokurov, V., Martinez-Delgado, D., Martin, N. F., Kaiser, N., Hodapp, K., Chambers, K. C., and Wainscoat, R. (2017). The Geometry of the Sagittarius Stream from Pan-STARRS1 3π RR Lyrae. *ApJ*, 850(1):96.

Hernquist, L. (1990). An Analytical Model for Spherical Galaxies and Bulges. *ApJ*, 356:359.

Hu, W., Barkana, R., and Gruzinov, A. (2000). Fuzzy cold dark matter: The wave properties of ultralight particles. *Phys. Rev. Lett.*, 85:1158–1161.

Hunter, J. D. (2007). Matplotlib: A 2d graphics environment. *Computing In Science & Engineering*, 9(3):90–95.

Ibata, R., Malhan, K., Martin, N., Aubert, D., Famaey, B., Bianchini, P., Monari, G., Siebert, A., Thomas, G. F., Bellazzini, M., Bonifacio, P., Caffau, E., and Renaud, F. (2020). Charting the Galactic acceleration field I. A search for stellar streams with Gaia DR2 and EDR3 with follow-up from ESPaDOnS and UVES. *arXiv e-prints*, page arXiv:2012.05245.

Ibata, R. A. and Lewis, G. F. (1998). Galactic Indigestion: Numerical Simulations of the Milky Way's Closest Neighbor. *ApJ*, 500(2):575–590.

Ibata, R. A., Lewis, G. F., Irwin, M. J., and Quinn, T. (2002). Uncovering cold dark matter halo substructure with tidal streams. *MNRAS*, 332(4):915–920.

Ibata, R. A., Wyse, R. F. G., Gilmore, G., Irwin, M. J., and Suntzeff, N. B. (1997). The Kinematics, Orbit, and Survival of the Sagittarius Dwarf Spheroidal Galaxy. *AJ*, 113:634–655.

Iorio, G. and Belokurov, V. (2018). The shape of the Galactic halo with Gaia DR2 RR

Lyrae. Anatomy of an ancient major merger. *Monthly Notices of the Royal Astronomical Society*, 482(3):3868–3879.

Ivezić, Ž., *et al.* (2008). LSST: from Science Drivers to Reference Design and Anticipated Data Products. *ArXiv e-prints*.

Ivezić, Ž., Beers, T. C., and Jurić, M. (2012). Galactic Stellar Populations in the Era of the Sloan Digital Sky Survey and Other Large Surveys. **??***jnlARA&A*, 50:251–304.

Jacyszyn-Dobrzeniecka, A. M., Skowron, D. M., Mróz, P., Soszyński, I., Udalski, A., Pietrukowicz, P., Skowron, J., Poleski, R., Kozłowski, S., Wyrzykowski, Ł., Pawlak, M., Szymański, M. K., and Ulaczyk, K. (2017). OGLE-ing the Magellanic System: Three-Dimensional Structure of the Clouds and the Bridge using RR Lyrae Stars. *Acta Astron.*, 67(1):1–35.

Jeon, Y.-B., Ngeow, C.-C., and Nemec, J. M. (2014). Ground-based photometry for 42 Kepler-field RR Lyrae stars. In Guzik, J. A., Chaplin, W. J., Handler, G., and Pigulski, A., editors, *Precision Asteroseismology*, volume 301 of *IAU Symposium*, pages 427–428.

Jethwa, P., Erkal, D., and Belokurov, V. (2016). A Magellanic origin of the DES dwarfs. *MNRAS*, 461(2):2212–2233.

Jethwa, P., Torrealba, G., Navarrete, C., Carballo-Bello, J. A., de Boer, T., Erkal, D., Koposov, S. E., Duffau, S., Geisler, D., Catelan, M., and Belokurov, V. (2018). Discovery of a thin stellar stream in the SLAMS survey. *MNRAS*, 480(4):5342–5351.

Ji, A. P., Li, T. S., Hansen, T. T., Casey, A. R., Koposov, S. E., Pace, A. B., Mackey, D., Lewis, G. F., Simpson, J. D., Bland-Hawthorn, J., Cullinane, L. R., Da Costa, G. S., Hattori, K., Martell, S. L., Kuehn, K., Erkal, D., Shipp, N., Wan, Z., and Zucker, D. B. (2020). The Southern Stellar Stream Spectroscopic Survey (S^5): Chemical Abundances of Seven Stellar Streams. *AJ*, 160(4):181.

Johnston, K. V., Sackett, P. D., and Bullock, J. S. (2001). Interpreting Debris from Satellite Disruption in External Galaxies. *ApJ*, 557(1):137–149.

Johnston, K. V., Spergel, D. N., and Haydn, C. (2002). How Lumpy Is the Milky Way's

Dark Matter Halo? *ApJ*, 570(2):656–664.

Johnston, K. V., Spergel, D. N., and Hernquist, L. (1995). The Disruption of the Sagittarius Dwarf Galaxy. *ApJ*, 451:598.

Johnston, K. V., Zhao, H., Spergel, D. N., and Hernquist, L. (1999). Tidal Streams as Probes of the Galactic Potential. *ApJ*, 512(2):L109–L112.

Jones, E., Oliphant, T., Peterson, P., et al. (2001). SciPy: Open source scientific tools for Python.

Jurcsik, J. (1995). Revision of the [Fe/H] Scales Used for Globular Clusters and RR Lyrae Variables. *Acta Astron.*, 45:653–660.

Kaiser, N., *et al.* (2002). Pan-STARRS: A Large Synoptic Survey Telescope Array. volume 4836 of *Proc. SPIE*, pages 154–164.

Kallivayalil, N., van der Marel, R. P., Besla, G., Anderson, J., and Alcock, C. (2013). Third-epoch Magellanic Cloud Proper Motions. I. Hubble Space Telescope/WFC3 Data and Orbit Implications. *ApJ*, 764(2):161.

Kapakos, E., Hatzidimitriou, D., and Soszyński, I. (2011). RR Lyrae variables in the Small Magellanic Cloud - I. The central region. *MNRAS*, 415(2):1366–1380.

Kaplinghat, M., Tulin, S., and Yu, H.-B. (2016). Dark matter halos as particle colliders: Unified solution to small-scale structure puzzles from dwarfs to clusters. *Phys. Rev. Lett.*, 116:041302.

Kesden, M. and Kamionkowski, M. (2006). Tidal tails test the equivalence principle in the dark-matter sector. *Phys. Rev. D*, 74(8):083007.

Koposov, S. E., Belokurov, V., Evans, N. W., Gilmore, G., Gieles, M., Irwin, M. J., Lewis, G. F., Niederste-Ostholt, M., Peñarrubia, J., and Smith, M. C. (2012). The Sagittarius Streams in the Southern Galactic Hemisphere. *ApJ*, 750(1):80.

Koposov, S. E., Belokurov, V., Li, T. S., Mateu, C., Erkal, D., Grillmair, C. J., Hendel, D., Price-Whelan, A. M., Laporte, C. F. P., Hawkins, K., Sohn, S. T., del Pino, A., Evans, N. W., Slater, C. T., Kallivayalil, N., Navarro, J. F., and Orphan Aspen Treasury

Collaboration (2019). Piercing the Milky Way: an all-sky view of the Orphan Stream. *MNRAS*, 485(4):4726–4742.

Koposov, S. E., Irwin, M., Belokurov, V., Gonzalez-Solares, E., Yoldas, A. K., Lewis, J., Metcalfe, N., and Shanks, T. (2014). Discovery of a cold stellar stream in the ATLAS DR1 data. *MNRAS*, 442:L85–L89.

Koposov, S. E., Rix, H.-W., and Hogg, D. W. (2010). Constraining the Milky Way Potential with a Six-Dimensional Phase-Space Map of the GD-1 Stellar Stream. *ApJ*, 712(1):260–273.

Kruijssen, J. M. D. (2008). Explaining the mass-to-light ratios of globular clusters. *A&A*, 486(3):L21–L24.

Kuhlen, M., Diemand, J., and Madau, P. (2007). The Shapes, Orientation, and Alignment of Galactic Dark Matter Subhalos. *ApJ*, 671(2):1135–1146.

Law, D. R. and Majewski, S. R. (2010a). The Sagittarius Dwarf Galaxy: A Model for Evolution in a Triaxial Milky Way Halo. *ApJ*, 714(1):229–254.

Law, D. R. and Majewski, S. R. (2010b). The Sagittarius Dwarf Galaxy: A Model for Evolution in a Triaxial Milky Way Halo. *ApJ*, 714(1):229–254.

Law, N. M., *et al.* (2009). The Palomar Transient Factory: System Overview, Performance, and First Results. *PASP*, 121:1395.

Li, T. S., *et al.* (2016). Assessment of Systematic Chromatic Errors that Impact Sub-1% Photometric Precision in Large-area Sky Surveys. *ApJ*, 151:157.

Li, T., DePoy, D. L., Kessler, R., Burke, D. L., Marshall, J. L., Wise, J., Rheault, J. P., Carona, D. W., Boada, S., Prochaska, T., and Allen, R. (2016). aTmcam: A Simple Atmospheric Transmission Monitoring Camera For Sub 1 Percent Photometric Precision. In Deustua, S., Allam, S., Tucker, D., and Smith, J. A., editors, *The Science of Calibration*, volume 503 of *Astronomical Society of the Pacific Conference Series*, page 25.

Li, T. S., Koposov, S. E., Erkal, D., Ji, A. P., Shipp, N., Pace, A. B., Hilmi, T., Kuehn, K., Lewis, G. F., Mackey, D., Simpson, J. D., Wan, Z., Zucker, D. B., Bland-Hawthorn,

J., Cullinane, L. R., Da Costa, G. S., Drlica-Wagner, A., Hattori, K., Martell, S. L., and Sharma, S. (2020). Broken into Pieces: ATLAS and Aliqa Uma as One Single Stream. *arXiv e-prints*, page arXiv:2006.10763.

Li, T. S., Koposov, S. E., Zucker, D. B., Lewis, G. F., Kuehn, K., Simpson, J. D., Ji, A. P., Shipp, N., Mao, Y. Y., Geha, M., Pace, A. B., Mackey, A. D., Allam, S., Tucker, D. L., Da Costa, G. S., Erkal, D., Simon, J. D., Mould, J. R., Martell, S. L., Wan, Z., De Silva, G. M., Bechtol, K., Balbinot, E., Belokurov, V., Bland-Hawthorn, J., Casey, A. R., Cullinane, L., Drlica-Wagner, A., Sharma, S., Vivas, A. K., Wechsler, R. H., Yanny, B., and S5 Collaboration (2019). The southern stellar stream spectroscopic survey (S^5): Overview, target selection, data reduction, validation, and early science. *MNRAS*, 490(3):3508–3531.

Li, T. S., Simon, J. D., Kuehn, K., Pace, A. B., Erkal, D., Bechtol, K., Yanny, B., Drlica-Wagner, A., Marshall, J. L., Lidman, C., Balbinot, E., Carollo, D., Jenkins, S., Martínez-Vázquez, C. E., Shipp, N., Stringer, K. M., Vivas, A. K., Walker, A. R., Wechsler, R. H., Abdalla, F. B., Allam, S., Annis, J., Avila, S., Bertin, E., Brooks, D., Buckley-Geer, E., Burke, D. L., Carnero Rosell, A., Carrasco Kind, M., Carretero, J., Cunha, C. E., D'Andrea, C. B., da Costa, L. N., Davis, C., De Vicente, J., Doel, P., Eifler, T. F., Evrard, A. E., Flaugher, B., Frieman, J., García-Bellido, J., Gaztanaga, E., Gerdes, D. W., Gruen, D., Gruendl, R. A., Gschwend, J., Gutierrez, G., Hartley, W. G., Hollowood, D. L., Honscheid, K., James, D. J., Krause, E., Maia, M. A. G., March, M., Menanteau, F., Miquel, R., Plazas, A. A., Sanchez, E., Santiago, B., Scarpine, V., Schindler, R., Schubnell, M., Sevilla-Noarbe, I., Smith, M., Smith, R. C., Soares-Santos, M., Sobreira, F., Suchyta, E., Swanson, M. E. C., Tarle, G., Tucker, D. L., and DES Collaboration (2018). The First Tidally Disrupted Ultra-faint Dwarf Galaxy?: A Spectroscopic Analysis of the Tucana III Stream. *ApJ*, 866(1):22.

Limbach, M. A., Schmidt, L. M., DePoy, D. L., Mason, J. C., Scobey, M., Brown, P., Taylor, C., and Marshall, J. L. (2020). The Exoplanet Transmission Spectroscopy Imager (ETSI). In *Society of Photo-Optical Instrumentation Engineers (SPIE) Conference Series*, volume

11447 of *Society of Photo-Optical Instrumentation Engineers (SPIE) Conference Series*, page 114477D.

Łokas, E. L., Kazantzidis, S., Majewski, S. R., Law, D. R., Mayer, L., and Frinchaboy, P. M. (2010). The Inner Structure and Kinematics of the Sagittarius Dwarf Galaxy as a Product of Tidal Stirring. *ApJ*, 725(2):1516–1527.

LSST Science Collaboration and Abell, P. A., *et al.* (2009). LSST Science Book, Version 2.0. *ArXiv*.

Lynden-Bell, D. and Lynden-Bell, R. M. (1995). Ghostly streams from the formation of the Galaxy's halo. *MNRAS*, 275(2):429–442.

Madore, B. F. (1976). A Reddening-independent Formulation of the Period-Luminosity Relation: the Wesenheit Function. In *The Galaxy and the Local Group*, volume 182, page 153.

Majewski, S. R., Hasselquist, S., Łokas, E. L., Nidever, D. L., Frinchaboy, P. M., García Pérez, A. E., Johnston, K. V., Mészáros, S., Shetrone, M., Allende Prieto, C., Beaton, R. L., Beers, T. C., Bizyaev, D., Cunha, K., Damke, G., Ebelke, G., Eisenstein, D. J., Hearty, F., Holtzman, J., Johnson, J. A., Law, D. R., Malanushenko, V., Malanushenko, E., O'Connell, R. W., Oravetz, D., Pan, K., Schiavon, R. P., Schneider, D. P., Simmons, A., Skrutskie, M. F., Smith, V. V., Wilson, J. C., and Zasowski, G. (2013). Discovery of a Dynamical Cold Point in the Heart of the Sagittarius dSph Galaxy with Observations from the APOGEE Project. *ApJ*, 777:L13.

Majewski, S. R., Schiavon, R. P., Frinchaboy, P. M., Allende Prieto, C., Barkhouser, R., Bizyaev, D., Blank, B., Brunner, S., Burton, A., Carrera, R., Chojnowski, S. D., Cunha, K., Epstein, C., Fitzgerald, G., García Pérez, A. E., Hearty, F. R., Henderson, C., Holtzman, J. A., Johnson, J. A., Lam, C. R., Lawler, J. E., Maseman, P., Mészáros, S., Nelson, M., Nguyen, D. C., Nidever, D. L., Pinsonneault, M., Shetrone, M., Smee, S., Smith, V. V., Stolberg, T., Skrutskie, M. F., Walker, E., Wilson, J. C., Zasowski, G., Anders, F., Basu, S., Beland, S., Blanton, M. R., Bovy, J., Brownstein, J. R., Carlberg, J., Chaplin, W.,

Chiappini, C., Eisenstein, D. J., Elsworth, Y., Feuillet, D., Fleming, S. W., Galbraith-Frew, J., García, R. A., García-Hernández, D. A., Gillespie, B. A., Girardi, L., Gunn, J. E., Hasselquist, S., Hayden, M. R., Hekker, S., Ivans, I., Kinemuchi, K., Klaene, M., Mahadevan, S., Mathur, S., Mosser, B., Muna, D., Munn, J. A., Nichol, R. C., O'Connell, R. W., Parejko, J. K., Robin, A. C., Rocha-Pinto, H., Schultheis, M., Serenelli, A. M., Shane, N., Silva Aguirre, V., Sobeck, J. S., Thompson, B., Troup, N. W., Weinberg, D. H., and Zamora, O. (2017). The Apache Point Observatory Galactic Evolution Experiment (APOGEE). *AJ*, 154(3):94.

Majewski, S. R., Skrutskie, M. F., Weinberg, M. D., and Ostheimer, J. C. (2003a). A Two Micron All Sky Survey View of the Sagittarius Dwarf Galaxy. I. Morphology of the Sagittarius Core and Tidal Arms. *ApJ*, 599(2):1082–1115.

Majewski, S. R., Skrutskie, M. F., Weinberg, M. D., and Ostheimer, J. C. (2003b). A Two Micron All Sky Survey View of the Sagittarius Dwarf Galaxy. I. Morphology of the Sagittarius Core and Tidal Arms. *ApJ*, 599(2):1082–1115.

Malhan, K. and Ibata, R. A. (2018). STREAMFINDER - I. A new algorithm for detecting stellar streams. *MNRAS*, 477(3):4063–4076.

Malhan, K., Ibata, R. A., and Martin, N. F. (2018). Ghostly tributaries to the Milky Way: charting the halo's stellar streams with the Gaia DR2 catalogue. *MNRAS*, 481(3):3442–3455.

Marshall, J. L., *et al.* (2016). DECal: A Spectrophotometric Calibration System for DECam. volume 503 of *ASPC*, page 49.

Marshall, J. L. and DePoy, D. L. (2013). Flattening scientific ccd imaging data with a dome flat-field system. *PASP*, 125:932.

Mau, S., Cerny, W., Pace, A. B., Choi, Y., Drlica-Wagner, A., Santana-Silva, L., Riley, A. H., Erkal, D., Stringfellow, G. S., Adamów, M., Carlin, J. L., Gruendl, R. A., Hernandez-Lang, D., Kuropatkin, N., Li, T. S., Martínez-Vázquez, C. E., Morganson, E., Mutlu-Pakdil, B., Neilsen, E. H., Nidever, D. L., Olsen, K. A. G., Sand, D. J., Tollerud, E. J., Tucker, D. L.,

Yanny, B., Zenteno, A., Allam, S., Barkhouse, W. A., Bechtol, K., Bell, E. F., Balaji, P., Crnojević, D., Esteves, J., Ferguson, P. S., Gallart, C., Hughes, A. K., James, D. J., Jethwa, P., Johnson, L. C., Kuehn, K., Majewski, S., Mao, Y. Y., Massana, P., McNanna, M., Monachesi, A., Nadler, E. O., Noël, N. E. D., Palmese, A., Paz-Chinchon, F., Pieres, A., Sanchez, J., Shipp, N., Simon, J. D., Soares-Santos, M., Tavangar, K., van der Marel, R. P., Vivas, A. K., Walker, A. R., and Wechsler, R. H. (2020). Two Ultra-faint Milky Way Stellar Systems Discovered in Early Data from the DECam Local Volume Exploration Survey. *ApJ*, 890(2):136.

McConnachie, A. W. (2012). The Observed Properties of Dwarf Galaxies in and around the Local Group. *AJ*, 144(1):4.

McMillan, P. J. (2017). The mass distribution and gravitational potential of the Milky Way. *MNRAS*, 465:76–94.

Mitteldorf, J. J. and Landon, D. O. (1968). Multiply diffracted light in the czerny-turner spectrometer. *Appl. Opt.*, 7(8):1431–1435.

Miyamoto, M. and Nagai, R. (1975). Three-dimensional models for the distribution of mass in galaxies. *Publications of the Astronomical Society of Japan*, 27:533–543.

Morganson, E., Gruendl, R. A., Menanteau, F., Carrasco Kind, M., Chen, Y. C., Daues, G., Drlica-Wagner, A., Friedel, D. N., Gower, M., Johnson, M. W. G., Johnson, M. D., Kessler, R., Paz-Chinchón, F., Petravick, D., Pond, C., Yanny, B., Allam, S., Armstrong, R., Barkhouse, W., Bechtol, K., Benoit-Lévy, A., Bernstein, G. M., Bertin, E., Buckley-Geer, E., Covarrubias, R., Desai, S., Diehl, H. T., Goldstein, D. A., Gruen, D., Li, T. S., Lin, H., Marriner, J., Mohr, J. J., Neilsen, E., Ngeow, C. C., Paech, K., Rykoff, E. S., Sako, M., Sevilla-Noarbe, I., Sheldon, E., Sobreira, F., Tucker, D. L., Wester, W., and DES Collaboration (2018). The Dark Energy Survey Image Processing Pipeline. **??***jnlPASP*, 130(989):074501.

Nadler, E. O., Drlica-Wagner, A., Bechtol, K., Mau, S., Wechsler, R. H., Gluscevic, V., Boddy, K., Pace, A. B., Li, T. S., McNanna, M., Riley, A. H., García-Bellido, J., Mao,

Y. Y., Green, G., Burke, D. L., Peter, A., Jain, B., Abbott, T. M. C., Aguena, M., Allam, S., Annis, J., Avila, S., Brooks, D., Carrasco Kind, M., Carretero, J., Costanzi, M., da Costa, L. N., De Vicente, J., Desai, S., Diehl, H. T., Doel, P., Everett, S., Evrard, A. E., Flaugher, B., Frieman, J., Gerdes, D. W., Gruen, D., Gruendl, R. A., Gschwend, J., Gutierrez, G., Hinton, S. R., Honscheid, K., Huterer, D., James, D. J., Krause, E., Kuehn, K., Kuropatkin, N., Lahav, O., Maia, M. A. G., Marshall, J. L., Menanteau, F., Miquel, R., Palmese, A., Paz-Chinchón, F., Plazas, A. A., Romer, A. K., Sanchez, E., Scarpine, V., Serrano, S., Sevilla-Noarbe, I., Smith, M., Soares-Santos, M., Suchyta, E., Swanson, M. E. C., Tarle, G., Tucker, D. L., Walker, A. R., Wester, W., and DES Collaboration (2021). Constraints on Dark Matter Properties from Observations of Milky Way Satellite Galaxies. **??***jnlPhRvL*, 126(9):091101.

Naidu, R. P., Conroy, C., Bonaca, A., Johnson, B. D., Ting, Y.-S., Caldwell, N., Zaritsky, D., and Cargile, P. A. (2020). Evidence from the H3 Survey That the Stellar Halo Is Entirely Comprised of Substructure. *ApJ*, 901(1):48.

Neilsen, E., Bernstein, G., Gruendl, R., and Kent, S. (2015). "limiting magnitude, τ, t_{eff}, and image quality in des year 1". Technical Report FERMILAB-TM-2610-AE-CD.

Nemec, J. M., Cohen, J. G., Ripepi, V., Derekas, A., Moskalik, P., Sesar, B., Chadid, M., and Bruntt, H. (2013). Metal Abundances, Radial Velocities, and Other Physical Characteristics for the RR Lyrae Stars in The Kepler Field. *ApJ*, 773(2):181.

Newberg, H. J. and Carlin, J. L. (2016). *Tidal Streams in the Local Group and Beyond*, volume 420. Springer.

Niederste-Ostholt, M., Belokurov, V., Evans, N. W., and Peñarrubia, J. (2010). Re-Assembling the Sagittarius Dwarf Galaxy. *ApJ*, 712(1):516–526.

Odenkirchen, M., Grebel, E. K., Rockosi, C. M., Dehnen, W., Ibata, R., Rix, H.-W., Stolte, A., Wolf, C., Anderson, John E., J., Bahcall, N. A., Brinkmann, J., Csabai, I., Hennessy, G., Hindsley, R. B., Ivezić, Ž., Lupton, R. H., Munn, J. A., Pier, J. R., Stoughton, C., and York, D. G. (2001). Detection of Massive Tidal Tails around the Globular Cluster

Palomar 5 with Sloan Digital Sky Survey Commissioning Data. *ApJ*, 548(2):L165–L169.

Pace, A. B. and Li, T. S. (2019). Proper Motions of Milky Way Ultra-faint Satellites with Gaia DR2 × DES DR1. *ApJ*, 875(1):77.

pandas development team, T. (2020). pandas-dev/pandas: Pandas.

Peñarrubia, J., Zucker, D. B., Irwin, M. J., Hyde, E. A., Lane, R. R., Lewis, G. F., Gilmore, G., Evans, N. W., and Belokurov, V. (2011). No Evidence for Internal Rotation in the Remnant Core of the Sagittarius Dwarf. *ApJ*, 727(1):L2.

Pearson, S., Price-Whelan, A. M., and Johnston, K. V. (2017). Gaps and length asymmetry in the stellar stream Palomar 5 as effects of Galactic bar rotation. *Nature Astronomy*, 1:633–639.

Penchina, C. M. (1967). Reduction of stray light in in-plane grating spectrometers. *Appl. Opt.*, 6(6):1029–1031.

Pietrzyński, G., Graczyk, D., Gieren, W., Thompson, I. B., Pilecki, B., Udalski, A., Soszyński, I., Kozłowski, S., Konorski, P., Suchomska, K., Bono, G., Moroni, P. G. P., Villanova, S., Nardetto, N., Bresolin, F., Kudritzki, R. P., Storm, J., Gallenne, A., Smolec, R., Minniti, D., Kubiak, M., Szymański, M. K., Poleski, R., Wyrzykowski, Ł., Ulaczyk, K., Pietrukowicz, P., Górski, M., and Karczmarek, P. (2013). An eclipsing-binary distance to the Large Magellanic Cloud accurate to two per cent. **??***jnlNature*, 495(7439):76–79.

Planck Collaboration, Aghanim, N., Akrami, Y., Ashdown, M., Aumont, J., Baccigalupi, C., Ballardini, M., Banday, A. J., Barreiro, R. B., Bartolo, N., Basak, S., Battye, R., Benabed, K., Bernard, J. P., Bersanelli, M., Bielewicz, P., Bock, J. J., Bond, J. R., Borrill, J., Bouchet, F. R., Boulanger, F., Bucher, M., Burigana, C., Butler, R. C., Calabrese, E., Cardoso, J. F., Carron, J., Challinor, A., Chiang, H. C., Chluba, J., Colombo, L. P. L., Combet, C., Contreras, D., Crill, B. P., Cuttaia, F., de Bernardis, P., de Zotti, G., Delabrouille, J., Delouis, J. M., Di Valentino, E., Diego, J. M., Doré, O., Douspis, M., Ducout, A., Dupac, X., Dusini, S., Efstathiou, G., Elsner, F., Enßlin, T. A., Eriksen, H. K., Fantaye, Y., Farhang, M., Fergusson, J., Fernandez-Cobos, R., Finelli, F.,

Forastieri, F., Frailis, M., Fraisse, A. A., Franceschi, E., Frolov, A., Galeotta, S., Galli, S., Ganga, K., Génova-Santos, R. T., Gerbino, M., Ghosh, T., González-Nuevo, J., Górski, K. M., Gratton, S., Gruppuso, A., Gudmundsson, J. E., Hamann, J., Handley, W., Hansen, F. K., Herranz, D., Hildebrandt, S. R., Hivon, E., Huang, Z., Jaffe, A. H., Jones, W. C., Karakci, A., Keihänen, E., Keskitalo, R., Kiiveri, K., Kim, J., Kisner, T. S., Knox, L., Krachmalnicoff, N., Kunz, M., Kurki-Suonio, H., Lagache, G., Lamarre, J. M., Lasenby, A., Lattanzi, M., Lawrence, C. R., Le Jeune, M., Lemos, P., Lesgourgues, J., Levrier, F., Lewis, A., Liguori, M., Lilje, P. B., Lilley, M., Lindholm, V., López-Caniego, M., Lubin, P. M., Ma, Y. Z., Macías-Pérez, J. F., Maggio, G., Maino, D., Mandolesi, N., Mangilli, A., Marcos-Caballero, A., Maris, M., Martin, P. G., Martinelli, M., Martínez-González, E., Matarrese, S., Mauri, N., McEwen, J. D., Meinhold, P. R., Melchiorri, A., Mennella, A., Migliaccio, M., Millea, M., Mitra, S., Miville-Deschênes, M. A., Molinari, D., Montier, L., Morgante, G., Moss, A., Natoli, P., Nørgaard-Nielsen, H. U., Pagano, L., Paoletti, D., Partridge, B., Patanchon, G., Peiris, H. V., Perrotta, F., Pettorino, V., Piacentini, F., Polastri, L., Polenta, G., Puget, J. L., Rachen, J. P., Reinecke, M., Remazeilles, M., Renzi, A., Rocha, G., Rosset, C., Roudier, G., Rubiño-Martín, J. A., Ruiz-Granados, B., Salvati, L., Sandri, M., Savelainen, M., Scott, D., Shellard, E. P. S., Sirignano, C., Sirri, G., Spencer, L. D., Sunyaev, R., Suur-Uski, A. S., Tauber, J. A., Tavagnacco, D., Tenti, M., Toffolatti, L., Tomasi, M., Trombetti, T., Valenziano, L., Valiviita, J., Van Tent, B., Vibert, L., Vielva, P., Villa, F., Vittorio, N., Wandelt, B. D., Wehus, I. K., White, M., White, S. D. M., Zacchei, A., and Zonca, A. (2020). Planck 2018 results. VI. Cosmological parameters. *A&A*, 641:A6.

Plummer, H. C. (1911). On the problem of distribution in globular star clusters. *MNRAS*, 71:460–470.

Press, W. H. and Schechter, P. (1974). Formation of Galaxies and Clusters of Galaxies by Self-Similar Gravitational Condensation. *ApJ*, 187:425–438.

Price-Whelan, A. M. and Bonaca, A. (2018). Off the Beaten Path: Gaia Reveals GD-1 Stars

outside of the Main Stream. *ApJ*, 863(2):L20.

Price-Whelan, A. M., Sipőcz, B. M., Günther, H. M., Lim, P. L., Crawford, S. M., Conseil, S., Shupe, D. L., Craig, M. W., Dencheva, N., Ginsburg, A., VanderPlas, J. T., Bradley, L. D., Pérez-Suárez, D., de Val-Borro, M., Paper Contributors, P., Aldcroft, T. L., Cruz, K. L., Robitaille, T. P., Tollerud, E. J., Coordination Committee, A., Ardelean, C., Babej, T., Bach, Y. P., Bachetti, M., Bakanov, A. V., Bamford, S. P., Barentsen, G., Barmby, P., Baumbach, A., Berry, K. L., Biscani, F., Boquien, M., Bostroem, K. A., Bouma, L. G., Brammer, G. B., Bray, E. M., Breytenbach, H., Buddelmeijer, H., Burke, D. J., Calderone, G., Cano Rodríguez, J. L., Cara, M., Cardoso, J. V. M., Cheedella, S., Copin, Y., Corrales, L., Crichton, D., D'Avella, D., Deil, C., Depagne, É., Dietrich, J. P., Donath, A., Droettboom, M., Earl, N., Erben, T., Fabbro, S., Ferreira, L. A., Finethy, T., Fox, R. T., Garrison, L. H., Gibbons, S. L. J., Goldstein, D. A., Gommers, R., Greco, J. P., Greenfield, P., Groener, A. M., Grollier, F., Hagen, A., Hirst, P., Homeier, D., Horton, A. J., Hosseinzadeh, G., Hu, L., Hunkeler, J. S., Ivezić, Ž., Jain, A., Jenness, T., Kanarek, G., Kendrew, S., Kern, N. S., Kerzendorf, W. E., Khvalko, A., King, J., Kirkby, D., Kulkarni, A. M., Kumar, A., Lee, A., Lenz, D., Littlefair, S. P., Ma, Z., Macleod, D. M., Mastropietro, M., McCully, C., Montagnac, S., Morris, B. M., Mueller, M., Mumford, S. J., Muna, D., Murphy, N. A., Nelson, S., Nguyen, G. H., Ninan, J. P., Nöthe, M., Ogaz, S., Oh, S., Parejko, J. K., Parley, N., Pascual, S., Patil, R., Patil, A. A., Plunkett, A. L., Prochaska, J. X., Rastogi, T., Reddy Janga, V., Sabater, J., Sakurikar, P., Seifert, M., Sherbert, L. E., Sherwood-Taylor, H., Shih, A. Y., Sick, J., Silbiger, M. T., Singanamalla, S., Singer, L. P., Sladen, P. H., Sooley, K. A., Sornarajah, S., Streicher, O., Teuben, P., Thomas, S. W., Tremblay, G. R., Turner, J. E. H., Terrón, V., van Kerkwijk, M. H., de la Vega, A., Watkins, L. L., Weaver, B. A., Whitmore, J. B., Woillez, J., Zabalza, V., and Contributors, A. (2018). The Astropy Project: Building an Open-science Project and Status of the v2.0 Core Package. *AJ*, 156:123.

Rheault, J.-P., *et al.* (2010). Spectrophotometric calibration system for DECam. volume

7735 of *Proc. SPIE*, page 773564.

Rheault, J.-P., *et al.* (2012). Spectrophotometric calibration system for DECam. volume 8446 of *Proc. SPIE*, page 84466M.

Rheault, J.-P., *et al.* (2014). Spectrophotometric calibration of the Swope and duPont telescopes for the Carnegie s@INPROCEEDINGSSchmidt:2018, author = Schmidt, Luke M. and Gomez, Madelynn and Kim, Doyeon and Torregosa, Michael and Sauseda, Marcus and Prochaska, Travis and DePoy, D. L. and Marshall, J. L. and Gardner, Lawrence and Grant, Walter, title = "Characterization of the reflectivity of various white materials", booktitle = Advances in Optical and Mechanical Technologies for Telescopes and Instrumentation III, year = 2018, editor = Navarro, Ramón and Geyl, Roland, series = Society of Photo-Optical Instrumentation Engineers (SPIE) Conference Series, volume = 10706, month = jul, eid = 107065F, pages = 107065F, doi = 10.1117/12.2312365, adsurl = https://ui.adsabs.harvard.edu/abs/2018SPIE10706E..5FS, adsnote = Provided by the SAO/NASA Astrophysics Data System upernova project 2. volume 9147 of *Proc. SPIE*, page 91475L.

Richardson, T., Spolyar, D., and Lehnert, M. (2014). Plan β: Core or Cusp? *Mon. Not. Roy. Astron. Soc.*, 440(2):1680–1689.

Riello, M., De Angeli, F., Evans, D. W., Montegriffo, P., Carrasco, J. M., Busso, G., Palaversa, L., Burgess, P. W., Diener, C., Davidson, M., Rowell, N., Fabricius, C., Jordi, C., Bellazzini, M., Pancino, E., Harrison, D. L., Cacciari, C., van Leeuwen, F., Hambly, N. C., Hodgkin, S. T., Osborne, P. J., Altavilla, G., Barstow, M. A., Brown, A. G. A., Castellani, M., Cowell, S., De Luise, F., Gilmore, G., Giuffrida, G., Hidalgo, S., Holland, G., Marinoni, S., Pagani, C., Piersimoni, A. M., Pulone, L., Ragaini, S., Rainer, M., Richards, P. J., Sanna, N., Walton, N. A., Weiler, M., and Yoldas, A. (2020). Gaia Early Data Release 3: Photometric content and validation. *arXiv e-prints*, page arXiv:2012.01916.

Riess, A. G., Macri, L. M., Hoffmann, S. L., Scolnic, D., Casertano, S., Filippenko, A. V.,

Tucker, B. E., Reid, M. J., Jones, D. O., Silverman, J. M., Chornock, R., Challis, P., Yuan, W., Brown, P. J., and Foley, R. J. (2016). A 2.4% Determination of the Local Value of the Hubble Constant. *ApJ*, 826(1):56.

Sanders, J. L. and Binney, J. (2013). Stream-orbit misalignment - I. The dangers of orbit-fitting. *MNRAS*, 433(3):1813–1825.

Sanders, J. L. and Evans, N. W. (2017). The shapes and alignments of the satellites of the Milky Way and Andromeda. *MNRAS*, 472(3):2670–2685.

Schlafly, E. F. and Finkbeiner, D. P. (2011). Measuring Reddening with Sloan Digital Sky Survey Stellar Spectra and Recalibrating SFD. *ApJ*, 737:103.

Schlegel, D. J., Finkbeiner, D. P., and Davis, M. (1998). Maps of Dust Infrared Emission for Use in Estimation of Reddening and Cosmic Microwave Background Radiation Foregrounds. *ApJ*, 500:525–553.

Schmidt, L., *et al.* (2018). Characterization of the reflectivity of various white materials. Proc. SPIE, page in prep.

Schmidt, L. M., Gomez, M., Kim, D., Torregosa, M., Sauseda, M., Prochaska, T., DePoy, D. L., Marshall, J. L., Gardner, L., and Grant, W. (2018). Characterization of the reflectivity of various white materials. In Navarro, R. and Geyl, R., editors, *Advances in Optical and Mechanical Technologies for Telescopes and Instrumentation III*, volume 10706 of *Society of Photo-Optical Instrumentation Engineers (SPIE) Conference Series*, page 107065F.

Searle, L. and Zinn, R. (1978). Composition of halo clusters and the formation of the galactic halo. *ApJ*, 225:357–379.

Sesar, B., Hernitschek, N., Dierickx, M. I. P., Fardal, M. A., and Rix, H.-W. (2017). The >100 kpc Distant Spur of the Sagittarius Stream and the Outer Virgo Overdensity, as Seen in PS1 RR Lyrae Stars. *ApJ*, 844(1):L4.

Shi, X. and Fuller, G. M. (1999). New Dark Matter Candidate: Nonthermal Sterile Neutrinos. **??***jnlPhRvL*, 82(14):2832–2835.

Shipp, N., Drlica-Wagner, A., Balbinot, E., Ferguson, P., Erkal, D., Li, T. S., Bechtol, K., Belokurov, V., Buncher, B., Carollo, D., Carrasco Kind, M., Kuehn, K., Marshall, J. L., Pace, A. B., Rykoff, E. S., Sevilla-Noarbe, I., Sheldon, E., Strigari, L., Vivas, A. K., Yanny, B., Zenteno, A., Abbott, T. M. C., Abdalla, F. B., Allam, S., Avila, S., Bertin, E., Brooks, D., Burke, D. L., Carretero, J., Castander, F. J., Cawthon, R., Crocce, M., Cunha, C. E., D'Andrea, C. B., da Costa, L. N., Davis, C., De Vicente, J., Desai, S., Diehl, H. T., Doel, P., Evrard, A. E., Flaugher, B., Fosalba, P., Frieman, J., García-Bellido, J., Gaztanaga, E., Gerdes, D. W., Gruen, D., Gruendl, R. A., Gschwend, J., Gutierrez, G., Hartley, W., Honscheid, K., Hoyle, B., James, D. J., Johnson, M. D., Krause, E., Kuropatkin, N., Lahav, O., Lin, H., Maia, M. A. G., March, M., Martini, P., Menanteau, F., Miller, C. J., Miquel, R., Nichol, R. C., Plazas, A. A., Romer, A. K., Sako, M., Sanchez, E., Santiago, B., Scarpine, V., Schindler, R., Schubnell, M., Smith, M., Smith, R. C., Sobreira, F., Suchyta, E., Swanson, M. E. C., Tarle, G., Thomas, D., Tucker, D. L., Walker, A. R., Wechsler, R. H., and DES Collaboration (2018). Stellar Streams Discovered in the Dark Energy Survey. *ApJ*, 862:114.

Shipp, N., Erkal, D., Drlica-Wagner, A., et al. (2021). *in prep.*

Shipp, N., Li, T. S., Pace, A. B., Erkal, D., Drlica-Wagner, A., Yanny, B., Belokurov, V., Wester, W., Koposov, S. E., Kuehn, K., Lewis, G. F., Simpson, J. D., Wan, Z., Zucker, D. B., Martell, S. L., Wang, M. Y., and S5 Collaboration (2019). Proper Motions of Stellar Streams Discovered in the Dark Energy Survey. *ApJ*, 885(1):3.

Shipp, N., Price-Whelan, A. M., Tavangar, K., Mateu, C., and Drlica-Wagner, A. (2020). Discovery of Extended Tidal Tails around the Globular Cluster Palomar 13. *AJ*, 160(5):244.

Simon, J. D. (2019). The Faintest Dwarf Galaxies. **??***jnlARA&A*, 57:375–415.

Skowron, D. M., Soszyński, I., Udalski, A., Szymański, M. K., Pietrukowicz, P., Skowron, J., Poleski, R., Wyrzykowski, Ł., Ulaczyk, K., Kozłowski, S., Mróz, P., and Pawlak, M. (2016). OGLE-ing the Magellanic System: Photometric Metallicity from Fundamental Mode RR Lyrae Stars. *Acta Astron.*, 66(3):269–292.

Skrutskie, M. F., *et al.* (2006). The Two Micron All Sky Survey (2MASS). *ApJ*, 131:1163–1183.

Slater, C. T., Bell, E. F., Schlafly, E. F., Jurić, M., Martin, N. F., Rix, H. W., Bernard, E. J., Burgett, W. S., Chambers, K. C., and Finkbeiner, D. P. (2013). A Pan-STARRS1 View of the Bifurcated Sagittarius Stream. *ApJ*, 762(1):6.

Soszyński, I., Udalski, A., Szymański, M. K., Pietrukowicz, P., Mróz, P., Skowron, J., Kozłowski, S., Poleski, R., Skowron, D., Pietrzyński, G., Wyrzykowski, L., Ulaczyk, K., and Kubiak, M. (2014). Over 38000 RR Lyrae Stars in the OGLE Galactic Bulge Fields. *Acta Astron.*, 64:177–196.

Strigari, L. E., Frenk, C. S., and White, S. D. M. (2010). Kinematics of Milky Way satellites in a Lambda cold dark matter universe. *MNRAS*, 408(4):2364–2372.

The GPyOpt authors (2016). GPyOpt: A bayesian optimization framework in python. `http://github.com/SheffieldML/GPyOpt`.

Tonry, J. L., Denneau, L., Flewelling, H., Heinze, A. N., Onken, C. A., Smartt, S. J., Stalder, B., Weiland, H. J., and Wolf, C. (2018). The ATLAS All-Sky Stellar Reference Catalog. *ApJ*, 867:105.

Udalski, A., Szymański, M. K., and Szymański, G. (2015). OGLE-IV: Fourth Phase of the Optical Gravitational Lensing Experiment. *Acta Astron.*, 65(1):1–38.

van der Marel, R. P., Alves, D. R., Hardy, E., and Suntzeff, N. B. (2002). New Understanding of Large Magellanic Cloud Structure, Dynamics, and Orbit from Carbon Star Kinematics. *AJ*, 124(5):2639–2663.

van der Marel, R. P. and Cioni, M.-R. L. (2001). Magellanic Cloud Structure from Near-Infrared Surveys. I. The Viewing Angles of the Large Magellanic Cloud. *AJ*, 122(4):1807–1826.

van der Marel, R. P. and Kallivayalil, N. (2014). Third-epoch Magellanic Cloud Proper Motions. II. The Large Magellanic Cloud Rotation Field in Three Dimensions. *ApJ*, 781:121.

Van Der Walt, S., Colbert, S. C., and Varoquaux, G. (2011). The NumPy array: a structure for efficient numerical computation. *Computing in Science & Engineering*, 13:22–30.

Vasiliev, E. (2019). Proper motions and dynamics of the Milky Way globular cluster system from Gaia DR2. *MNRAS*, 484(2):2832–2850.

Vasiliev, E., Belokurov, V., and Erkal, D. (2021). Tango for three: Sagittarius, LMC, and the Milky Way. *MNRAS*, 501(2):2279–2304.

Wan, Z., Lewis, G. F., Li, T. S., Simpson, J. D., Martell, S. L., Zucker, D. B., Mould, J. R., Erkal, D., Pace, A. B., Mackey, D., Ji, A. P., Koposov, S. E., Kuehn, K., Shipp, N., Balbinot, E., Bland-Hawthorn, J., Casey, A. R., Da Costa, G. S., Kafle, P., Sharma, S., and De Silva, G. M. (2020). The tidal remnant of an unusually metal-poor globular cluster. **??***jnlNature*, 583(7818):768–770.

Wang, J., Bose, S., Frenk, C. S., Gao, L., Jenkins, A., Springel, V., and White, S. D. M. (2020). Universal structure of dark matter haloes over a mass range of 20 orders of magnitude. **??***jnlNature*, 585(7823):39–42.

Webb, J. J. and Bovy, J. (2019). Searching for the GD-1 stream progenitor in Gaia DR2 with direct N-body simulations. *MNRAS*, 485(4):5929–5938.

Weisz, D. and Boylan-Kolchin, M. (2019). Near-Field Cosmology with the Lowest-Mass Galaxies. **??***jnlBAAS*, 51(3):1.

Wes McKinney (2010). Data Structures for Statistical Computing in Python. In Stéfan van der Walt and Jarrod Millman, editors, *Proceedings of the 9th Python in Science Conference*, pages 56 – 61.

White, S. D. M. and Rees, M. J. (1978). Core condensation in heavy halos: a two-stage theory for galaxy formation and clustering. *MNRAS*, 183:341–358.

Wickham, H. (2016). *ggplot2: Elegant Graphics for Data Analysis*. Springer-Verlag New York.

Xu, W. L. and Randall, L. (2019). Testing ΛCDM With Dwarf Galaxy Morphology. *arXiv e-prints*, page arXiv:1904.08949.

York, D. G., *et al.* (2000). The Sloan Digital Sky Survey: Technical Summary. *ApJ*, 120:1579–1587.

APPENDIX A

A.1 *Gaia* Queries

Selection of all stars in region of the core of Sagittarius:

```
SELECT * FROM gaiaDR2.gaia_source
WHERE parallax < 1
AND ra > 278 AND ra < 290
AND dec < -28 AND dec > -33
```

Selection of RRab stars in the region of the core of Sagittarius:

```
SELECT *
FROM gaiaDR2.vari_rrlyrae AS rr
INNER JOIN gaiaDR2.gaia_source AS gaia
ON rr.source_id=gaia.source_id
    WHERE parallax < 1
    AND rr.best_classification='RRab'
    AND gaia.ra < 300 AND gaia.ra > 275
    AND gaia.dec < -18 AND gaia.dec > -40
```

APPENDIX B

B.1 Membership Probability

Table B.1 includes probable stream member stars with membership probability greater than 0.1 from the likelihood analysis described in Section 3.3.5.

Table B.1. this table includes all stars with $p_i > 0.1$ for our analysis of the proper motion of the Jet stream.
(This table is available in its entirety in machine-readable form.)
(a) DELVE ID's are from the `QUICK_OBJECT_ID` column in DELVE-DR1, and Gaia IDs are from `SOURCE_ID` column in *Gaia* EDR3.
(b) R.A. and Dec. are from Gaia EDR3 catalog (J2015.5 Epoch).
(c) g, r band magnitudes are reddening corrected PSF photometry (`MAG_PSF_DERED`) from DELVE DR1 catalog.
(d) The D_{ϕ_1} column gives the distance in kpc derived from equation 3.3, except for candidate bhb stars whose distances are estimated from their predicted absolute magnitude M_g as discussed in section 3.3.2 (e) The probability that a star is a member of the Jet stream.

ID (DELVE)[a]	ID (Gaia)[a]	R.A.[b] (deg)	Dec.[b] (deg)	g_0[c] (mag)	r_0[c] (mag)	$\mu_\alpha \cos\delta$ (mas/yr)	μ_δ (mas/yr)	D_{ϕ_1}[d] (kpc)	p_i[e]
10728500080043	3769884424255747584	147.84902	-10.82876	18.25	17.71	-1.25 ± 0.12	-1.56 ± 0.11	27.20	0.89 ± 0.10
10728500327498	3769898992784797696	147.99841	-10.58564	18.78	18.28	-0.21 ± 0.22	-1.81 ± 0.25	27.14	0.19 ± 0.13
10728500026630	3769900397239081472	148.34539	-10.75644	19.10	18.65	-0.92 ± 0.21	-2.20 ± 0.24	27.13	0.99 ± 0.00
10728500315132	3769918715274616320	148.13991	-10.57946	19.01	18.47	-1.43 ± 0.25	-1.43 ± 0.30	27.12	0.98 ± 0.02
10728500024967	3770009145810545664	148.73686	-10.33853	18.97	18.47	-1.13 ± 0.23	-2.04 ± 0.23	27.01	0.99 ± 0.00
10741200099637	5691172859402469376	147.03403	-12.15313	18.64	18.11	-0.75 ± 0.14	-2.39 ± 0.12	27.53	0.29 ± 0.18
10754000190703	5690650591379140608	145.22603	-13.49643	18.82	18.35	-1.38 ± 0.17	-1.93 ± 0.15	27.99	0.95 ± 0.06
10754000071117	5690723434024204288	146.34768	-13.10071	19.10	18.66	-0.96 ± 0.20	-1.55 ± 0.17	27.78	0.97 ± 0.03
10754000135902	5690754357789028352	146.29135	-12.69526	18.68	18.15	-0.61 ± 0.16	-1.65 ± 0.13	27.72	0.57 ± 0.20
10754000016678	5690813834496188416	145.60490	-12.65539	18.94	18.47	-1.11 ± 0.18	-1.64 ± 0.18	27.79	0.84 ± 0.10
10766700041815	5688839386491128832	144.97105	-14.55419	19.02	18.48	-0.66 ± 0.21	-1.21 ± 0.27	28.20	0.90 ± 0.05
10766700002702	5689006890215606272	144.34193	-14.21870	18.42	17.92	-1.28 ± 0.14	-1.72 ± 0.15	28.22	0.48 ± 0.21
10766700136724	5689088838191581184	144.96562	-13.90216	18.87	18.39	-1.17 ± 0.20	-1.96 ± 0.17	28.09	0.99 ± 0.00

Table B.1 (cont'd)

ID (DELVE)[a]	ID (Gaia)[a]	R.A.[b] (deg)	Dec.[b] (deg)	g_0[c] (mag)	r_0[c] (mag)	$\mu_\alpha \cos\delta$ (mas/yr)	μ_δ (mas/yr)	D_{ϕ_1}[d] (kpc)	p_i[e]
10766700035075	5689103269281880064	144.44651	-14.09401	18.62	18.13	-0.55 ± 0.15	-1.58 ± 0.14	28.19	0.66 ± 0.13
10779500052390	5688077390573231104	143.32846	-16.53625	19.12	18.63	-0.66 ± 0.28	-1.71 ± 0.33	28.77	0.99 ± 0.01
10779500005281	5688163358638977024	143.69278	-16.03945	18.07	17.50	-0.60 ± 0.11	-1.65 ± 0.11	28.63	0.98 ± 0.02
10779500058548	5688164973546700800	143.71670	-15.96170	18.56	18.03	-1.31 ± 0.14	-1.86 ± 0.14	28.61	0.58 ± 0.21
10779500116240	5688322581665456128	144.15994	-15.26023	18.56	18.05	-1.00 ± 0.15	-1.75 ± 0.16	28.43	1.00 ± 0.00
10779500125707	5688373708956744704	143.23721	-15.76513	18.84	18.33	-1.03 ± 0.18	-1.17 ± 0.17	28.64	0.25 ± 0.11
10779500135707	5688385670441143296	142.88390	-15.72215	18.66	18.08	-0.66 ± 0.14	-1.49 ± 0.10	28.68	0.14 ± 0.08
10779500145970	5688585777262317568	143.76531	-14.79803	18.87	18.40	-1.17 ± 0.20	-1.70 ± 0.22	28.40	0.92 ± 0.04
10792200059851	5681899921930767360	142.56282	-17.61680	18.55	18.06	-0.87 ± 0.17	-1.63 ± 0.15	29.06	0.99 ± 0.02
10792200057289	5681927237923304448	141.83396	-17.73566	18.46	17.94	-0.59 ± 0.14	-1.68 ± 0.12	29.17	0.96 ± 0.06
10792200060064	5681928925846183936	141.56627	-17.79131	17.73	17.18	-0.86 ± 0.08	-1.62 ± 0.09	29.22	0.67 ± 0.35
10792200170968	5682093882654153728	142.46540	-16.83792	18.69	18.14	-0.56 ± 0.18	-1.73 ± 0.15	28.93	0.99 ± 0.01
10792200156636	5682102408165005312	142.82850	-16.86320	18.07	17.51	-0.85 ± 0.10	-1.60 ± 0.06	28.89	1.00 ± 0.00

Table B.1 (cont'd)

ID (DELVE)[a]	ID (Gaia)[a]	R.A.[b] (deg)	Dec.[b] (deg)	g_0[c] (mag)	r_0[c] (mag)	$\mu_\alpha \cos\delta$ (mas/yr)	μ_δ (mas/yr)	D_{ϕ_1}[d] (kpc)	p_i[e]
10792200144735	5682103812619283456	142.75012	-16.80093	19.16	18.68	-0.36 ± 0.22	-2.08 ± 0.14	28.89	0.93 ± 0.04
10805000122022	5681400571853164544	140.73299	-18.62761	17.91	17.33	-0.67 ± 0.08	-1.52 ± 0.06	29.48	0.95 ± 0.04
10805000146842	5681565807835944960	141.41245	-17.80764	18.74	18.26	-0.47 ± 0.15	-1.42 ± 0.12	29.24	0.78 ± 0.09
10805100139444	5678846681220571136	142.25622	-18.25624	18.58	18.06	-0.42 ± 0.13	-1.56 ± 0.10	29.21	0.13 ± 0.11
10817700018781	5679651145774471168	139.72487	-20.11565	18.91	18.43	-1.17 ± 0.15	-2.18 ± 0.11	29.88	0.67 ± 0.11
10817700091324	5679772027630109696	140.04425	-19.65764	18.21	17.69	-0.66 ± 0.11	-1.39 ± 0.09	29.76	0.98 ± 0.01
10817700087087	5679780445765880832	140.38862	-19.66353	18.28	17.76	-0.70 ± 0.12	-1.50 ± 0.08	29.71	0.99 ± 0.01
10817800172384	5678275003892722688	141.12600	-19.57061	19.15	18.69	-0.43 ± 0.18	-1.75 ± 0.14	29.60	0.79 ± 0.09
10817800029289	5678288438550469632	140.64957	-19.48382	17.95	17.40	-0.68 ± 0.08	-1.57 ± 0.06	29.65	1.00 ± 0.00
10817800159599	5678465086261559296	141.77380	-18.46979	19.07	18.62	-0.49 ± 0.17	-1.21 ± 0.18	29.31	0.90 ± 0.05
10830600148522	5676595706040610816	139.42058	-20.76754	18.78	18.28	-0.84 ± 0.14	-1.42 ± 0.13	30.04	0.99 ± 0.00
10830600197552	5676595946558777344	139.38362	-20.76842	18.23	17.67	-0.85 ± 0.11	-1.47 ± 0.10	30.05	0.99 ± 0.01
10830600148645	5676602818506551296	139.58558	-20.70625	18.86	18.37	-0.64 ± 0.15	-1.36 ± 0.14	30.01	1.00 ± 0.00

Table B.1 (cont'd)

ID (DELVE)[a]	ID (Gaia)[a]	R.A.[b] (deg)	Dec.[b] (deg)	g_0[c] (mag)	r_0[c] (mag)	$\mu_\alpha \cos\delta$ (mas/yr)	μ_δ (mas/yr)	D_{ϕ_1}[d] (kpc)	p_i[e]
10830600102314	5676620238894112768	140.10936	-20.56687	17.66	17.09	-0.61 ± 0.07	-1.60 ± 0.06	29.92	1.00 ± 0.00
10830600172599	5676631234010499072	139.85125	-20.48700	18.21	17.66	-0.85 ± 0.10	-1.69 ± 0.08	29.94	0.99 ± 0.01
10830600051757	5676638075893485568	139.90801	-20.39132	19.07	18.62	-0.72 ± 0.19	-1.58 ± 0.13	29.91	1.00 ± 0.01
10830600136199	5676720500609427456	140.34750	-20.25480	17.69	17.12	-0.65 ± 0.07	-1.54 ± 0.06	29.83	1.00 ± 0.00
10830600151662	5676769566316783616	140.78179	-19.66060	18.73	18.19	-0.56 ± 0.13	-1.36 ± 0.09	29.66	0.43 ± 0.20
10843300004541	5676154904956396544	138.87976	-21.61947	18.07	17.53	-0.50 ± 0.10	-1.79 ± 0.08	30.27	0.88 ± 0.08
10843300194651	5676200465970655232	139.46576	-21.11660	18.36	17.83	-0.74 ± 0.12	-1.59 ± 0.11	30.10	1.00 ± 0.00
10856100104497	5651735851215925248	138.48348	-22.70527	19.10	18.65	-0.40 ± 0.21	-1.64 ± 0.16	30.53	0.71 ± 0.11
10856100035103	5651736675850326016	137.13799	-23.90559	18.82	18.31	-0.69 ± 0.18	-1.21 ± 0.18	30.94	0.99 ± 0.00
10856100056861	5651737912800928768	137.12391	-23.85192	17.86	17.31	-0.56 ± 0.09	-1.32 ± 0.10	30.93	1.00 ± 0.00
10856100145888	5651749908644837376	137.23166	-23.65347	19.01	18.49	-0.17 ± 0.22	-1.67 ± 0.19	30.88	0.63 ± 0.12
10856100139900	5651790689358588928	137.30615	-23.35828	19.19	18.68	-0.23 ± 0.20	-1.22 ± 0.18	30.81	0.95 ± 0.03
10856100098621	5651800726697629696	137.55560	-23.16100	18.77	18.27	-0.17 ± 0.18	-0.99 ± 0.16	30.74	0.57 ± 0.11

Table B.1 (cont'd)

ID (DELVE)[a]	ID (Gaia)[a]	R.A.[b] (deg)	Dec.[b] (deg)	g_0[c] (mag)	r_0[c] (mag)	$\mu_\alpha \cos\delta$ (mas/yr)	μ_δ (mas/yr)	D_{ϕ_1}[d] (kpc)	p_i[e]
10856100097840	5651895142962067456	137.69250	-23.07110	17.67	17.06	-0.48 ± 0.08	-1.42 ± 0.08	30.70	0.24 ± 0.26
10856100064940	5651897685582752768	137.68343	-23.02325	18.72	18.21	-0.49 ± 0.14	-1.39 ± 0.15	30.70	1.00 ± 0.00
10856100152737	5651906382893307904	137.95477	-22.80462	17.75	17.17	-0.74 ± 0.10	-1.49 ± 0.08	30.62	1.00 ± 0.00
10856100096593	5651949637507311616	137.52971	-22.87437	18.49	17.98	-0.56 ± 0.13	-1.40 ± 0.12	30.69	1.00 ± 0.00
10856100041762	5651957780765474816	137.66397	-22.71231	19.01	18.46	-0.49 ± 0.19	-1.33 ± 0.19	30.64	0.98 ± 0.01
10856100041806	5651959258234237952	137.68446	-22.69965	18.77	18.24	-0.18 ± 0.17	-1.04 ± 0.15	30.64	0.85 ± 0.06
10856100129410	5651960976222656512	137.57977	-22.68631	18.58	18.01	-0.37 ± 0.13	-1.14 ± 0.13	30.65	0.38 ± 0.13
10868800123221	5650984506817870848	135.78800	-25.29168	18.54	17.93	-0.54 ± 0.13	-1.72 ± 0.14	31.38	1.00 ± 0.00
10868800122682	5650990760288540672	136.17160	-25.15336	18.02	17.47	-0.48 ± 0.09	-1.60 ± 0.12	31.30	0.94 ± 0.06
10868800120938	5651018419878298624	136.24769	-24.95523	18.69	18.17	-0.20 ± 0.14	-1.79 ± 0.16	31.26	0.75 ± 0.10
10868800081002	5651134624513393664	136.62197	-24.49387	17.90	17.31	-0.63 ± 0.09	-1.45 ± 0.08	31.12	1.00 ± 0.00
10868800050093	5651184102536306688	135.96147	-25.02792	18.98	18.44	0.14 ± 0.18	-0.62 ± 0.18	31.31	0.20 ± 0.07
10868800047596	5651184858450643968	136.02881	-24.95434	17.59	16.98	-0.44 ± 0.07	-1.44 ± 0.09	31.29	1.00 ± 0.02

Table B.1 (cont'd)

ID (DELVE)[a]	ID (Gaia)[a]	R.A.[b] (deg)	Dec.[b] (deg)	g_0[c] (mag)	r_0[c] (mag)	$\mu_\alpha \cos\delta$ (mas/yr)	μ_δ (mas/yr)	D_{ϕ_1}[d] (kpc)	p_i[e]
10868800047225	5651185614364893184	135.92346	-24.94823	18.84	18.28	-0.76 ± 0.15	-1.89 ± 0.16	31.30	0.32 ± 0.12
10868800161219	5651202351854088192	135.82922	-24.79696	17.67	17.06	-0.74 ± 0.08	-1.36 ± 0.08	31.28	0.91 ± 0.08
10868800047403	5651212792918118400	135.97203	-24.84119	18.81	18.29	-0.86 ± 0.16	-1.19 ± 0.21	31.27	0.99 ± 0.01
10868800077734	5651321717585215488	136.39738	-24.38487	17.71	17.11	-0.57 ± 0.09	-1.35 ± 0.08	31.13	1.00 ± 0.00
10868800009221	5651324736945464320	136.59428	-24.32086	17.06	16.42	-0.58 ± 0.05	-1.46 ± 0.05	31.09	1.00 ± 0.00
10881600158462	5649409529426027520	135.97209	-25.83750	18.75	18.18	-0.45 ± 0.17	-1.10 ± 0.15	31.46	0.60 ± 0.14
10881600033437	5649439521182560256	135.09234	-25.86142	19.17	18.66	-0.41 ± 0.22	-0.89 ± 0.22	31.59	0.77 ± 0.09
10881600187420	5649439967859188736	135.19538	-25.81135	18.81	18.31	-0.58 ± 0.19	-1.50 ± 0.23	31.56	0.99 ± 0.00
10881600063209	5649482367775344640	135.69826	-25.40744	18.03	17.45	-0.54 ± 0.10	-1.41 ± 0.09	31.42	1.00 ± 0.00
10894300252770	5648727587403615232	133.38733	-27.83157	17.39	16.79	-0.24 ± 0.05	-1.26 ± 0.07	32.20	0.84 ± 0.18
10894300055651	5648919834437548032	134.38130	-26.69333	19.04	18.55	-0.40 ± 0.14	-1.76 ± 0.22	31.85	0.49 ± 0.13
10907100305896	5642463227288105984	132.37406	-29.59642	18.50	17.93	-0.37 ± 0.08	-1.13 ± 0.14	32.69	1.00 ± 0.00
10907100284243	5642475214532541440	132.10210	-29.57173	18.66	18.14	-0.56 ± 0.09	-1.38 ± 0.14	32.72	0.94 ± 0.05

Table B.1 (cont'd)

ID (DELVE)[a]	ID (Gaia)[a]	R.A.[b] (deg)	Dec.[b] (deg)	g_0[c] (mag)	r_0[c] (mag)	$\mu_\alpha \cos\delta$ (mas/yr)	μ_δ (mas/yr)	D_{ϕ_1}[d] (kpc)	p_i[e]
10907100070095	5642511193480231936	132.63307	-29.20267	17.86	17.25	-0.35 ± 0.05	-1.13 ± 0.07	32.57	1.00 ± 0.00
10907100279389	5642514247196083200	132.46072	-29.14657	19.06	18.60	-0.61 ± 0.11	-1.25 ± 0.15	32.59	0.98 ± 0.02
10907100353746	5642514350275323904	132.50197	-29.11790	18.41	17.88	-0.34 ± 0.07	-1.20 ± 0.10	32.58	1.00 ± 0.00
10907100155998	5642606056416819200	132.67916	-29.09299	18.85	18.37	-0.17 ± 0.10	-1.07 ± 0.15	32.55	0.99 ± 0.01
10907100260267	5642640381794764800	133.43070	-28.51812	18.95	18.47	-0.37 ± 0.14	-1.89 ± 0.19	32.33	0.91 ± 0.05
10907100295854	5642699759723975680	132.81360	-28.43379	18.02	17.44	-0.23 ± 0.07	-1.19 ± 0.09	32.40	0.15 ± 0.19
10919800455299	5641884742426066944	130.77321	-31.33790	18.80	18.27	-0.28 ± 0.11	-1.21 ± 0.15	33.26	0.99 ± 0.01
10919800325924	5642036681192404992	131.74834	-30.35556	18.63	18.11	-0.19 ± 0.09	-1.07 ± 0.13	32.92	1.00 ± 0.00
10919800056574	5642042900301821952	131.32278	-30.48572	18.88	18.30	0.11 ± 0.11	-0.98 ± 0.14	33.01	0.21 ± 0.11
10932700330110	5641156079756009472	131.64018	-31.10487	17.43	16.80	-0.40 ± 0.05	-1.14 ± 0.07	33.08	0.99 ± 0.01
10932700005905	5641162986066823168	131.63431	-30.89640	18.04	17.50	-0.32 ± 0.06	-1.13 ± 0.09	33.04	1.00 ± 0.00
10932700407608	5641176519502877696	131.42139	-30.91069	18.27	17.73	-0.08 ± 0.07	-0.88 ± 0.10	33.08	0.78 ± 0.18
10932700314117	5641281969537067008	131.73285	-30.58309	18.62	18.11	-0.39 ± 0.09	-1.22 ± 0.13	32.97	1.00 ± 0.00

Table B.1 (cont'd)

ID (DELVE)[a]	ID (Gaia)[a]	R.A.[b] (deg)	Dec.[b] (deg)	g_0[c] (mag)	r_0[c] (mag)	$\mu_\alpha \cos\delta$ (mas/yr)	μ_δ (mas/yr)	D_{ϕ_1}[d] (kpc)	p_i[e]
10932700093182	5641310458062931968	131.92667	-30.26418	18.87	18.31	-0.36 ± 0.11	-1.27 ± 0.15	32.88	1.00 ± 0.00
10932700224458	5641315921261763584	132.30975	-30.15848	18.91	18.36	-0.46 ± 0.10	-1.16 ± 0.16	32.81	0.99 ± 0.00
10945400248141	5639355560740634624	129.99009	-33.41154	18.77	18.28	-0.55 ± 0.12	-1.04 ± 0.15	33.77	0.97 ± 0.03
10945400457951	5639403213406989312	130.53367	-32.70052	19.09	18.62	-0.53 ± 0.17	-0.90 ± 0.26	33.55	0.95 ± 0.02
10945400274218	5639408990142212096	130.19938	-32.80797	18.92	18.35	-0.01 ± 0.13	-0.82 ± 0.24	33.62	0.98 ± 0.01
10945400035058	5639410566390705152	130.26241	-32.77440	18.84	18.30	-0.52 ± 0.14	-1.24 ± 0.22	33.61	1.00 ± 0.00
10945400311305	5639429498604271616	129.66127	-32.89064	18.75	18.18	-0.14 ± 0.10	-0.80 ± 0.14	33.72	0.49 ± 0.16
10945400186661	5639459155362115584	130.19103	-32.64570	18.94	18.40	0.06 ± 0.15	-0.62 ± 0.23	33.59	0.71 ± 0.14
10945400357058	5639552579489067008	130.91744	-32.00119	18.77	18.23	-0.07 ± 0.12	-1.22 ± 0.17	33.36	0.98 ± 0.02
10945400046366	5639557046247945216	131.14907	-31.92892	18.73	18.15	-0.27 ± 0.12	-1.11 ± 0.17	33.32	0.96 ± 0.02
10945400305604	5639570480908457984	130.38072	-32.15038	19.19	18.63	0.20 ± 0.16	-1.00 ± 0.22	33.47	0.48 ± 0.18
10945400286758	5639596559955088384	130.39932	-31.83393	18.94	18.46	0.17 ± 0.14	-1.22 ± 0.20	33.41	0.54 ± 0.14
10945400356917	5639598136199576576	130.84427	-32.01316	18.50	17.91	-0.63 ± 0.12	-1.40 ± 0.16	33.38	0.99 ± 0.01

Table B.1 (cont'd)

ID (DELVE)[a]	ID (Gaia)[a]	R.A.[b] (deg)	Dec.[b] (deg)	g_0[c] (mag)	r_0[c] (mag)	$\mu_\alpha \cos\delta$ (mas/yr)	μ_δ (mas/yr)	D_{ϕ_1}[d] (kpc)	p_i[e]
10945400303181	5639623051313760256	130.54443	-31.65325	18.52	17.98	-0.06 ± 0.10	-1.14 ± 0.13	33.35	0.16 ± 0.28
10945400403136	5639625353412084736	130.74206	-31.64510	18.64	18.13	-0.37 ± 0.10	-1.00 ± 0.13	33.32	1.00 ± 0.00
10958200198189	5638936303222245376	129.42081	-33.95916	18.01	17.44	0.00 ± 0.08	-1.09 ± 0.12	33.96	1.00 ± 0.00
10958200506638	5638944927506932736	129.60303	-33.79499	18.58	18.08	-0.31 ± 0.14	-1.67 ± 0.21	33.90	0.96 ± 0.04
10958200077581	5638966196188052480	129.72247	-33.71730	19.00	18.43	0.59 ± 0.15	-1.24 ± 0.22	33.87	0.65 ± 0.13
10741200132396	5691174268151734272	146.88439	-12.16936	17.63	17.78	-1.06 ± 0.10	-2.03 ± 0.09	26.87	1.00 ± 0.00
10741200094069	5691397709530736640	147.82855	-11.24442	17.63	17.74	-1.06 ± 0.12	-1.87 ± 0.10	27.35	1.00 ± 0.00
10766700149205	5688746649557013504	144.78809	-14.61022	17.71	17.77	-1.04 ± 0.13	-1.87 ± 0.12	28.70	1.00 ± 0.00
10766700048828	5688910339350307840	143.92770	-14.82403	18.31	18.47	-0.66 ± 0.18	-1.65 ± 0.20	36.69	0.99 ± 0.00
10779500047406	5688340414370036736	142.95519	-16.00187	17.73	17.85	-0.82 ± 0.12	-1.92 ± 0.10	28.47	0.99 ± 0.01
10792200117459	5682053205019695104	142.77460	-16.95514	17.81	17.96	-0.83 ± 0.12	-1.88 ± 0.08	29.27	1.00 ± 0.00
10805000144900	5681301821965646848	140.80869	-19.17199	17.83	17.95	-0.85 ± 0.10	-1.63 ± 0.07	29.82	1.00 ± 0.00
10817700035285	5679794047927322624	140.49243	-19.39604	17.84	17.97	-0.73 ± 0.11	-1.59 ± 0.08	29.86	1.00 ± 0.00

Table B.1 (cont'd)

ID (DELVE)[a]	ID (Gaia)[a]	R.A.[b] (deg)	Dec.[b] (deg)	g_0[c] (mag)	r_0[c] (mag)	$\mu_\alpha \cos\delta$ (mas/yr)	μ_δ (mas/yr)	D_{ϕ_1}[d] (kpc)	p_i[e]
10817800170691	5678332075418486784	141.28136	-18.97863	17.68	17.82	-0.80 ± 0.09	-1.51 ± 0.07	27.74	1.00 ± 0.00
10830600115073	5676577976415314944	139.56831	-20.94405	17.86	17.94	-0.47 ± 0.11	-1.45 ± 0.09	30.60	1.00 ± 0.00
10830600077722	5676619036303386624	139.95095	-20.47795	17.83	18.00	-0.83 ± 0.11	-1.52 ± 0.09	29.37	1.00 ± 0.00
10830600025097	5676733114929773568	140.49799	-20.02617	17.85	18.01	-0.86 ± 0.12	-1.64 ± 0.09	29.68	1.00 ± 0.00
10843300154577	5676011384329309184	138.85235	-21.82420	18.12	18.13	-0.83 ± 0.15	-0.92 ± 0.12	35.06	0.25 ± 0.10
10843300067527	5676205791730224128	139.35850	-20.99315	17.94	18.08	-0.81 ± 0.12	-1.43 ± 0.12	31.25	1.00 ± 0.00
10868800052554	5650977737949556736	136.20568	-25.24379	18.00	18.15	-0.46 ± 0.12	-1.42 ± 0.17	31.90	0.99 ± 0.00
10868800036875	5650984575537310720	135.84337	-25.30335	18.02	18.18	-0.36 ± 0.13	-1.24 ± 0.13	32.20	1.00 ± 0.00
10868800156976	5651126378176101376	136.49904	-24.61309	17.99	18.06	-0.33 ± 0.14	-1.38 ± 0.12	32.49	1.00 ± 0.00
10881600064547	5649665509476788224	135.28454	-25.43939	18.54	18.61	0.07 ± 0.21	-0.95 ± 0.19	41.92	0.45 ± 0.11
10894300275690	5648866366387045376	134.13125	-27.25206	18.07	18.17	-0.40 ± 0.10	-1.36 ± 0.12	33.50	1.00 ± 0.00
10907100156361	5642591934564324352	132.94125	-29.11109	18.24	18.34	-0.37 ± 0.11	-0.94 ± 0.15	36.10	0.99 ± 0.01
10919900174916	5641694256336070656	132.42002	-30.02954	18.18	18.30	-0.48 ± 0.10	-1.41 ± 0.15	34.93	0.99 ± 0.01

Table B.1 (cont'd)

ID (DELVE)[a]	ID (Gaia)[a]	R.A.[b] (deg)	Dec.[b] (deg)	g_0[c] (mag)	r_0[c] (mag)	$\mu_\alpha \cos\delta$ (mas/yr)	μ_δ (mas/yr)	D_{ϕ_1}[d] (kpc)	p_i[e]
10919800324884	5642070216297474048	132.05840	-30.05427	18.17	18.37	-0.44 ± 0.10	-1.14 ± 0.14	33.93	1.00 ± 0.00
10932700187714	5641117356333830144	131.11522	-31.50268	17.74	17.87	-0.24 ± 0.10	-1.14 ± 0.14	28.63	1.00 ± 0.00
10932700243590	5641143602871524352	131.14655	-31.15677	18.06	18.21	-0.36 ± 0.09	-1.09 ± 0.13	32.97	1.00 ± 0.00
10932700005729	5641173706306020352	131.49331	-30.92151	18.04	18.17	-0.42 ± 0.09	-1.27 ± 0.13	32.74	1.00 ± 0.00
10945400217453	5639433140738629632	130.01729	-32.82041	18.13	18.23	-0.11 ± 0.12	-1.33 ± 0.16	34.49	0.98 ± 0.01
10945400252679	5639607653847863296	130.90331	-31.82911	17.93	17.94	-0.39 ± 0.10	-1.22 ± 0.14	32.04	1.00 ± 0.00
10945400026245	5639609474914353152	131.08236	-31.71127	18.11	18.22	-0.13 ± 0.11	-0.72 ± 0.17	33.90	0.90 ± 0.07
10958200151163	5638618544360909824	129.29248	-34.73100	18.08	18.23	-0.25 ± 0.16	-1.06 ± 0.22	33.07	0.99 ± 0.00
10958200396025	5638741754084684800	129.44514	-34.19862	18.08	18.33	0.16 ± 0.15	-1.03 ± 0.21	30.84	0.98 ± 0.01